To the Graduate Council:

I am submitting herewith a dissertation written by Guillermo Daniel Del Cul entitled "Luminescence, Raman and Absorption Spectrophotometric Studies of Selected Lanthanide and Actinide Compounds in the Solid State." I have examined the final copy of this dissertation for form and content and recommend that it be accepted in partial fulfillment of the requirements for the degree of Doctor of Philosophy, with a major in Chemistry.

Joseph R. Peterson, Major Professor

We have read this dissertation and recommend its acceptance:

James L. Adcock

Jeffrey D. Kovac

Stanley E. Nave

Accepted for the Council:

Vice Provost
and Dean of The Graduate School

DOE/ER/13865-029

LUMINESCENCE, RAMAN AND ABSORPTION SPECTROPHOTOMETRIC STUDIES OF SELECTED LANTHANIDE AND ACTINIDE COMPOUNDS IN THE SOLID STATE

A Dissertation

Presented for the

Doctor of Philosophy

Degree

The University of Tennessee, Knoxville

Guillermo Daniel Del Cul

December 1990

DEDICATION

The author desires to dedicate this work to his wife, Amalia, his daughters Lia, Silvina and Nora, his mother Ines, and in memory of his father Emilio.

ACKNOWLEDGMENTS

There are many people from whom the author received invaluable help that made this work possible.

The author wishes to thank Professor Joseph R. Peterson for his advice and financial, scientific, and technical support during the course of this work.

Special thanks go to Dr. S. E. Nave, Dr. G. M. Begun, Dr. R. G. Haire, Dr. C. E. Bamberger and Dr. G. M. Murray for sharing their vast expertise.

Thanks also go to the entire staff of the Transuranium Research Laboratory (TRL) and the author's dissertation committee Dr. J. L. Adcock, Dr. J. D. Kovac and Dr. S. E. Nave for their helpful cooperation.

This research was performed in the TRL at the Oak Ridge National Laboratory and was sponsored by the U.S. Department of Energy under grant DE-FG05-88ER13865 to the University of Tennessee, Knoxville and contract DE-AC05-84OR21400 with Martin Marietta Energy Systems, Inc. The author gratefully acknowledges these organizations for their financial and operational support.

ABSTRACT

Raman, absorption and luminescence spectroscopy has been used extensively in our laboratory to recognize crystal structures or to identify changes in the structural pattern of solid compounds at different temperatures and pressures. These techniques have also been employed to determine the chemical environment of f element ions in different compounds and solutions.

Polarized Raman spectroscopy was used to assign the Raman-active bands of selected lanthanide oxyhalide single crystals. Cerium oxychloride was synthesized for the first time in the present research.

The polarized luminescence, absorbance and electronic Raman spectra from single crystal europium oxychloride, recorded at 300 and 77 K, were measured, interpreted, and used to calculate crystal field parameters. Although a suitable UV excitation source was unavailable, luminescence from the upper levels was obtained by resonance enhanced two-photon excitation.

The same techniques were applied to both a collection of coaxial single crystals and polycrystalline europium oxychloride under pressure using a diamond anvil cell. The spectra at high pressure suggest the presence of Eu^{II} ion.

The two-photon sequential excitation technique was also employed, for the first time, to study the electronic levels

of Cm^{III} and Cf^{III} in trihalides. Such luminescence is often weak due to an efficient nonradiative de-excitation process due to closely spaced energy levels. Nevertheless, because of the low background encountered in two-photon processes, the energy of many levels can be obtained. These energy values were used to determine ion site symmetries and in some cases to calculate crystal field parameters.

The effect of pressure on the Raman, absorption and luminescence spectra of $CmCl_3$ was investigated. The curium trichloride behavior was compared to previous studies on lanthanide trihalides and along with new studies on $NdBr_3$ to confirm the possibility of a new high pressure phase.

TABLE OF CONTENTS

LIST OF TABLES

LIST OF FIGURES

CHAPTER I

INTRODUCTION

A. Background

The fourteen elements from cerium to lutetium constitute the lanthanide series resulting from the filling of the 4f orbitals. Similarly, as realized by G. T. Seaborg in 1944 [1], the actinides from thorium to lawrencium involve the filling of the 5f orbitals. Because of this fact, lanthanides and actinides show numerous similarities.

All the lanthanides with the exception of the unstable ^{147}Pm and the actinides thorium and uranium are as abundant in nature as many of the common elements. As an example [2], thorium constitutes 8.1 ppm of the earth's crust and is almost as abundant as boron (9 ppm) whereas uranium at 2.3 ppm is almost as abundant as bromine (2.5ppm) and more abundant than tin (2.1 ppm).

All the elements beyond uranium have been produced artificially and in fact man-made transuranium elements now comprise about fifteen percent of all the presently known chemical elements. The transuranium elements are primarily produced by a sequence of neutron captures and beta decays under prolonged neutron irradiation inside nuclear reactors. For example

$$^{238}U + {}^{1}n \rightarrow {}^{239}U \xrightarrow{\beta^-} {}^{239}Np \xrightarrow{\beta^-} {}^{239}Pu$$

Because of competition between beta decay and nuclear fission, and the general trend of shorter half-lives with increasing atomic number, the availability of transuranium element isotopes greatly decreases across the series.

The systematic study of the actinide elements presents nontrivial experimental problems. All of them are highly radiotoxic. Consequently, the safe handling of these materials requires the use of radiochemical hoods and gloved box facilities. Pyrophoric or moisture sensitive compounds impose the use of inert-gas atmospheres. Due to availability and safe handling, sample sizes are typically in the microgram range. The manipulation of such small samples requires the utilization of microchemical techniques along with absolute containment of the specimens. The primary sample enclosure is usually a quartz capillary, while secondary containment is determined by each particular experimental technique.

Methodical planning and safety precautions must be exercised at all times to ensure permanent radiological containment of the samples.

B. Oxidation States

For the lanthanides the trivalent state, Ln^{III}, is prevalent. The 4f electrons are deeply buried in the inner core of electrons and are seldom accessible for bonding. The enhanced stability of the f^0, f^7 and f^{14} configurations is

demonstrated by the existence of Ce^{IV} , Eu^{II} and Tb^{IV}, and Yb^{II}, respectively.

In the early actinides the 5f electrons have a greater spatial extent and therefore are more effectively shielded from the nuclear charge than are the 4f electrons of the corresponding lanthanides. Consequently these elements behave more like d-transition elements and exhibit a very wide range of oxidation states. The increased effective nuclear charge going across the series finally makes the 5f electrons behave like the lanthanides' 4f electrons. This behavior is evident in the second half of the series where the trivalent oxidation state predominates. At the same time there is an increasing tendency toward divalency that extends from Am to No, where the divalent oxidation state is actually the most stable in aqueous solution.

C. Spectroscopic Properties

One of the main characteristics of lanthanide and transplutonium actinide elements is that even though the f orbitals contain the optically active electrons, they can be regarded at the same time as belonging to the inner core of filled shells. As a result, the optical spectra of these elements are moderately insensitive to external influences. Thus, the electronic levels of free ions are only slightly different from the corresponding energy levels in compounds

[3-7].

The calculated energy levels of the f^n electronic configurations of trivalent lanthanide and actinide "free" ions are shown in Figures 1 and 2, respectively [5]. Because of the scarcity of gaseous free ion data, the "free" ion energy-level structure is usually obtained from the study of condensed phases and subsequent correction of the experimental energy levels by removal of the calculated crystal field interactions. The "free" ion states shown in Figures 1 and 2 were deduced from the observed electronic energy levels of Ln^{III} and An^{III} ions doped in $LaCl_3$, and the width of the bands represent the extent of the experimentally observed crystal field splitting [5].

As a first approximation the electronic configurations of the lanthanides can be described using the Russell-Saunders coupling scheme. As already mentioned, the 4f electrons in lanthanide ions are deeply buried in the inner electron core and therefore shielded from their chemical environment. Crystal field effects are consequently much smaller than those resulting from the spin-orbit coupling. The predominant interaction between the orbital and spin motions generates a resultant total angular momentum designated by the quantum number J.

In the lanthanides the most common electronic transitions involve only a redistribution of electrons within the 4f orbitals. Such transitions are orbitally forbidden by the

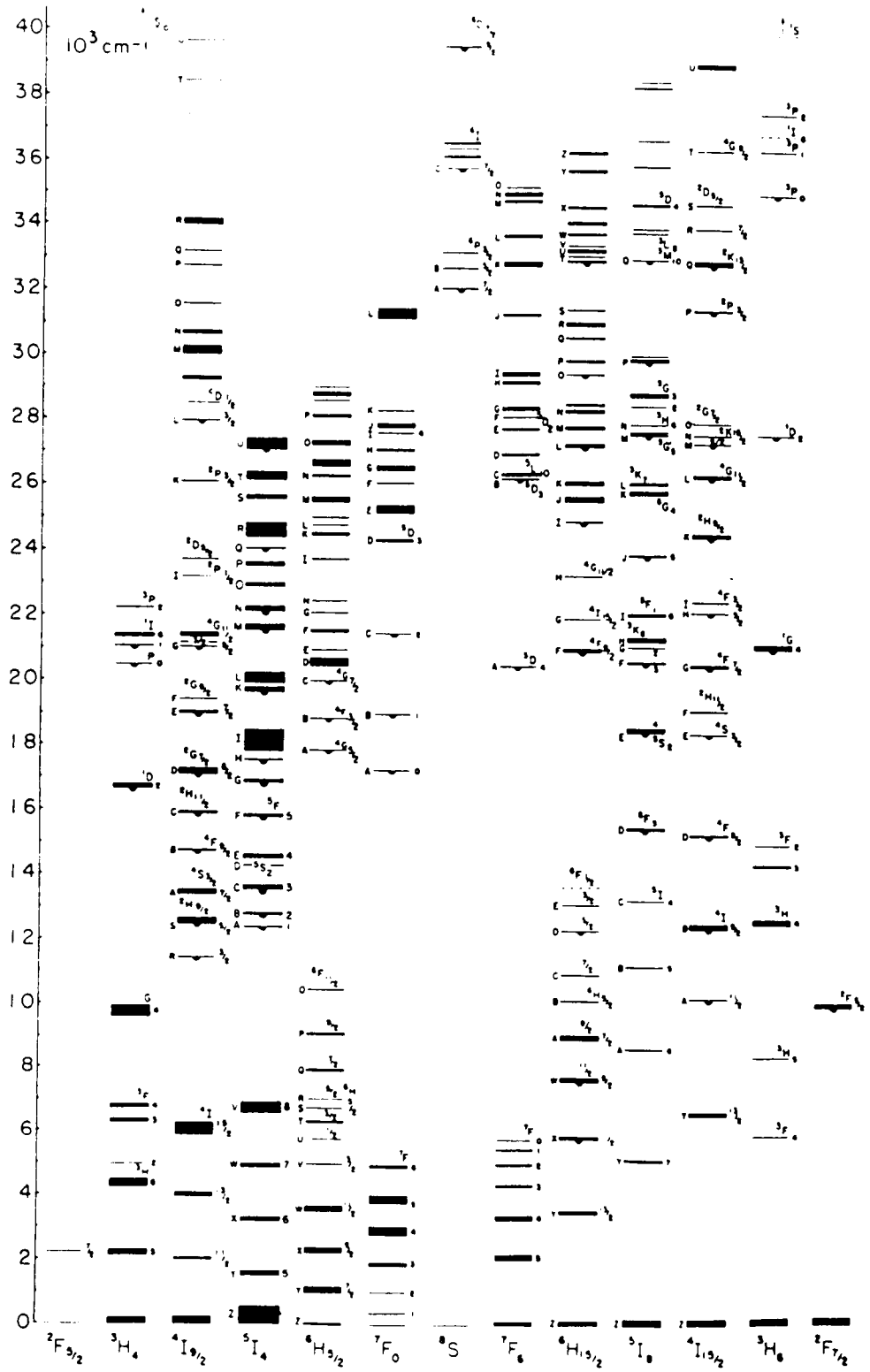

Figure 1. "Free" ion Energy Levels of the Trivalent Lanthanides.

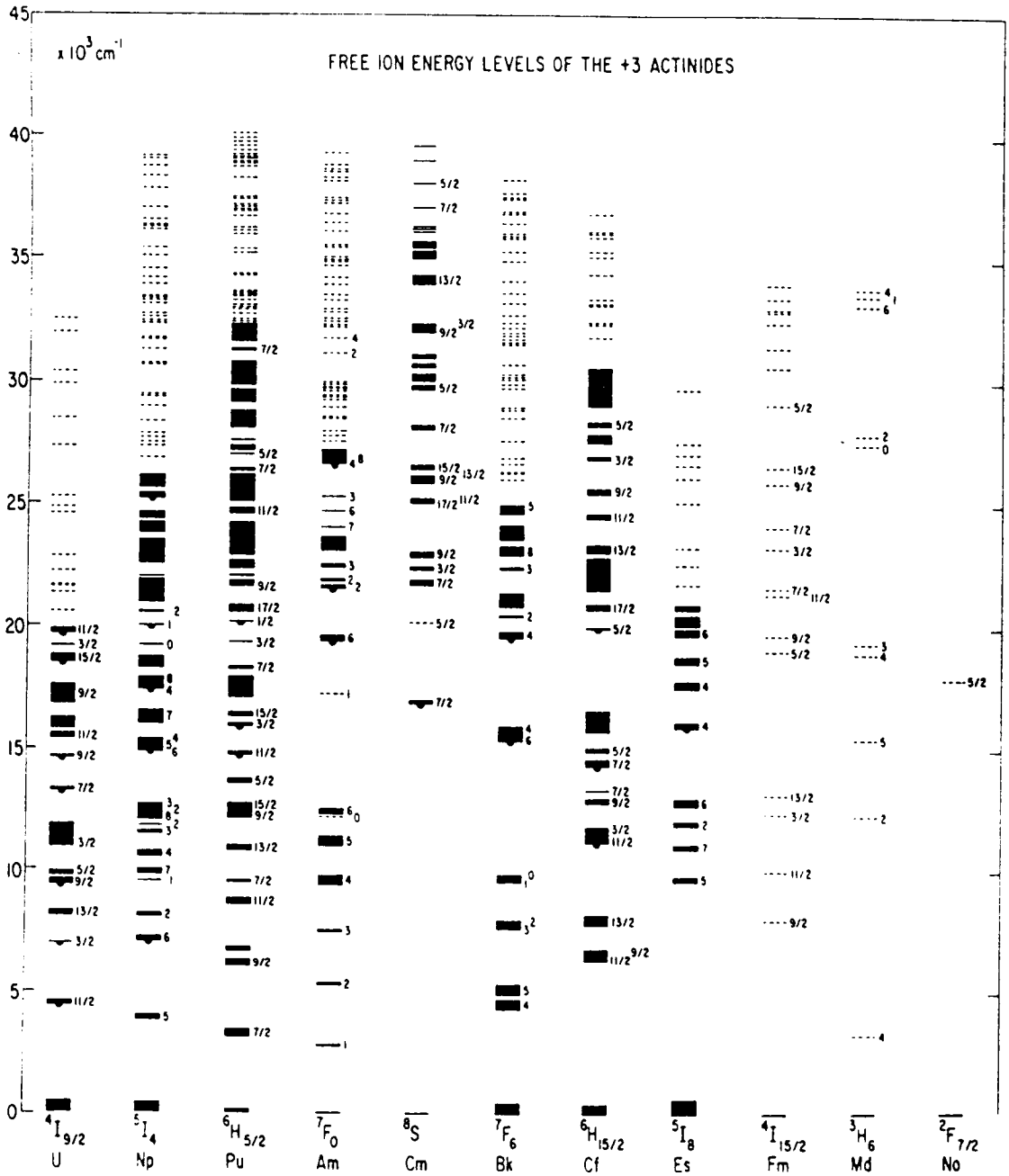

Figure 2. "Free" ion Energy Levels of the Trivalent Actinides.

selection rule $\Delta L = \pm 1$, so they are of low intensity. Derived from the small effect of the electronic environment is the fact that the electronic transitions have a narrow energy width and exhibit a fine structure due to the crystal field splitting of the components of the J-state. However, in the case of the Ln^{II} ions with a lower effective nuclear charge, the 4f and 5d orbitals are much closer in energy. For this reason the spectra of Ln^{II} species consist of fairly broad, intense, orbitally allowed 4f→5d bands superimposed on the weaker and much sharper f→f bands.

In the actinides spin-orbit coupling is also strong; however, due to the greater exposure of the 5f electrons, crystal-field splittings are of similar magnitude, and J may no longer be such a good quantum number. In addition, and particularly for the early actinides, the energy levels of the 5f and 6d orbitals are much closer together than the corresponding 4f and 5d orbitals in the lanthanides. As a result, in order to understand the optical properties of the actinides, it is necessary to consider mixing of "J levels," which leads to slightly broader f→f transitions in the visible region. A characteristic absorption spectrum of actinide compounds also includes the quite intense and broad 5f→6d and ligand→metal bands (parity allowed) in the ultraviolet wavelength region.

D. Lanthanide and Actinide Trihalides

1. Trifluorides

The anhydrous lanthanide and actinide trifluorides form a group of ionic, high melting compounds. All the lanthanide and actinide trifluorides [8,9] are reported to crystallize in the LaF_3-type trigonal crystal structure, space group D^4_{3d}-$P\bar{3}c1$, where the cation is nine-coordinated according to a tricapped trigonal prismatic geometry.

There is also a low-temperature, orthorhombic yttrium trifluoride-type form [8,9] for the lanthanide trifluorides of samarium to lutetium, yttrium, and the actinide trifluorides of berkelium and californium. This low-temperature form belongs to the space group D^{16}_{2h}-Pnma where the cation has eight near neighbors and a ninth neighbor at a slightly larger distance away.

2. Trichlorides, Tribromides, and Triiodides

The known crystallographic forms of the lanthanide and actinide trihalides (except the trifluorides) number four [8,9]. These are: (1) the monoclinic aluminum chloride type, space group C^3_{2h}-C2/m, which is a distorted octahedral sodium chloride structure in which two thirds of the metal ions are omitted; (2) the rhombohedral bismuth triiodide or iron trichloride type, space group C^2_{3i}-$R\bar{3}$, in which each metal ion

is at the center of an almost perfect octahedron of halogen atoms; (3) the orthorhombic plutonium tribromide type, space group D^{17}_{2h}-Cmcm, in which each cation is octacoordinated with a bicapped trigonal prismatic geometry; and (4) the hexagonal uranium trichloride type, space group C^{2}_{6h}-$P6_3/m$, in which each metal ion is bonded to nine halogens according to a tricapped trigonal prismatic geometry.

In some cases, the different crystallographic forms interconvert readily with temperature or pressure [10-13].

E. Oxychlorides

The oxychlorides of the actinides and lanthanides with the exception of TmOCl, YbOCl and LuOCl crystallize with the tetragonal lead chlorofluoride-type structure [8,9], space group D^{7}_{4h}-P4/nmm, in which the metal ion is surrounded by four oxygen ions and five chloride ions in a monocapped antiprism.

Thulium, ytterbium, lutetium and a second phase of erbium oxychloride possess the SmSI-type rhombohedral crystal structure [9,14,15], space group D^{5}_{3d}-$R\bar{3}m$, in which the cation is decacoordinated.

F. Proposed Research

The objective of this work was to investigate the crystal structure, electronic energy levels, chemical environment and crystal field parameters of actinide and lanthanide compounds.

To do so, a combination of Raman, absorption and luminescence spectroscopy along with X-ray diffraction was used.

Polarized Raman spectroscopy was used to assign the Raman-active bands of selected lanthanide oxyhalide single crystals. Phonon Raman spectroscopy was utilized on europium oxychloride, neodymium tribromide and curium trichloride to identify phase transitions under different applied pressures using a diamond anvil cell.

Single and two-photon luminescence along with absorption and electronic Raman spectroscopy were employed to measure and interpret the electronic energy levels of europium oxychloride and to calculate crystal field parameters.

Single and, for the first time, two-photon excitation were also used to study the electronic structure and site symmetries of Cm^{III} and Cf^{III} ions in selected trihalides.

CHAPTER II

EXPERIMENTAL TECHNIQUES

A. Sample Preparation

1. Transuranium Isotopes

The transuranium isotope ^{248}Cm ($t_{½}$ = 3.4x10^5 y) employed in this work was synthesized via long-term neutron irradiation in the High Flux Isotope Reactor (HFIR) at the Oak Ridge National Laboratory as part of the U.S. Department of Energy's program for transuranium elements production and research.

The ^{249}Cf ($t_{½}$ = 351 y) isotope was generated by beta decay of ^{249}Bk ($t_{½}$ = 320 d) which had been directly synthesized in HFIR.

2. Lanthanide and Actinide Oxides

Lanthanide and actinide oxides were utilized as intermediary materials in the synthesis of trihalides and some oxychlorides. While the lanthanide sesquioxides were commercially available, the curium oxide and the californium-doped lutetium oxide were synthesized according to published methods [16]. Due to the radiotoxicity the preparations were done inside an air-flow gloved box. An aqueous chloride or nitrate solution of curium(III) and of lutetium(III) spiked with californium (approx. 1%) were

precipitated with oxalic acid in a teflon (PTFE) microcone. The oxalate precipitate was dried under an infrared lamp and finally calcined for 6-12 hours at 1000 °C in air in a platinum boat. The californium-doped lutetium oxide possessed the sesquioxide stoichiometry, i.e., Lu_2O_3. The curium oxide was of intermediate composition, possessing a stoichiometry best represented by CmO_{2-x} ($x \leq 0.3$). Curium sesquioxide was synthesized by reduction of this mixed-valence oxide with anhydrous H_2 gas at 500 °C.

3. Lanthanide and Actinide Trihalides

The trichlorides of praseodymium, neodymium, and europium (prepared as intermediaries to the growth of the corresponding oxychloride single crystals) along with neodymium tribromide, californium-doped lutetium trichloride and the three heavier curium trihalides were prepared using the system schematically diagrammed in Figure 3 and according to microchemical methods previously reported [17]. Basically the equipment includes a glass manifold that can be connected, by opening the appropriate valve, to a high vacuum system or alternatively to delivery lines of anhydrous purified gases including HCl, HBr, HI, H_2 and Ar.

The usual preparatory steps start with the loading of the respective sesquioxide into the tip of a quartz capillary which has been drawn from a 14/35 standard-taper, quartz

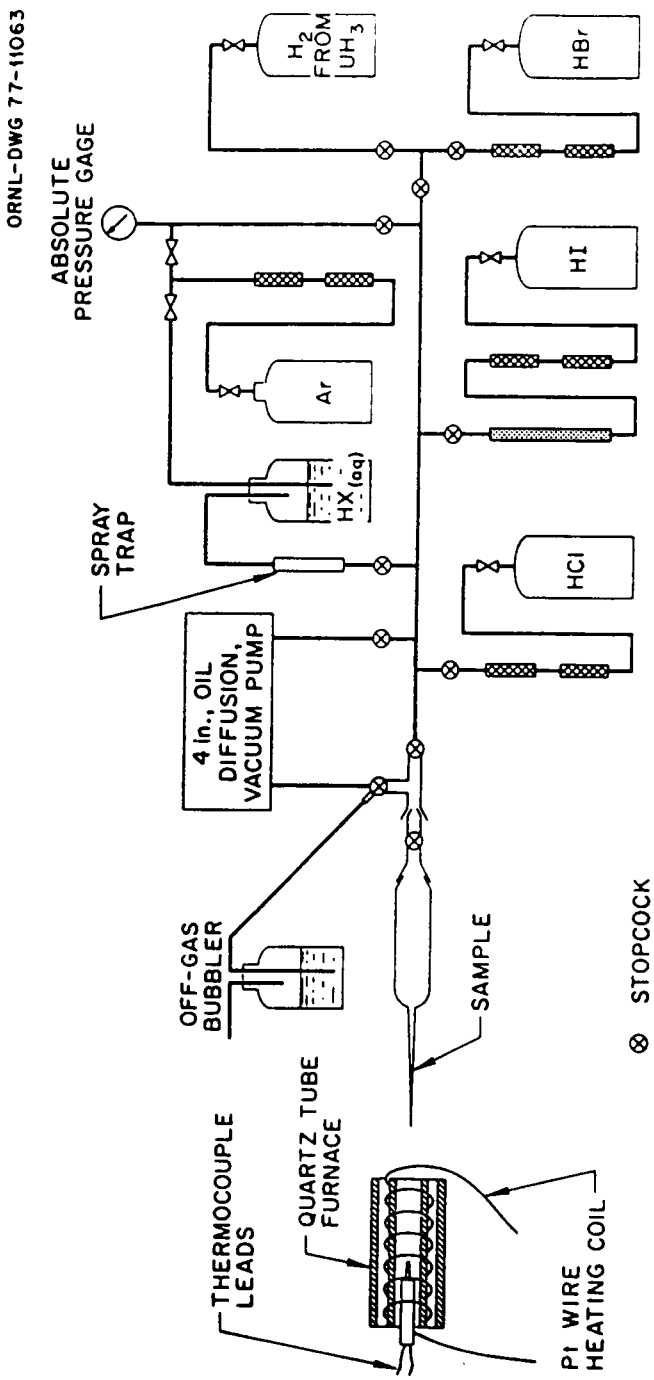

Figure 3. Schematic Diagram of the Compound-Preparation System.

joint which has been preleached in an HCl (6 M) solution for 24 hours. The loading of curium and californium-doped samples was done inside a gloved box. The sample-loaded capillary is then connected using Apiezon H grease to an Ace Glass Inc. S-shaped stop-cock which is attached to the preparation/vacuum system. The capillary is carefully evacuated to avoid projection of tiny particles into the vacuum system. The sample is observed through an adjustable, long-focal-length binocular microscope. The same microscope is used for the scrutiny of sample movement, color changes, melting or other changes during the course of the chemical treatment. A Pt-wire-wrapped quartz tube furnace is positioned, with the aid of a micromanipulator, around the capillary. A type-K (chromel-alumel) thermocouple is placed adjacent to the sample for monitoring the temperature. The oxide sample and capillary container are outgassed under vacuum at a temperature of about 700 °C. After the degassing the temperature is adjusted to the range 450-500 °C and the oxide is put in contact with the appropriate HX gas for a few minutes, after which the sample is allowed to cool to about 200°C. The sample capillary is evacuated first using the roughing pump and finally under high vacuum to remove excess reactant gas and any volatile reaction by-products, mainly water. This process is repeated several times with increased residence time of the HX gas. The reaction is determined to be complete when the sample is observed to melt congruently and completely, and the Raman

phonon spectrum of the product matches that expected. The preparation of triiodides is not done by direct treatment of the oxide with HI, because this route invariably leads to products containing oxyiodide. Instead, the synthesis is carried out through the initial preparation of the corresponding anhydrous trichloride or tribromide and subsequent reaction of it with excess anhydrous HI. In fact, all of the trihalides can be readily interconverted in this way using an excess of a specific anhydrous HX on a solid sample of a different halide.

4. Polycrystalline Oxychlorides

All lanthanide oxychlorides with the exception of CeOCl and EuOCl can be easily prepared by thermal decomposition of the trichloride hydrates in air. The $LnCl_3.xH_2O$ were obtained by dissolution of the sesquioxides in concentrated HCl and further evaporation of the resulting solution. The optimum temperature to obtain pure oxychlorides depends on the lanthanide element, but in general it is in the range 400-650 °C. The thermal decomposition of the trichloride hydrates of cerium produces cerium dioxide. In the case of europium the product is a dark solid containing mixed-valence (II and III) phases.

A very simple method, that also works with cerium and europium, was used to obtained lanthanide oxychlorides. This

procedure consisted of heating the trichloride hydrate in the presence of excess water and gaseous HCl with total exclusion of air, at temperatures in the range 650-700 °C for about fifteen minutes. The present work appears to be the first report of the synthesis of CeOCl with the exception of the reported production of CeOCl as an intermediary in a cerium-chlorine system for thermochemical production of hydrogen [18].

5. Single-Crystal Oxychlorides

Single crystals of praseodymium, neodymium and europium oxychloride were prepared by flux growth from a melt of the respective anhydrous $LnCl_3$ as described in the literature [19-21]. The starting material for all preparations was the commercially available 99.9% pure sesquioxide. The oxide was dried under vacuum and handled afterwards in a dry argon filled gloved box. Each particular trichloride was obtained by treating the corresponding oxide with anhydrous HCl at 400 °C in a platinum crucible. The system is similar to the one depicted previously in Figure 3. The main difference is that the sample-containing quartz tube is no longer a capillary but is 1" in diameter and is heated by a clam-shell furnace. A mixture of one part of the dried oxide and ten parts of the anhydrous trichloride was introduced into platinum tubing (6 mm ID), and both ends were sealed by crimping and spot-

welding. The sealed platinum tube was then contained in a quartz tube back-filled with dry argon (500 mmHg). A programmable furnace (Harrop Industries) was used for the following thermal cycle: heating to 950 °C at the maximum rate, holding at that temperature for fifteen hours, then cooling at 5 °C per hour to 500 °C and finally fast cooling to room temperature. The excess $LnCl_3$ was removed by washing the product in distilled water. The remnants consisted of single-crystal platelets (up to 4 x 4 x 0.1 mm) of the respective oxychloride.

B. X-Ray Diffraction Analysis

1. Equipment

A General Electric Model XRD-6 X-ray generator was utilized to obtain powder diffraction photographs to confirm crystal structures and to align the oxychloride single crystals. For diffraction the K_α radiation (wavelength = 1.54178 Å) from a copper target with a 0.1 x 1.4 mm filament along with a 0.7 mil nickel foil to stop the CuK_β radiation was used. For alignment of the single crystals, a molybdenum target (MoK_α, wavelength = 0.7107 Å) with a 0.8 x 12.5 mm filament was utilized. The film camera was a Phillips-Norelco (57.3 mm diameter) Debye-Scherrer type with Straumanis-type film mounting. To surround and protect the fragile capillary, a beryllium cup was employed [22]. All exposures were taken at

room temperature on Ilford Industrial G film. Exposure times were on the order of 4 hours but varied for radioactive samples. Exposures in these latter cases were often less than 4 hours due to darkening of the film by the emitted radiation. The developed films were read on a Phillips-Norelco film reader. A traveling cross hair and steel vernier scale permitted the determination of line positions to the nearest 0.05 mm.

2. Analysis of Powder Patterns

No film shrinkage factor was used in the analysis of the data. The observed lines were compared with data obtained from the JCPDS Powder Diffraction File [23] to confirm the crystal structure.

3. Single Crystal Alignment

Each batch of lanthanide oxychloride single crystals was examined under the microscope. The best looking platelets by size and appearance were sorted out. A selected crystal was attached to a quartz rod with a minimal amount of Q-dope glue. The rod was then mounted on a goniometer head which can be adjusted in all three directions. The alignment of the crystal was done by the precession method [24]. The light lanthanide oxychlorides are known to be tetragonal [8,9]. The plane of the platelet was assumed to contain two of the axes with the

third axis perpendicular to the surface. In order to confirm this assumption and to determine the orientation of the crystal with respect to the goniometer head, precession photographs were taken. These pictures show the crystal lattice in reciprocal space, where each family of crystal planes appears as a point. The orthogonal axes were easily recognized, and adjustments were made to properly align the crystal. A Laue photograph taken parallel to the large flat face of the platelet showed clearly a four-fold symmetry axis characteristic of the 00ℓ planes in a tetragonal structure, such as the PbFCl type, confirming that the c-axis was perpendicular to the plane of the platelet.

C. Solid-State Absorption Spectrophotometry

1. Equipment

Two different types of equipment were used to obtain solid-state absorption spectra, and both are single-beam spectrophotometers. One apparatus is the same as that utilized for Raman and luminescence spectrometry and will be described in Section D . The second one is of local design [17] and is shown schematically in Figure 4. The light from a tungsten halogen lamp is focused onto the sample by a reflecting microscope objective. The illuminated area is adjustable by opening or closing an iris. A sample area of about 5 μ^2 completely covers the smallest possible illuminated spot.

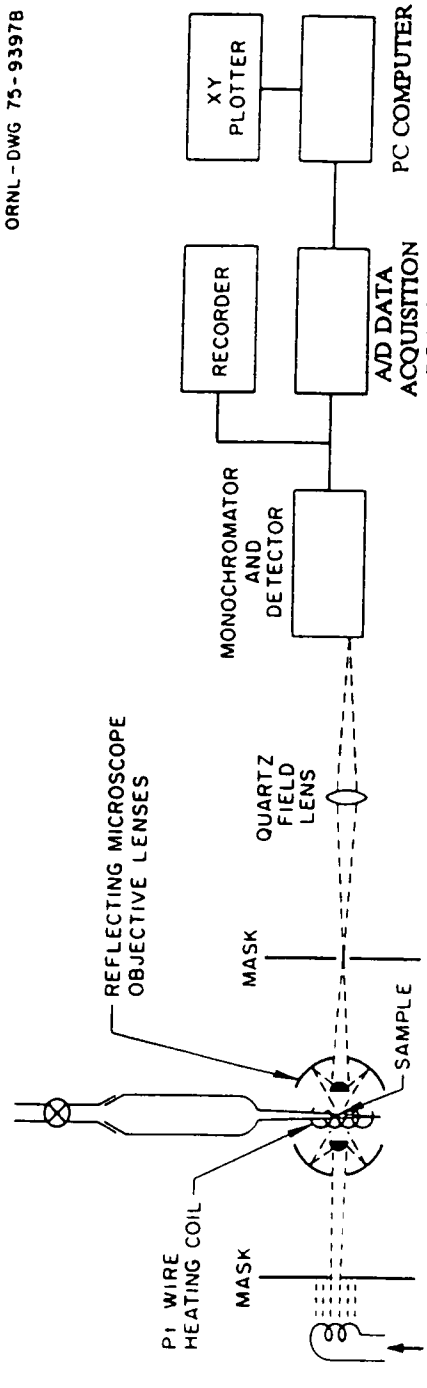

Figure 4. Schematic Diagram of the Microscope Spectrophotometer and Data Acquisition system.

The light passing through the sample is collected by another reflecting microscope objective and focused through the use of quartz field lens onto the entrance slit of a Jarrell Ash 1/2 meter scanning monochromator. This monochromator is equipped with a 1180 lines/mm grating blazed at 4000 Å. At the output of the monochromator there is a S-1 type RCA 7102 photomultiplier tube that is cooled when in use with a dry ice-acetone bath. The useful wavelength range of this instrument is 300-1100 nm.

2. Data Treatment

The output from the photomultiplier is amplified and measured through a resistor as a voltage. The voltage output is fed to an A/D data acquisition board Metrabyte DAS 16G connected to a PC-AT compatible computer and digitized at a programmable rate, stored as an ASCII file on disk and displayed as a graphic on the computer monitor. The data are further analyzed using the Spectra Calc software [25]. Because this is a single-beam instrument, the program transforms logarithmically the light attenuation data into an absorbance-like spectrum. Another feature of the same software package is used to reduce the noise using a Fourier-transform filter. The spectrum baseline is flattened-out using a multipoint fitting routine. The spectrum can be zoomed, deconvoluted, plotted and stored for further analysis.

D. Raman Spectroscopy

1. Equipment

Raman, absorption and luminescence spectra and lifetime measurements of both lanthanide and actinide compounds were obtained with the system depicted in Figure 5. The heart of the apparatus is a Ramanor HG.2S spectrophotometer (Jobin Yvon-Instruments SA). This spectrophotometer uses a double monochromator equipped with curved holographic gratings, a cooled photomultiplier detector, an amplifier, pulse discriminator and pulse counting electronics. A Nicolet 1170 multichannel analyzer and signal averager was used to collect the data. From the fast NIM output of the pulse discriminator a second pulse counter was used for lifetime measurements (see Section E). The curved holographic gratings of the double monochromator are characterized by 2000 lines/mm. The photomultiplier detector was a red sensitive Hammammatsu model R636 which was operated at -30 °C using a thermoelectric cooler. An argon-ion laser model Innova 90-5 from Coherent Radiation was the main excitation source either in the single line mode or as a multiline source pumping a tunable dye-laser model 590 also from Coherent Radiation. In addition, a krypton and a nitrogen laser were utilized. The system is also equipped with a Nachet microscope attachment. This accessory was utilized to obtain absorption spectra of solid samples.

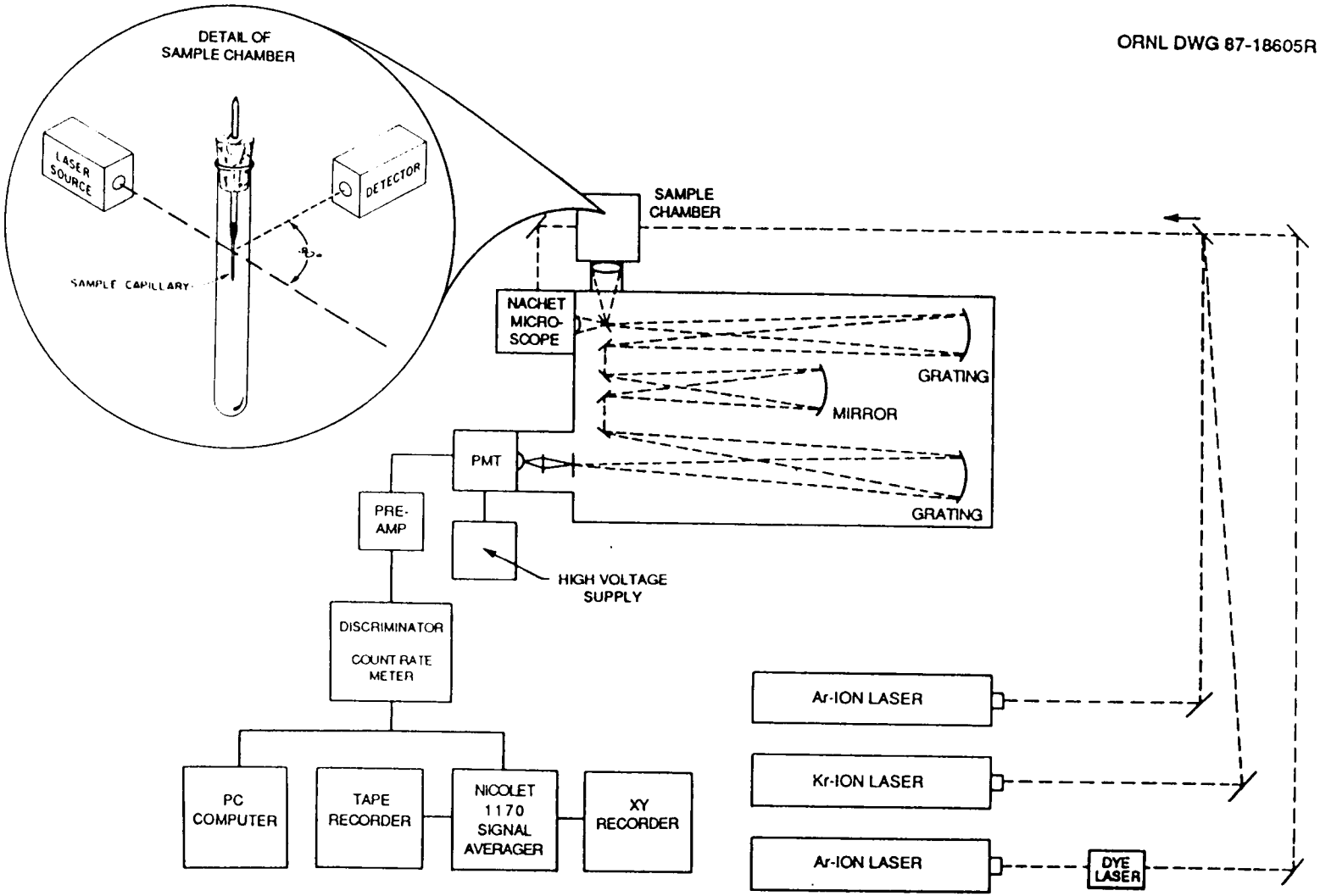

Figure 5. Schematic Diagram of the Raman Spectrophotometric System.

The light can enter the monochromator through a sample chamber illustrated in Figure 5 or via the microscope attachment. In the case of the sample chamber, the Raman scattered light is collected at 90° from the incident laser beam, as shown in Figure 6. On the other hand the light is collected at 180° by the microscope attachment.

The sample chamber was used for powdered samples and for the goniometer mounted single crystals. For low-temperature experiments, a small Dewar filled with liquid nitrogen or a refrigerated head from a CSW-204 Displex closed-cycle refrigeration system from Air Products and Chemicals Inc. was also located in the sample chamber.

The microscope accessory was principally used for obtaining spectra from samples under pressure in a diamond anvil cell.

2. Data Treatment

The data accumulated in the 4096-channel multichannel analyzer for signal averaging by the Nicolet 1170 were recorded on magnetic tape recorder for archival purposes. The data were also transferred through a serial 232C port to a personal computer where they could be evaluated and processed using the Spectra Calc software [25] as indicated in Section C.2.

3. Single-Crystal Polarized Spectra

The goniometer with an oriented single crystal was mounted inside the sample chamber (see Figure 5) and positioned with respect to the laser beam by an X,Y,Z micromanipulator. There are two ways in which the goniometer can be positioned, either the Z-axis is parallel or perpendicular to the plane containing the exciting and scattered light beams.

The polarized Raman spectra were obtained by rotating the plane of polarization of the exciting laser light beam to be either perpendicular or parallel to the plane containing the exciting and scattered light beams. For this purpose a Spectra-Physics model 310-21 broad band polarization rotator was used. To analyze the polarization of the scattered light, an oriented Polaroid sheet was placed before the monochromator and a polarization descrambler was employed just prior to the entrance slit of the monochromator.

To indicate the possible combinations of crystal axis orientations, incident light polarization and orientation of the polaroid analyzer, the conventional nomenclature was used [26]. For example, imagine a tetragonal oxychloride single crystal mounted in such a way that the Z axis is perpendicular to the plane containing the exciting and scattered light beams. The laser beam coincides with the X axis and the detected scattered beam with the Y axis. The Cartesian X, Y, Z axes are designated a, b, c, respectively. The designation

for this configuration is a( )b . If, as illustrated in Figure 6, the electric vector of the laser is parallel to the c axis and the polaroid sheet is oriented in such a way to allow passage of scattered light with the electric vector parallel to the a axis, then the full designation is a(ca)b. All possible polarization combinations for crystal structures possessing orthogonal axes, like cubic, tetragonal, and orthorhombic, are depicted in Figure 7.

4. High Pressure Raman and Luminescence

A diamond anvil cell similar to the one described previously [27,28] and depicted in Figure 8 was used to subject EuOCl, $NdBr_3$ and $CmCl_3$ samples to pressures up to 40 GPa (400 kbar). An Inconel gasket is utilized for confining a pressure transmitting fluid [29] (silicone oil) between the diamond culets. The gasket is disk-shaped, made of a 200 μm thick Inconel X750 sheet, and is 10 mm in diameter. To accommodate to the diamonds, the gasket was pre-indented by pressing it in the diamond anvil cell to a thickness of approximately 75 μm. Finally a 200 μm diameter hole was drilled in the center of the indentation to contain the sample. The gasket is seated using a wax ring around its outer edge on one of the diamond flats in the same orientation it had when making the indentation. The hole is filled with the silicone oil and then the sample and a few ruby chips are

ORNL-DWG 88-6564

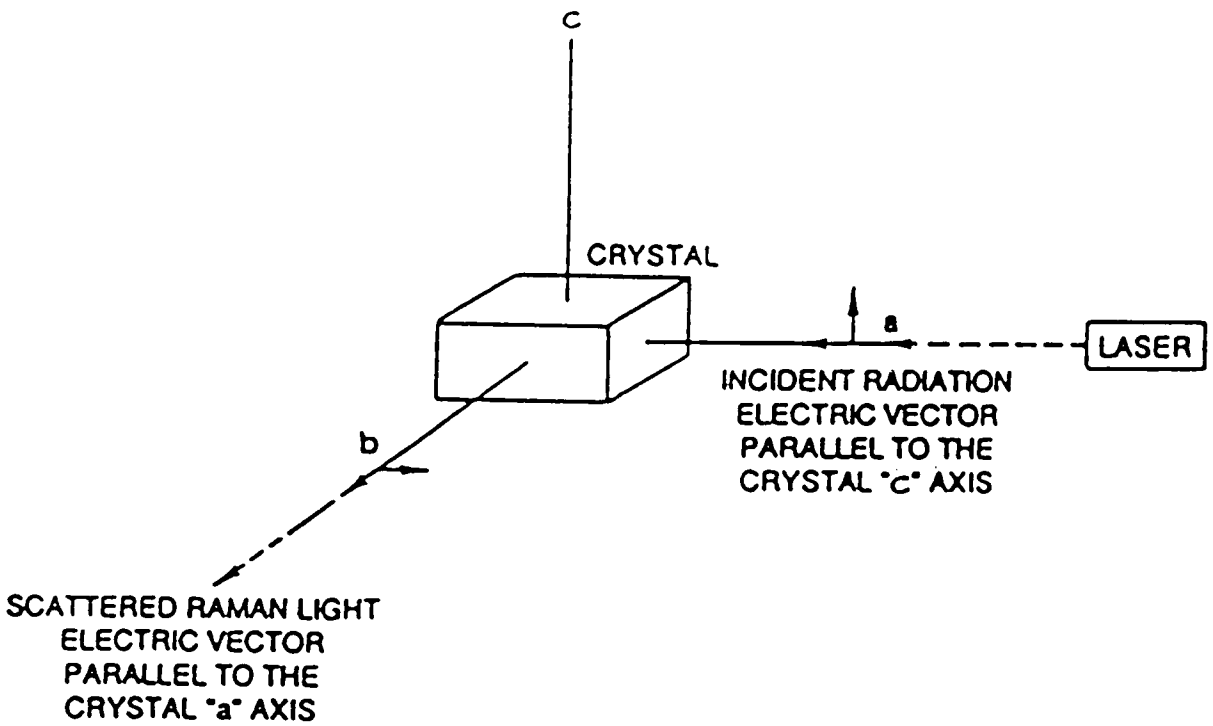

Figure 6. Polarization Diagram Corresponding to the Standard Notation a(ca)b.

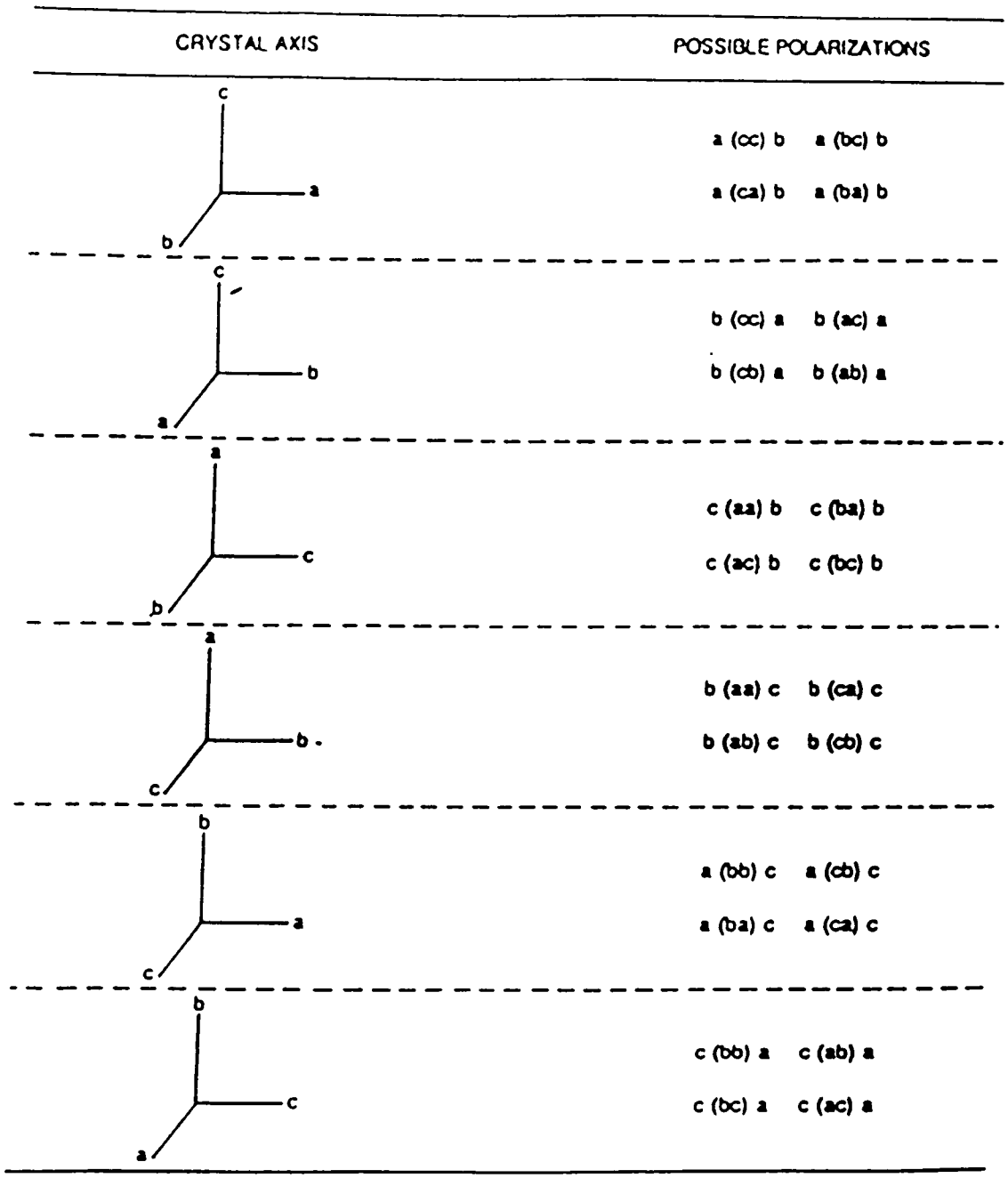

Figure 7. Possible Polarization Combinations for Crystal Structures Possessing Orthogonal Axes.

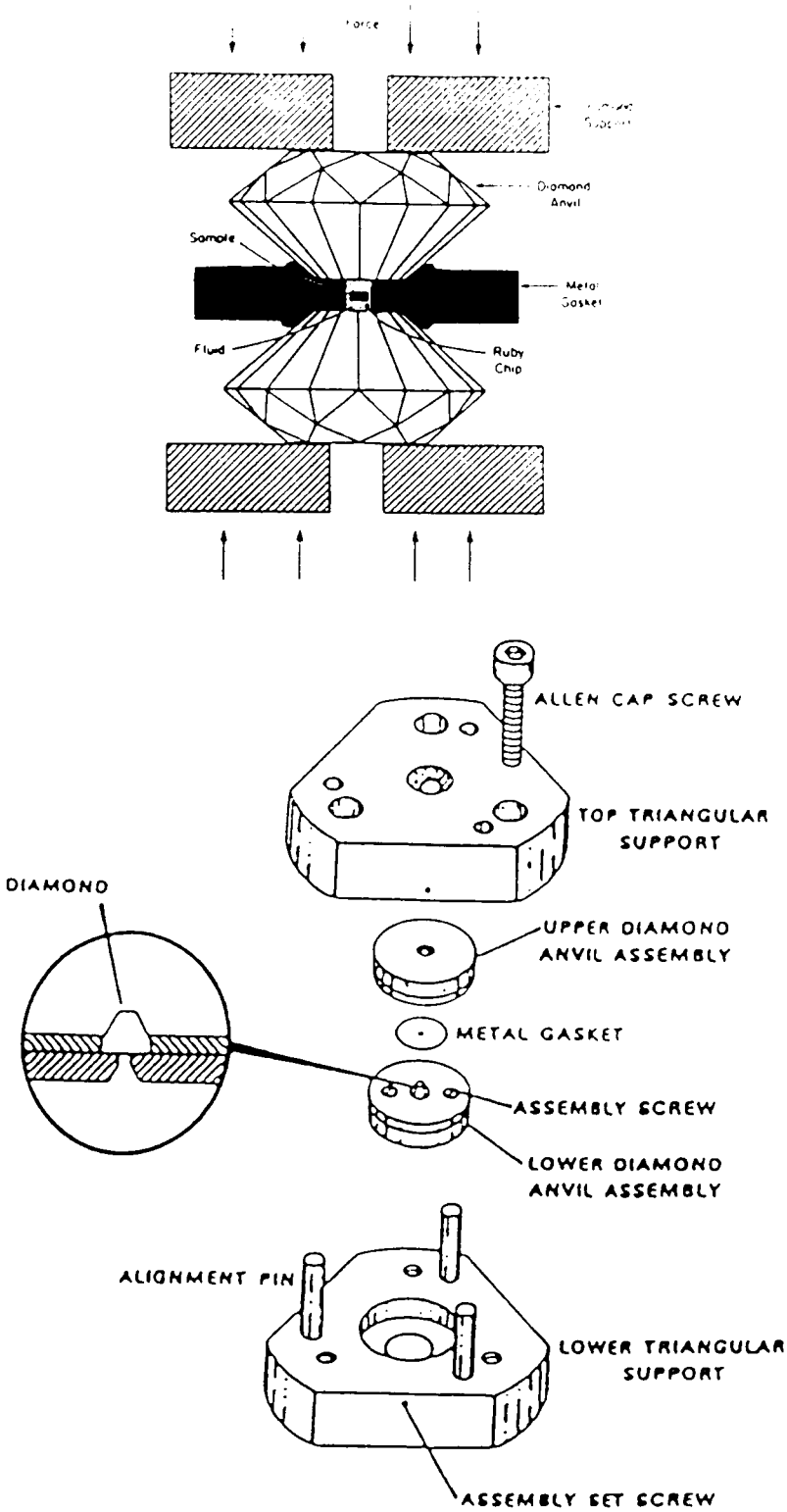

Figure 8. Exploded View of the Diamond Anvil Cell

immersed in the oil. The ruby chips serve as a pressure marker. The wavenumber-pressure relationship of the R1 fluorescence line emitted upon laser excitation of the ruby chips is well known [30,31,32]. Neodymium tribromide was loaded and tightened to seal in an argon filled gloved box because of its hygroscopicity. The same is true for $CmBr_3$ and in addition there is its radiotoxicity.

The Raman spectra were taken using a Nachet microscope attachment equipped with a 0.32 numerical aperture, 20X lens to focus the laser beam onto the sample through a beam splitter and to collect the 180° back-scattered Raman signal. The Raman data, as a function of pressure, were obtained in the same way as described in Section D.2.

E. Luminescence Spectroscopy and Lifetime Measurements

1. Equipment

Luminescence involves the emission of electromagnetic radiation, usually in competition with nonradiative decay processes, due to transitions between electronic energy levels. The transition originates from some excited level to a lower energy level. As already mentioned an argon-ion laser was the main excitation source, either in the single line mode (465.7 nm for Eu; 457.9 nm for Cm) or as a multiline source pumping a tunable dye-laser filled with rhodamine 6G.

In addition, a krypton (647 nm) and a pulsed nitrogen (334 nm) laser were also utilized.

2. Data Treatment

The data were collected and analyzed in essentially the same way as described in Section D.2. In the case of lifetime measurements, the excitation source was a pulsed nitrogen laser with a repetition rate of up to 60 Hz and pulse duration in the nanosecond region. A Stanford Research model SR450 photon counter coupled to a personal computer running the Stanford Research software was used to measure the after-peak radiation. The time resolved measurement was triggered by a pulse emitted by the nitrogen laser just after each pulse of light.

CHAPTER III

RESULTS AND DISCUSSION: POLARIZED RAMAN SPECTRA OF SINGLE-CRYSTAL TETRAGONAL LANTHANIDE OXYCHLORIDES

A. Introduction

1. Background

When light (photons) interacts with a crystal there are several processes that take place simultaneously. Light can be reflected, refracted, absorbed and finally light can be elastically and inelastically scattered. The Raman effect refers specifically to the inelastic scattering of photons. In the case of crystals, this inelastic dispersion is due to interaction between the photons and the vibrations of the crystal lattice with a change in the polarizability induced by the incident radiation. This interaction depends on the symmetry of these vibrations, or phonon modes. To determine the number and symmetry of these possible modes, the "correlation method" was used [33,34]. This method uses the symmetry restrictions of each occupied site in the crystal lattice. Site distributions in all of the space groups have been analytically determined [35] and tabulated for each case [36]. The combined motion of all the sites must be in accord

with the symmetry of the crystal as a whole; thus, a correlation between site and crystal symmetries is involved. The Raman-active phonon modes will be represented by those symmetry elements of the irreducible representation for the entire crystal which transform as a component of the polarization tensor α. The experimental assignment of these vibrational modes is done by correlating the changes in intensity of the different Raman-active bands with the expected behavior when the polarization of the laser beam and the orientation of the crystal are varied. As described in Chapter II-D.3 for the four letter notation (e.g., z(xy)x), the two symbols in parenthesis define the components of the scattering tensor being measured, whereas the other two symbols relate to the crystal orientation with respect to the exciting laser and the detected beam.

The polarization in a real crystal is not usually complete because of imperfections in the lattice structure. The number of expected vibrations for a given crystal can be calculated by taking into account the degrees of freedom present in the unit cell. If n is the number of ions in the unit cell, the degrees of freedom for n independent ions is 3n (each ion can move in any of the three directions). For a crystal, three of the 3n degrees of freedom are connected with the movement of the center of mass; thus, the remaining 3n-3 degrees of freedom will be associated with the lattice vibrations or optical modes. The three degrees of freedom

related to the movement of the crystal as a whole are called the acoustical modes of vibration. This motion is characterized by longer wavelengths with the crystal size determining their upper limit.

2. Tetragonal Oxyhalides

It was mentioned previously (Chapter I-E) that all the actinide and lanthanide oxybromides and oxyiodides, all the known actinide oxychlorides, and the light lanthanide oxychlorides from cerium to erbium (Er is dimorphic) possess the lead chlorofluoride-type structure [37,38], space group D^7_{4h}-P4/nmm [39]. The crystallographic unit cell contains two formula units. Since there are two formula units of LnOX per unit cell, there are fifteen lattice vibrations (3n-3) or optical modes and three acoustical modes.

X-ray crystallography data indicate that the metal and the halogen ions are located in atomic position 2c with site symmetry C_{4v} while the oxygens are situated in the 2a atomic positions with site symmetry D_{2d} (Figure 9). The C_{4v} site analysis is straightforward, the site symmetry species containing translation are A_1 and E. A_1 correlates with normal modes A_{1g} and A_{2u} while E correlates with normal modes E_g and E_u. The D_{2d} site analysis is more controversial because it can correlate with two different subgroups of point group D_{4h}. To choose the correct one, the relation between symmetry elements

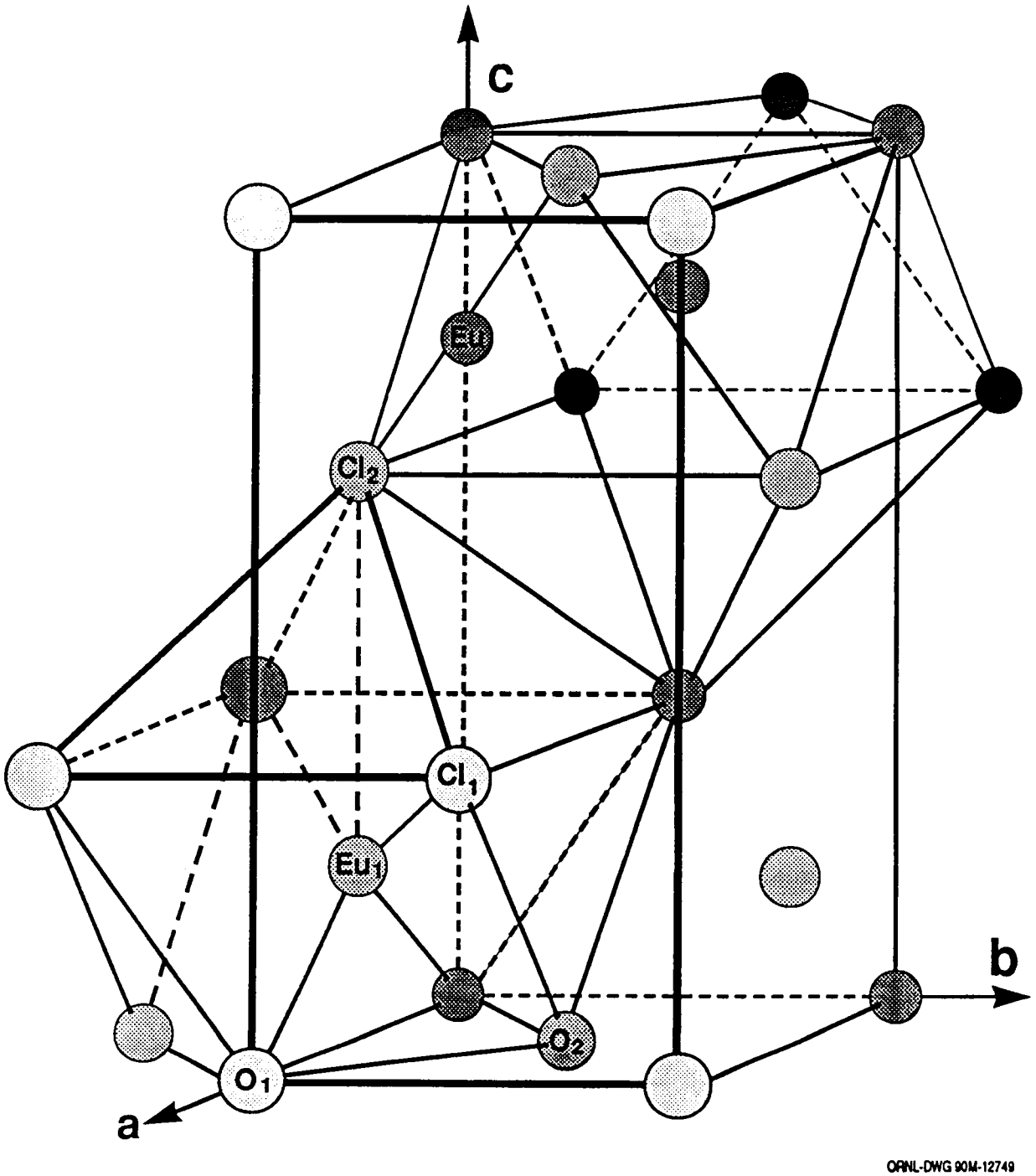

Figure 9. The Tetragonal Lead Chlofluoride-Type Unit Cell D^7_{4h}-P4/nmm. Depicted EuOCl.

in the site group and in the factor group must be considered. For the tetragonal oxyhalides the diagonal mirror plane σ_d of the site is the same element as the vertical mirror plane σ_v for the crystal. The site symmetry elements that correspond to translations for D_{2d} are E and B_2. According to the correlation tables of Fateley [33] and Wilson [35], E relates to normal modes E_g and E_u, whereas B_2 correlates with normal modes B_{1g} and A_{2u}. On the other hand, according to the correlation tables of Rosseau [34] and Douglas [40], B_2 correlates to normal modes B_{2g} and A_{2u}. The irreducible representation for the whole crystal is therefore

$$2\ A_{1g} + 3\ E_g + B_{2g}\ (\text{or}\ B_{1g}) + 3\ A_{2u} + 3\ E_u$$

including the three acoustic modes $A_{2u}\{T_z\}$ and $E_u\{T_x,T_y\}$. The gerade (sub g) vibrational modes are Raman active while the ungerade (sub u) modes are infrared active. The B_{2g} species contains the polarizability tensor α_{xy} whereas B_{1g} possesses the α_{xx}- α_{yy} tensor. A Raman peak resulting from a phonon mode with B_{2g} symmetry should be intense under (ab) polarization but weak with (aa) or (bb) polarization. A B_{1g} Raman peak is expected to be intense in (aa) or (bb) polarization but weak in (ab) polarization. The reported information on tetragonal oxychlorides is contradictory. The irreducible representation containing the B_{2g} symmetry appears in at least two publications [41,42], whereas the one containing the B_{1g} symmetry was used in four papers [43-46]. Hase [44] made the first band assignments by comparison to the experimental

data with the results of the normal coordinate and related force constants method [35]. Haeuseler [45] repeated the calculations, got different results, and to resolve the discrepancies undertook a polarized Raman study of lanthanum oxychloride [46]. The experimental observations in his work are in agreement with the present study, but there are significant discrepancies in the band assignments.

B. Results and Discussion

Polarized Raman spectra were obtained in this work from single crystal neodymium, praseodymium and europium oxychlorides. The results were completely analogous from all compounds. The Raman spectrum of PrOCl was obtained using the 514.5 nm line from the Ar-ion laser. For EuOCl and NdOCl the 488 nm and the 458 nm lines were used. The use of the 458 nm excitation resulted in a resonance enhanced Raman spectrum. The Raman spectra from the tetragonal oxychlorides consist of five of the expected six bands. This was corroborated for all the lanthanide oxychlorides from cerium to erbium. The low energy band (around 70 cm^{-1}) reported by Hase [44] was found in some of the preparations of microcrystalline LnOCl powders. Nevertheless, after more careful synthesis the band was no longer detected. It was assumed that this low energy band indicates the presence of another phase in the sample. None of the high purity single crystals exhibited this longwave mode.

The measured frequencies are presented in Table I.

Polarized Raman spectra of NdOCl or PrOCl with polarizations c(aa)b, c(bb)a , b(ab)a, b(cc)a and b(cb)a are given in Figures 10, 11, 12, 13 and 14, respectively. The b(cc)a polarizations will enhance the A_{1g} symmetry with $\alpha_{zz} > \alpha_{xx,yy}$ and, for that reason, the 183 cm^{-1} band is assigned that symmetry. Analogously, the b(bc)a polarization will strengthen the E_g modes (118 cm^{-1} and 465 cm^{-1} bands). The band at 352 cm^{-1} is enhanced under polarizations b(aa)c, c(bb)a and b(ab)a. The last mentioned polarization will intensify the B_{2g} mode, while the first two polarizations will magnify the A_{1g} symmetry with $\alpha_{xx,yy} > \alpha_{zz}$. A close look at the superimposed spectra obtained with the three previously mentioned polarizations does not show any significant change in peak position or shape. One possible explanation for these observations is that the crystals studied are not actually single crystals but an array of multiple crystals oriented in the Z direction. If that were the case, (aa) and (bb) polarizations would not be well defined and all three polarizations would be (ab)-like. In contrast, however, the precession X-ray image is sharp, indicating the presence of single crystals. Another feasible explanation is the presence of two vibrational modes A_{1g} and B_{2g} that become excited with phonons of the same energy. Because of the sharpness of the precession photograph, we assumed that the peak at 352 cm^{-1} is actually the superposition of the two vibrational modes B_{2g} and

Table I

Observed Raman Wavenumbers (cm^{-1})

Tetragonal Lanthanide Oxychlorides (D^7_{4h}-P4/nmm)

Ln	E_g	A_{1g}	E_g	A_{1g}, B_{2g}	E_g
Ce	122	186	212	322	452
Pr	119	182	214	343	456
Nd	118	183	219	352	465
Sm	118	183	226	361	488
Eu	120	182	235	357	468
Gd	120	181	236	360	510
Tb	118	177	239	384	517
Dy	117	176	239	384	527
Ho	118	175	222	377	470
Er	118	174	190	352	459
Hase[44]	A_{1g}	A_{1g}	E_g	B_{1g}	E_g
Haeuseler[46]	E_g	A_{1g}	E_g	A_{1g}	E_g

The data for Pr, Nd, Eu and Gd were obtained from single crystals; the rest of the data were acquired from microcrystalline powders.

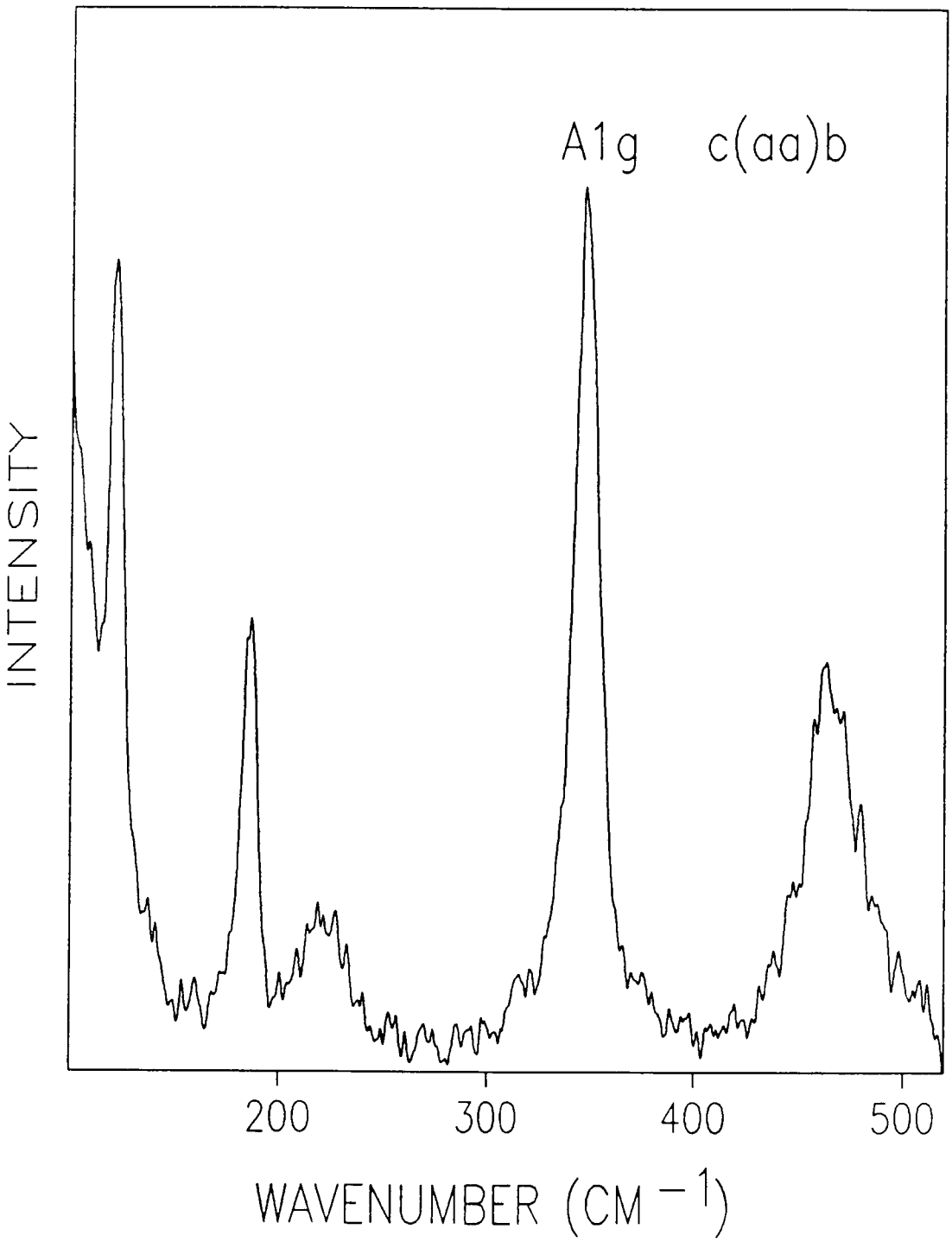

Figure 10. Polarized Raman Spectrum of PrOCl
Argon-Ion Laser 514.5 nm
Polarization c(aa)b.

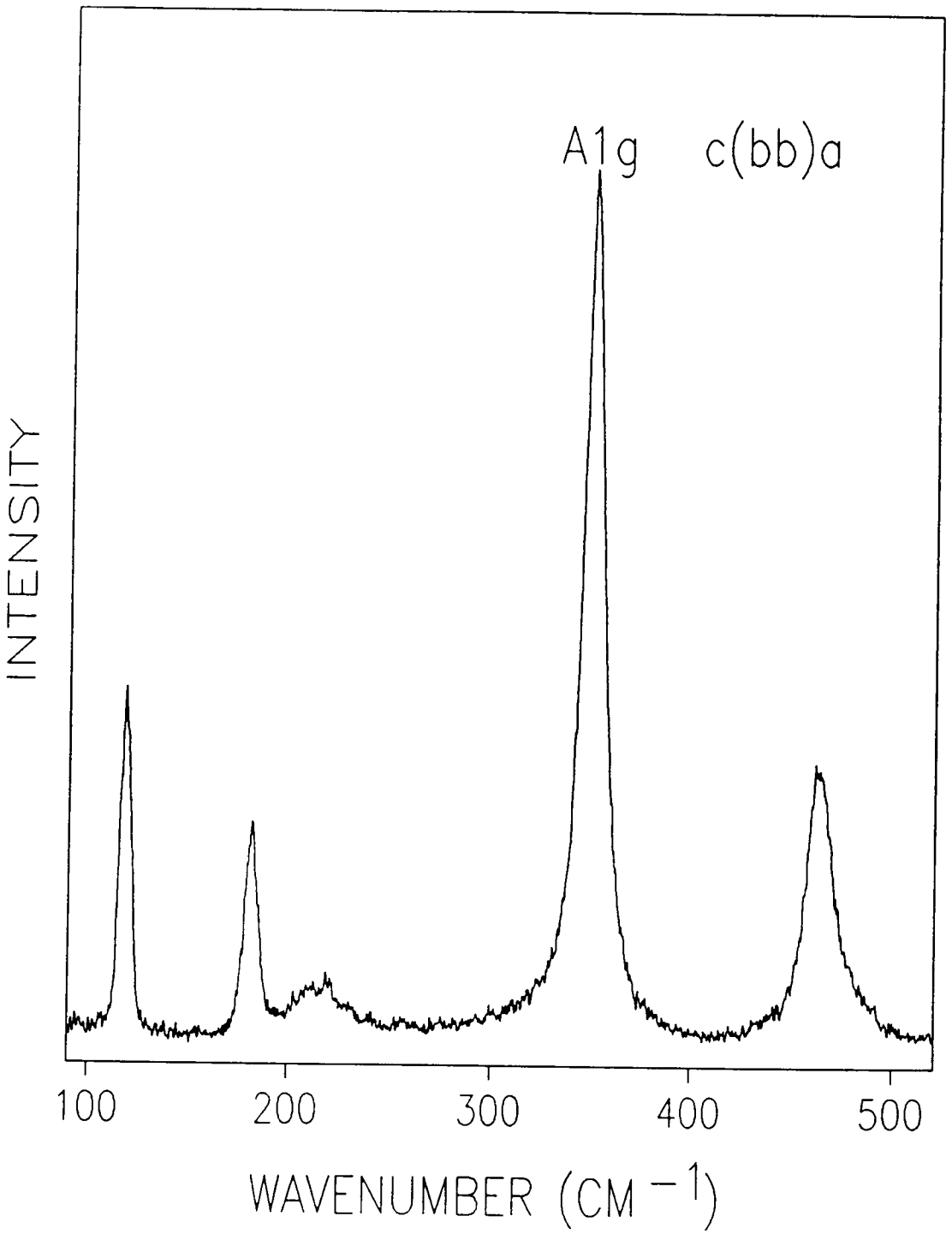

Figure 11. Polarized Raman Spectrum of NdOCl
Argon-Ion Laser 488 nm
Polarization c(bb)a.

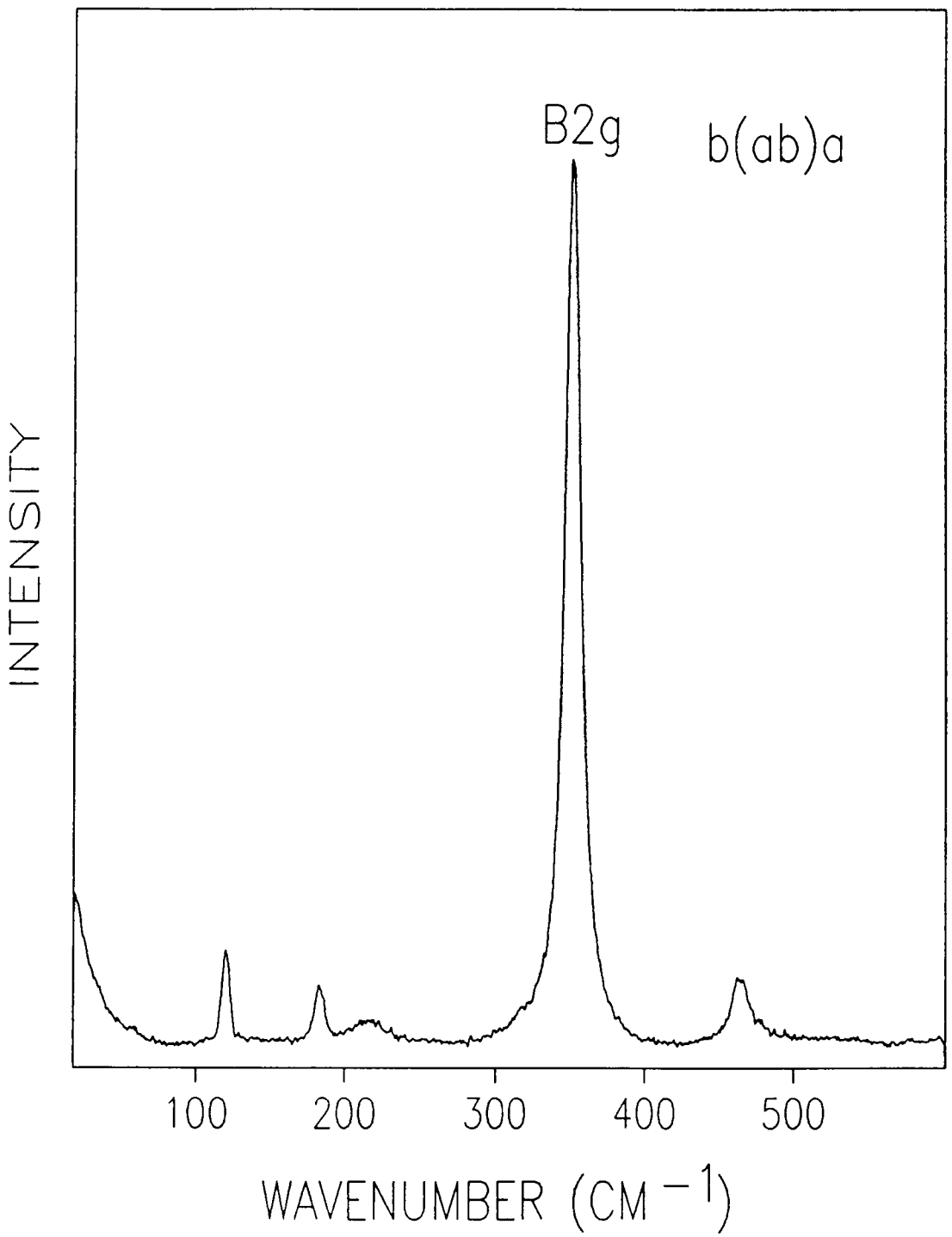

Figure 12. Polarized Raman Spectrum of NdOCl
Argon-Ion Laser 488 nm
Polarization b(ab)a.

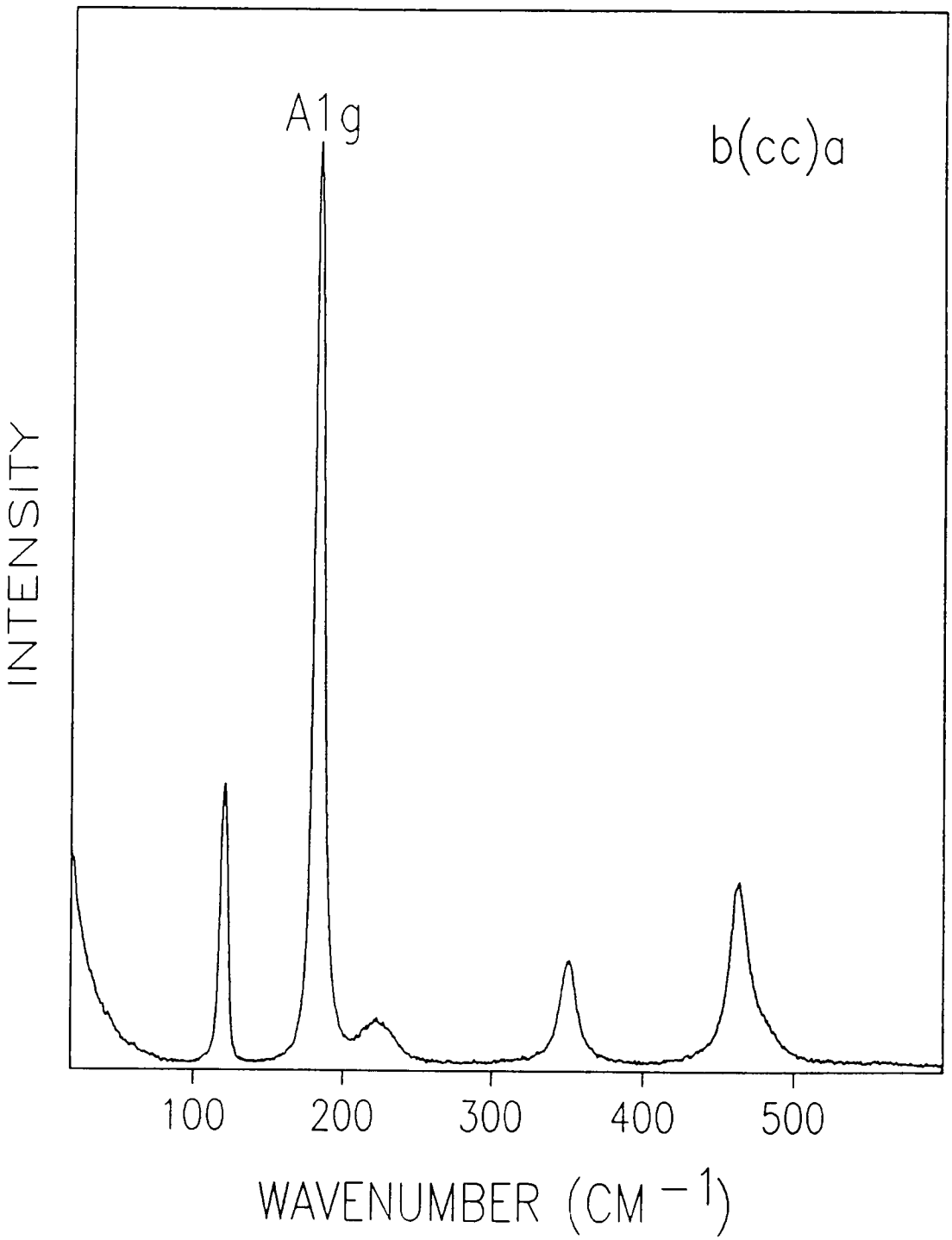

Figure 13. Polarized Raman Spectrum of NdOCl
Argon-Ion Laser 488 nm
Polarization b(cc)a.

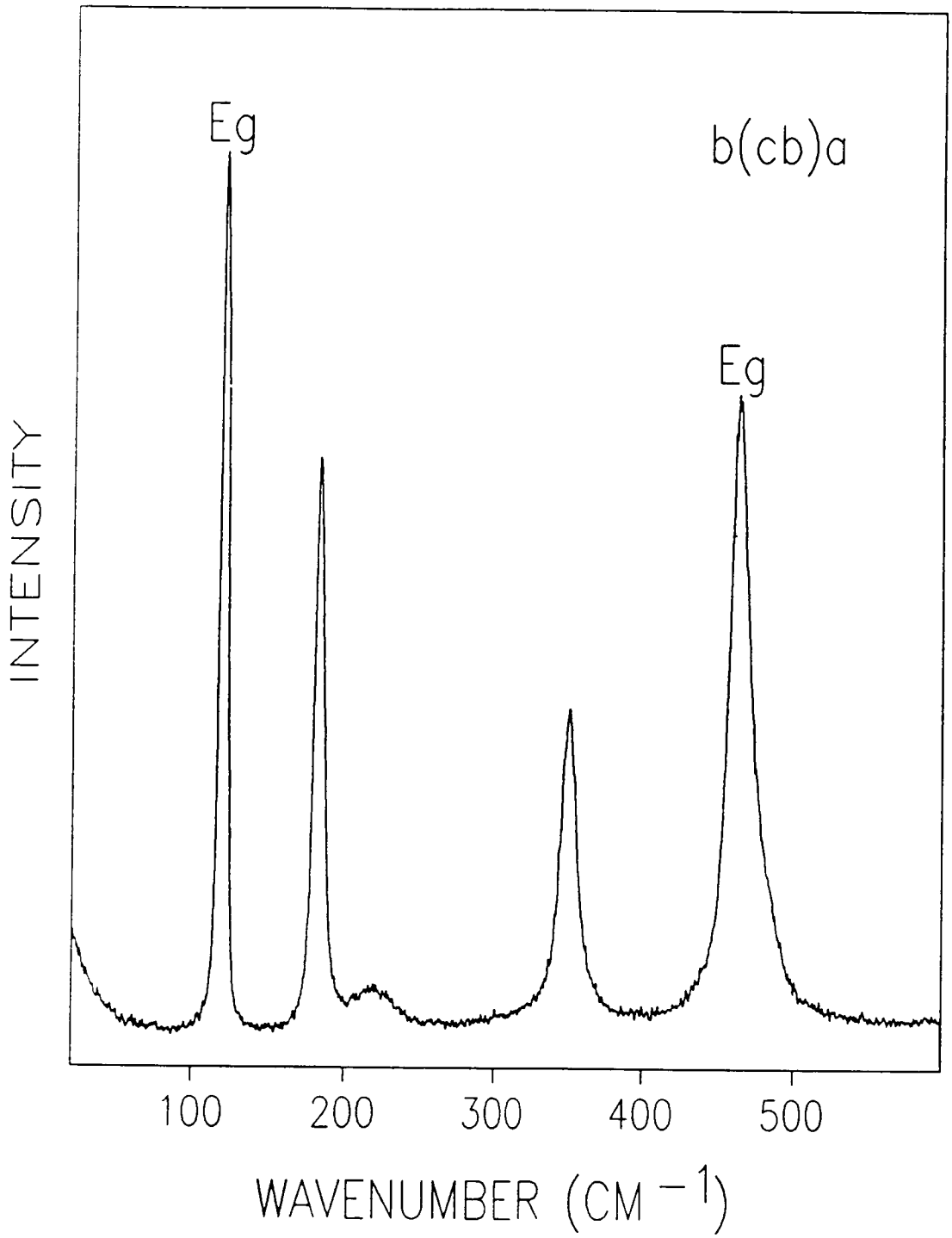

Figure 14. Polarized Raman Spectrum of NdOCl
Argon-Ion Laser 488 nm
Polarization b(cb)a.

and A_{1g}. The polarized Raman spectra from PrOCl in the present work and the polarized Raman spectra reported by Haueseler [46] display the same polarization behavior.

The weak and broad band located at 219 cm^{-1} is not clearly enhanced under any polarization. The only remaining unassigned vibrational symmetry corresponds to an E_g mode. By default and consistent with Haeuseler's work [46], the 219 cm^{-1} band is assigned the E_g symmetry.

Hase [44] reported a longwave mode in the region 65-70 cm^{-1} not observed either by Haueseler or in the present work.

Haeuseler [46] indicated a sixth band at 525 cm^{-1} in LaOCl as B_{1g}. This latter vibration is undoubtedly a combination band between the A_{1g} (189 cm^{-1} for LaOCl) and the B_{2g} component of the peak we believe consists of two components (336 cm^{-1} for LaOCl). Such a combination band would occur at the sum (525 cm^{-1}) of the individual vibration frequencies and would be enhanced under c(ab)a polarization because the B_{2g} component is enhanced by this polarization.

The symmetry assignments deduced in the present work are given at the top of Table I whereas those of Hase and Haeuseler are given at the bottom of Table I for comparison.

In the present work on EuOCl, a weak and broad band at 225 cm^{-1} is partially resolved with respect to a second band at 235 cm^{-1} (see Figure 15). This new band at 225 cm^{-1} is very likely due to an electronic Raman transition between the $^7F_1(A_2)$ level and the $^7F_0(A_1)$ ground state caused by electron-

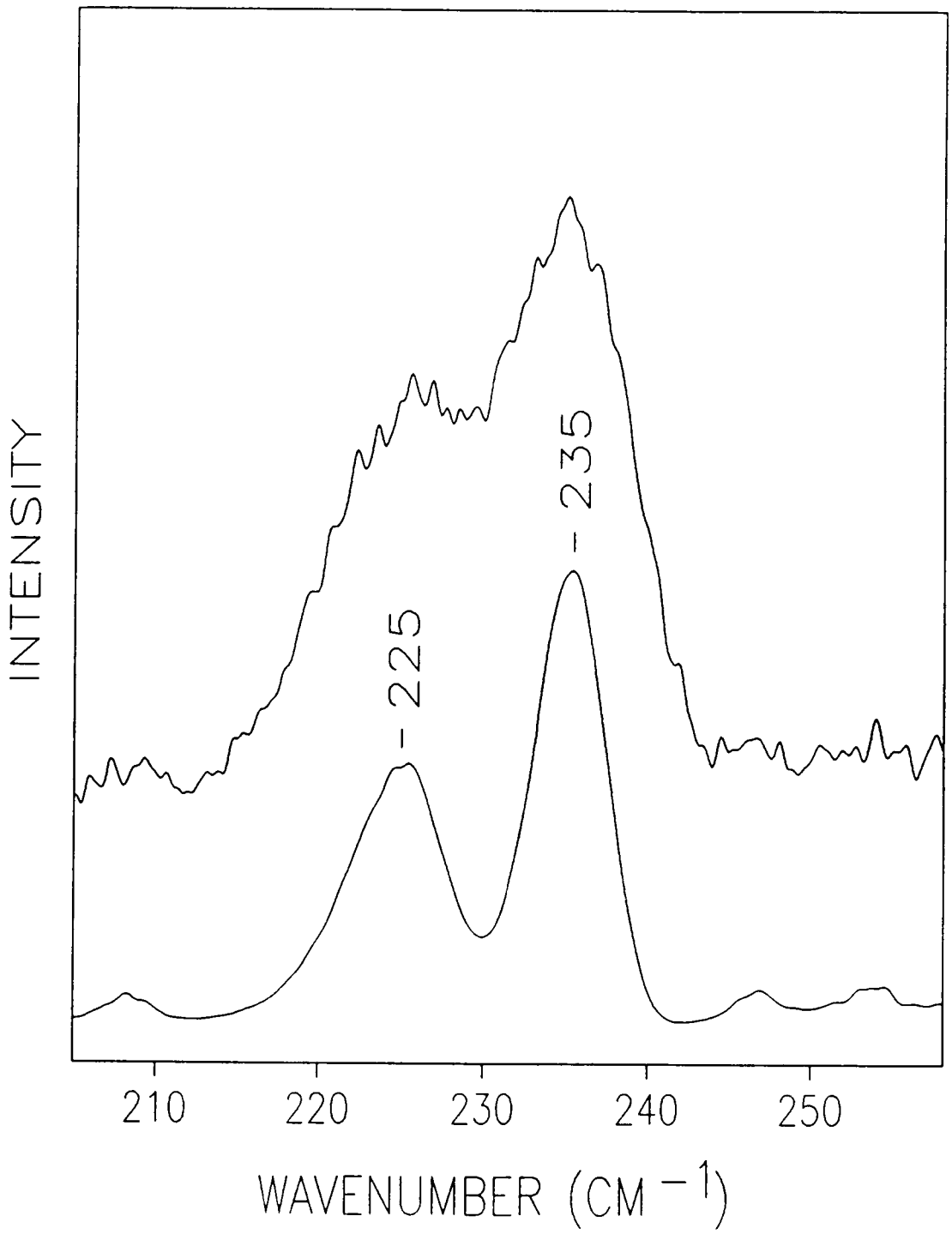

Figure 15. Raman and Electronic Raman Transitions in EuOCl. Ar-Ion Laser 488 nm.

phonon coupling reinforced by the near degeneracy of the electronic and vibrational states. The occurrence of electron-phonon coupling has been previously observed and documented in erbium [47] and ytterbium orthophosphates [48]. Examination of Raman spectra from europium orthophosphate previously obtained in the Transuranium Research Laboratory also revealed the presence of such electronic Raman transitions.

C. Conclusions

Analysis of the polarized Raman spectra from PrOCl and NdOCl clearly showed that the correct irreducible representation contains the B_{2g} symmetry. The symmetries of three of the six Raman-active bands are well determined. There is one band that displays two polarizations, and one band that has no clear polarization and is assigned as E_g by default. The EuOCl Raman spectrum displays a weak electronic Raman band which originates in electron-phonon coupling due to the closeness between the vibrational and electronic eigenvalues.

CHAPTER IV

RESULTS AND DISCUSSION: LUMINESCENCE, ABSORBANCE AND ELECTRONIC RAMAN STUDIES OF SINGLE-CRYSTAL EUROPIUM OXYCHLORIDE

A. Introduction

Lanthanide luminescence has been observed and studied for many years, resulting in extensive applications for phosphors and many lasers [49,50]. The optical properties of the lanthanide ions originate from the internal 4f electrons. The 4f electrons in the lanthanide ions occupy inner orbits surrounded by the external 5s and 5p electrons, in contrast to the case of the transition metal ions where the optically active electrons belong to the partially filled nd shell and occupy external orbits. Because of this shielding from external electrical fields, the effect of the crystal field on lanthanide ions due to neighboring ions is small. As a first approximation, the electronic configuration of the lanthanides can be described using the Russell-Saunders angular momentum coupling scheme. The wavefunctions of the 4f electrons are first calculated neglecting the angular interactions between 4f electrons and solving the system for each of the 4f electrons in the central field of the nucleus, the inner and outer filled shells of electrons, and the spherical part of the other 4f electrons. Next the nonspherical interactions

among the 4f electrons are considered and the resulting eigenstates labelled by their values of total spin S and total orbital angular momentum L according to the notation ^{2S+1}L. Spin-orbit coupling (on the order of 2000 cm^{-1}) is much larger than crystal field effects (50-150 cm^{-1}), so its effect must be considered first (weak field approximation). The resultant electronic states due to spin-orbit coupling are characterized by a resultant total angular momentum with quantum number J. The "ground state" or lowest energy arrangement of the electrons is determined according to Hund's rules by the maximum spin multiplicity 2S+1 ,the maximum resultant of the angular momentum L consistent with the greatest multiplicity, and $J=|L-S|$ if the f orbitals are less than half full or $J=|L+S|$ if the f orbitals are more than half full. In spectroscopic notation the state is labeled $^{2S+1}L_J$. The effect of the crystal field on the isolated ion is to remove the 2J+1 degeneracy of such a state (by 50-150 cm^{-1}), thus generating a splitting of the energy level that contains information about the ligand symmetry.

There is a more subtle but very important consequence of the crystal field influence. The energy levels of the lanthanide ions in the optical range all belong to the same $4f^n$ configuration, and so these energy levels have the same parity and thus electric dipole transitions are consequently forbidden. Nevertheless if the rare-earth ion is in a site with no center of inversion, the crystal field will contain

odd components which will mix some $4f^{n-1}5d$ states into the $4f^n$'s so that the parity selection rule for electric dipole transitions will be partially relaxed. Even if the lanthanide ion is in a symmetric crystal field, any odd parity vibration which is dynamically coupled to the electronic transition can destroy the inversion symmetry and again partially relax the selection rule that becomes $\Delta J \leq 6$. If the initial or the final state is J=0, the selection rule is $\Delta J = 2, 4$ or 6 [51-53]. Magnetic dipole transitions are parity allowed and obey the selection rule $\Delta L, \Delta J \leq 1$ (except $J=0 \rightarrow J=0$ which is forbidden). Quadrupole transitions are in principle parity allowed; nevertheless there are no reports of their occurrence.

The emission and absorbance spectra of lanthanide compounds in general consist of sharp peaks containing a fine structure which results from the influence of the lanthanide ion's environment. The emission spectrum which results from light excitation is called the photoluminescence spectrum. The use of a tunable laser as an excitation source has many practical advantages including its inherent high intensity and specificity due to the possibility of choosing the wavelength of the exciting beam to match a known energy level. The study of the splitting patterns of the luminescence peaks provides information about the central ion symmetry. This knowledge can be further enhanced by analysis of the polarization of the emissions. Also, the strength or absence of a given transition will depend in part upon the symmetry of the crystal field.

Certain transitions, called "hypersensitive," exhibit widely varying intensity depending sensitively upon the local metal ion environment. The mechanism proposed to explain this behavior involves a coupling of the 4f electrons with transient dipoles induced in the ligand by the electromagnetic radiation field [53,54].

The photoluminescence spectrum of a lanthanide cannot only provide information about the metal ion site symmetry in a pure compound, but it can also provide the same information about a host material into which the lanthanide has been doped. The splitting pattern analysis can be facilitated by choosing a favorable lanthanide ion as a structural probe. The desirable characteristics are a high radiative yield and a relatively easy to interpret scheme of energy levels. One excellent candidate as a dopant is Eu^{III}. Because the ground state is J=0, the analysis of the transitions is relatively simple, while the yield of the radiative transitions remains relatively high due to the ample energy gap between excited and ground states. A rule of thumb to determine if the main decay processes are radiative or nonradiative is the number of phonons to be involved for the nonradiative de-excitation. If the gap between a given excited state and the lowest energy state can be bridged by seven phonons or less, the excited state will decay mainly without emission of light [55]. Assuming that the active phonons of highest energy typically have energies around 500 cm^{-1}, the critical energy gap is in

the range of 3000-4000 cm^{-1}.

The coordination number for lanthanide and actinide compounds is usually between eight and ten. The symmetry relations between the coordination polyhedra and the luminescent transitions for Eu^{III}-containing compounds with the usual geometries for coordination numbers eight to ten are given in Table II.

B. Results and Discussion

Previous luminescence and absorption spectroscopic studies of the tetragonal oxychlorides were performed on LnOCl microcrystalline powders doped with Eu^{III} [56,59]. Such studies preclude the use of polarization measurements for symmetry assignments of the electronic bands. In many cases [55], it is found that increasing the concentration of dopant ions above a certain critical value produces a reduction, or quenching, of the luminescence. This phenomenon is due to multiple energy transfer between ions (which can involve about a million ions) before radiation is emitted. The energy flow can reach crystal defects or impurities that act as an energy sink or quenching trap and then de-excite by multiphoton modes (IR emission) or by multiphonon emission without radiation of light. This energy transfer should have a low efficiency among lanthanide ions because of the weak interaction of the 4f electrons with their environment. For that reason, the luminescence of pure,

Table II

Symmetry Relations Between Coordination Polyhedra and Luminescence Transitions for Europium(III) Containing Compounds

Coordination Polyhedron (CN)[b]	Site Symmetry	Active Representations[a]			
		$^7F_4 \leftarrow {}^5D_0$	$^7F_3 \leftarrow {}^5D_0$	$^7F_2 \leftarrow {}^5D_0$	$^7F_1 \leftarrow {}^5D_0$
Square Antiprism(8)	D_{4d}	B_2, E_1	E_1	E_1	A_2
	D_4	$A_2, 2E$	$3A_2, 2E$	E	A_2, E
	D_2	$2B_1, 2B_2, 2B_3$	$2B_1, 2B_2, 2B_3$	B_1, B_2, B_3	B_1, B_2, B_3
Triangulated Dodecahedron (8)	D_{2d}	$B_2, 2E$	$B_2, 2E$	B_2, E	A_2, E
	D_2	$2B_1, 2B_2, 2B_3$	$2B_1, 2B_2, 2B_3$	B_1, B_2, B_3	B_1, B_2, B_3
	S_4	$2B, 2E$	$2B, 2E$	$2B, E$	A, E
Tricapped Trigonal Prism (9)	D_{3h}	$3E'$	$2E'$	$2E'$	A_2'
	D_3	$A_1, 3E$	$2A_2, 2E$	$2E$	A_2, E
	S_6	$2A_u, E_u$	$2A_u, E_u$	E_u	A_g
	C_{3h}	$3E'$	$2E'$	E'	A', E''
	C_3	$3A, 3E$	$3A, 2E$	$A, 2E$	A, E
Monocapped Square Antiprism (9)	C_{4v}	$2A_1, 2E$	$2E$	A_1, E	A_2, E
	C_4	$3A, 2E$	$A, 2E$	A, E	A, E
	C_2	$5A, 4B$	$3A, 4B$	$3A, 2B$	$A, 2B$
Bicapped Square Antiprism (10)	D_{4d}	B_2, E_1	E_1	E_1	A_2
	D_{2d}	$B_2, 2E$	$B_2, 2E$	B_2, E	A_2, E
	D_2	$2B_1, 2B_2, 2B_2$	$2B_1, 2B_2, 2B_2$	B_1, B_2, B_3	B_1, B_2, B_3

[a]Magnetic-dipole selection rules were employed for the $^7F_1 \leftarrow {}^5D_0$ transition, and electric-dipole rules for the others.

[b]CN = coordination number.

single-crystal EuOCl was explored in the present work. Using the argon-ion laser line at 465.7 nm, the $^5D_1$ was excited allowing the polarized study of the transitions to the $^5D_0$ and $^7F_{1,2,3,4,6}$ levels. Although a suitable UV excitation source was unavailable, luminescence from the $^5D_{1,2,3}$ levels was obtained by resonance enhanced two-photon excitation. The excitation source for the latter was a tunable dye-laser containing rhodamine 6G and pumped with the argon-ion laser in the multiline mode. The dye-laser was tuned to excite the $^5D_0$ level, and lifetime measurements indicated that its half-life is about 10 μs ensuring sufficient population of this level. From the $^5D_0$ level a second photon can be absorbed to excite charge-transfer states (CTS). This last transition is fully allowed, so the absorption of the first photon involving the forbidden $^7F_0 \rightarrow {}^5D_0$ transition is the rate-determining step. The de-excitation of the CTS proceeds initially mainly by multiphonon decay to the ^5D levels, because of the closely spaced upper energy levels, and is followed by a photoluminescence cascade toward the ground state. The upper energy levels $^5L_{6,7,8}$, $^5G_{2,3,4,5,6}$ and $^5D_4$ were examined by absorption spectroscopy. Additionally, as mentioned in Chapter III, the $^7F_1(A_2) \rightarrow {}^7F_0$ transition was observed by electronic Raman.

The polarized one-photon luminescence and unpolarized two-photon luminescence measurements were conducted at room temperature, along with the absorption spectrum. These results

are displayed in Figures 16 to 24. The one and two-photon luminescence spectra were also recorded at liquid nitrogen temperature (77 K) and used for crystal-field parameters calculations. The Raman spectrum that exhibits the electronic Raman transition is displayed in Figure 15 (page 45).

To analyze the data the character table for the Eu^{III} C_{4v} site symmetry and the group theory selection rules must be used. The C_{4v} character table is given in Table III. In Table IV are presented the number and symmetry designation for all the Stark levels for the C_{4v} site symmetry for J=0 to 8. The selection rules for electric dipole transitions (that transform according to the translation x,y and z) and magnetic dipole transitions (that transform according to the rotations about x,y and z) are shown in Tables V and VI, respectively. The presence of an entry on a given row and column in Tables V and VI signifies that the involved transition should be oberved and that its intensity will be higher with the polarizer in the indicated orientation. The absence of an entry means that the transition is forbidden. The polarized luminescence experiment was carried out using a polarizer before the monochromator either parallel or perpendicular to the z axis. The multiplets due to transitions between the $^5D_0$ and $^7F_{0,1,2,3,4}$ levels were easily identified. Initially, there was some uncertainty in the assignment of the other bands because they were not only weaker but suffered from superimposition with other manifolds. The process utilized to

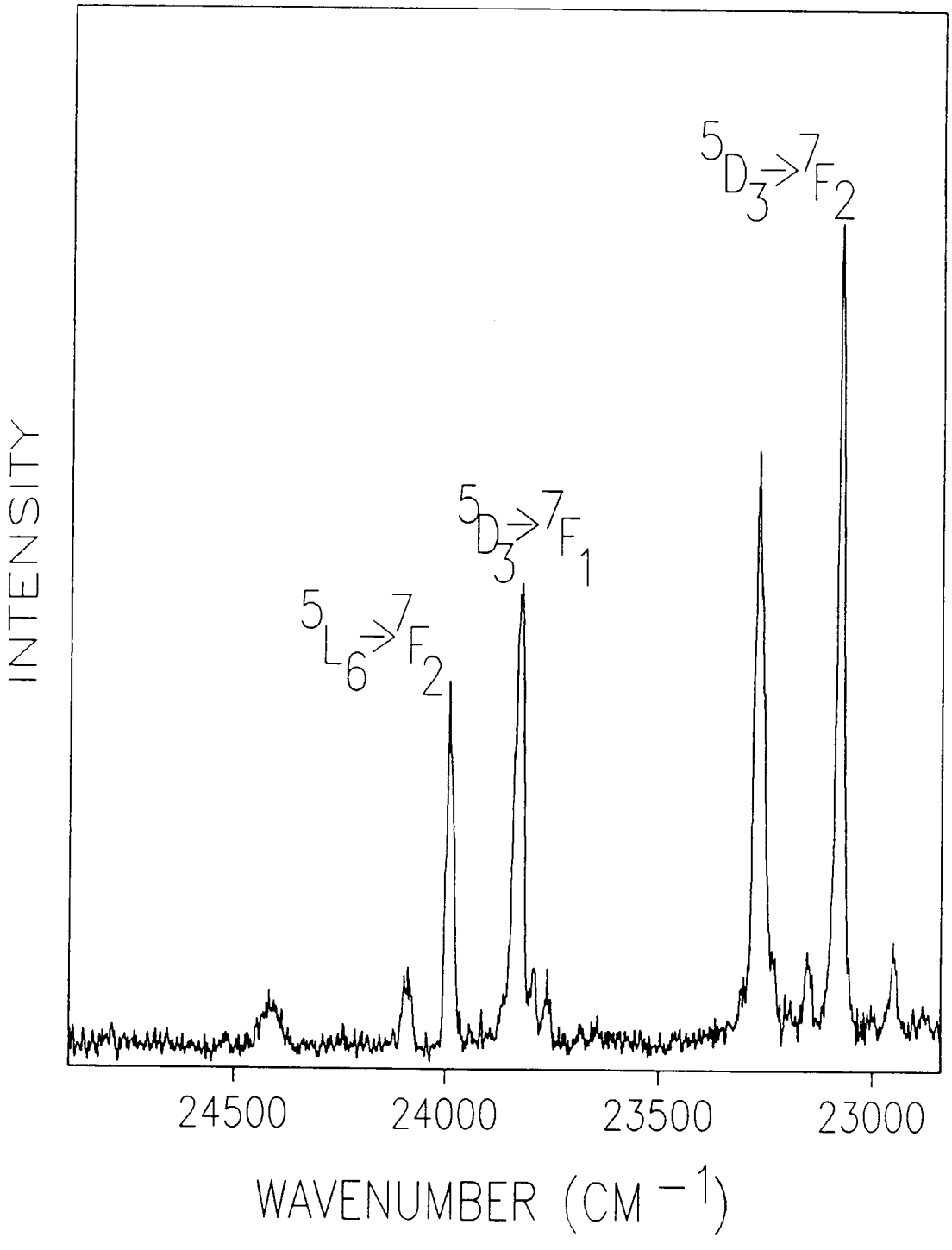

Figure 16. Polarized Luminescence Spectrum of EuOCl Showing Emission from the $^5D_2$ and $^5D_1$ to ^7F's Levels. The Electric Vector is Perpendicular to the Z Axis. Argon-Ion Laser Excitation (465.8 nm).

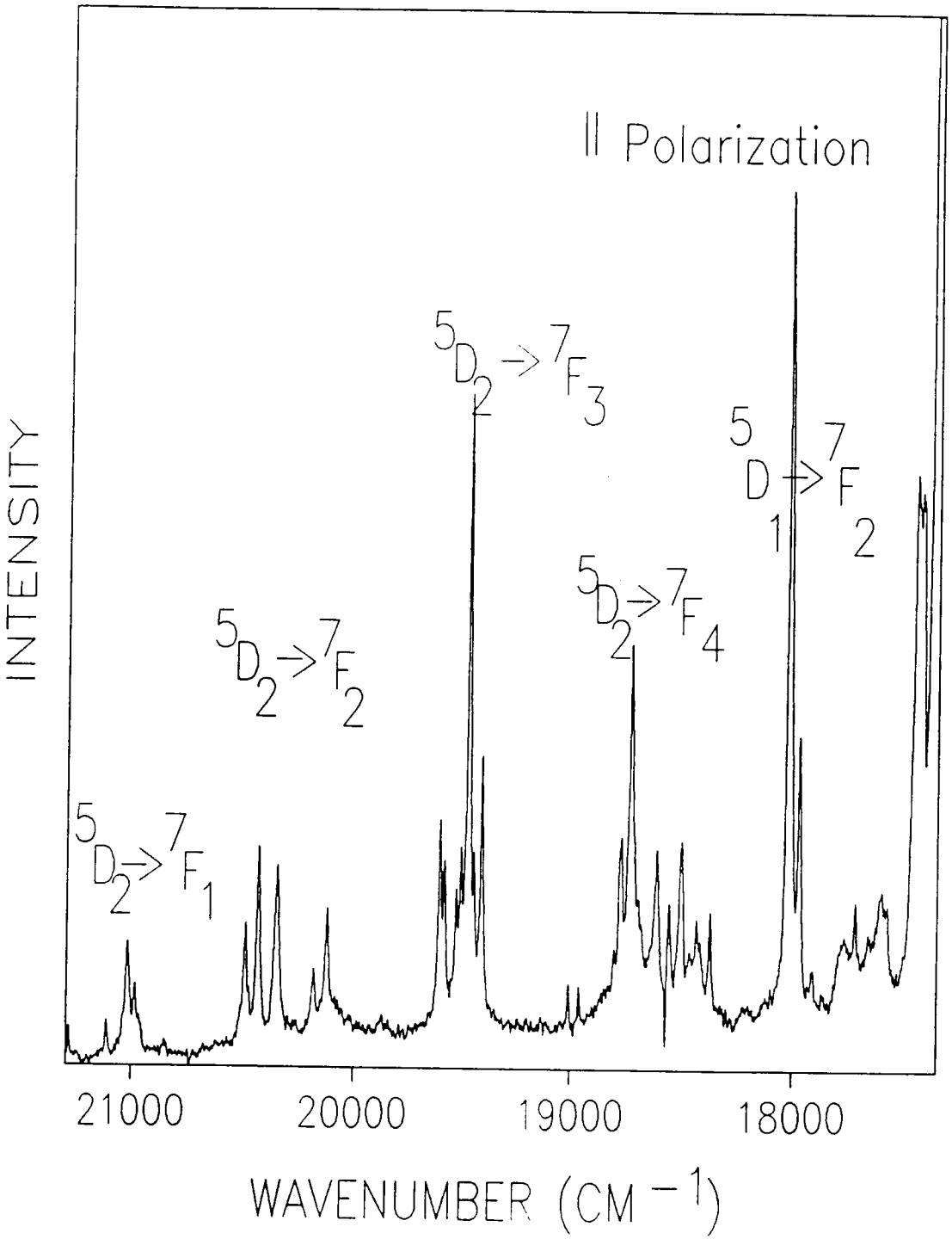

Figure 17. Polarized Luminescence Spectrum of EuOCl Showing Emission from the $^5D_2$ and $^5D_1$ to ^7F's Levels. The Electric Vector is Parallel to the Z Axis. Argon-Ion Laser Excitation (465.8 nm).

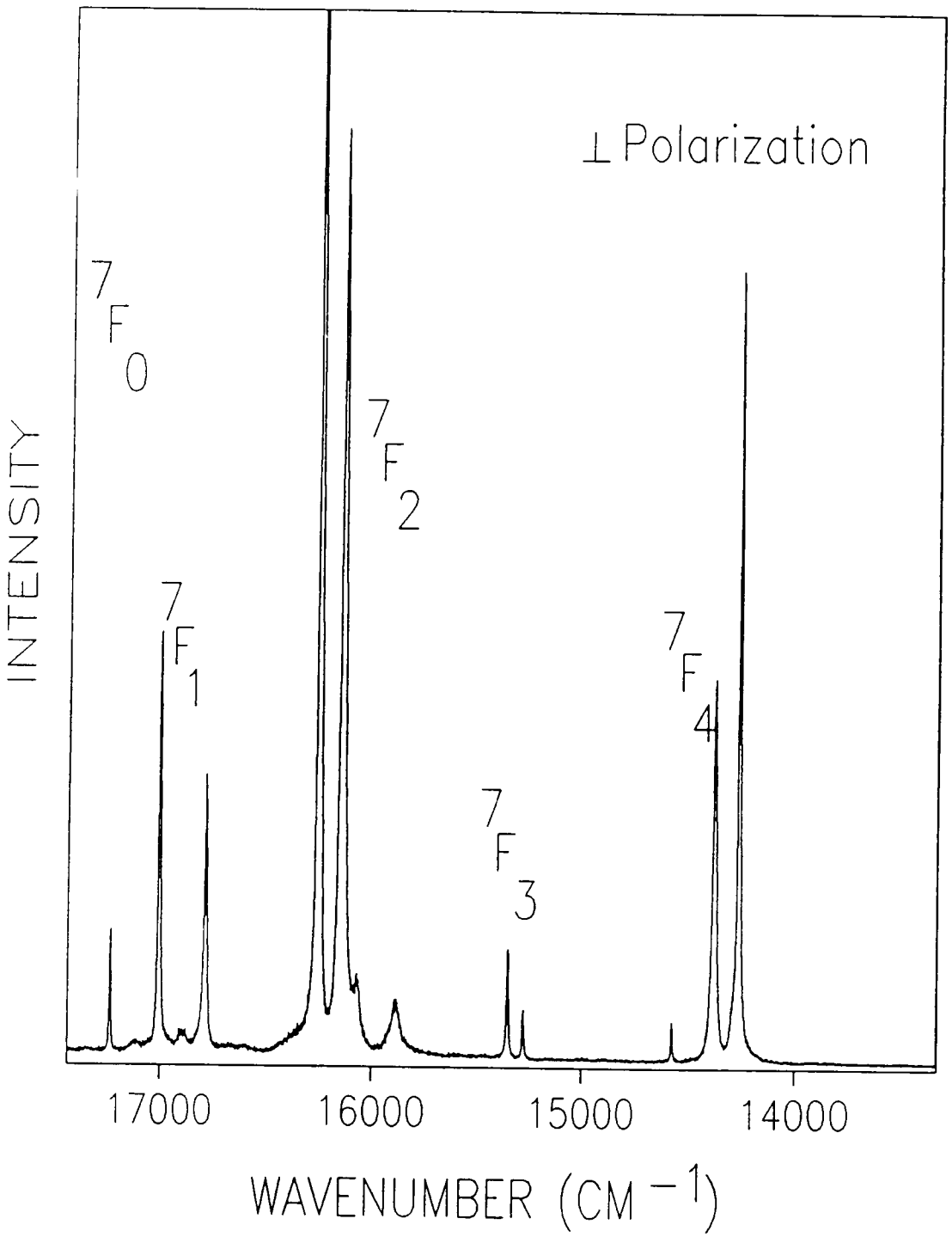

Figure 18. Polarized Luminescence Spectrum of EuOCl Showing Emission from the $^5D_0$ Level to the $^7F_{0-4}$ Levels. The Electric Vector is Perpendicular to the Z Axis. Argon-Ion Laser Excitation (465.8 nm).

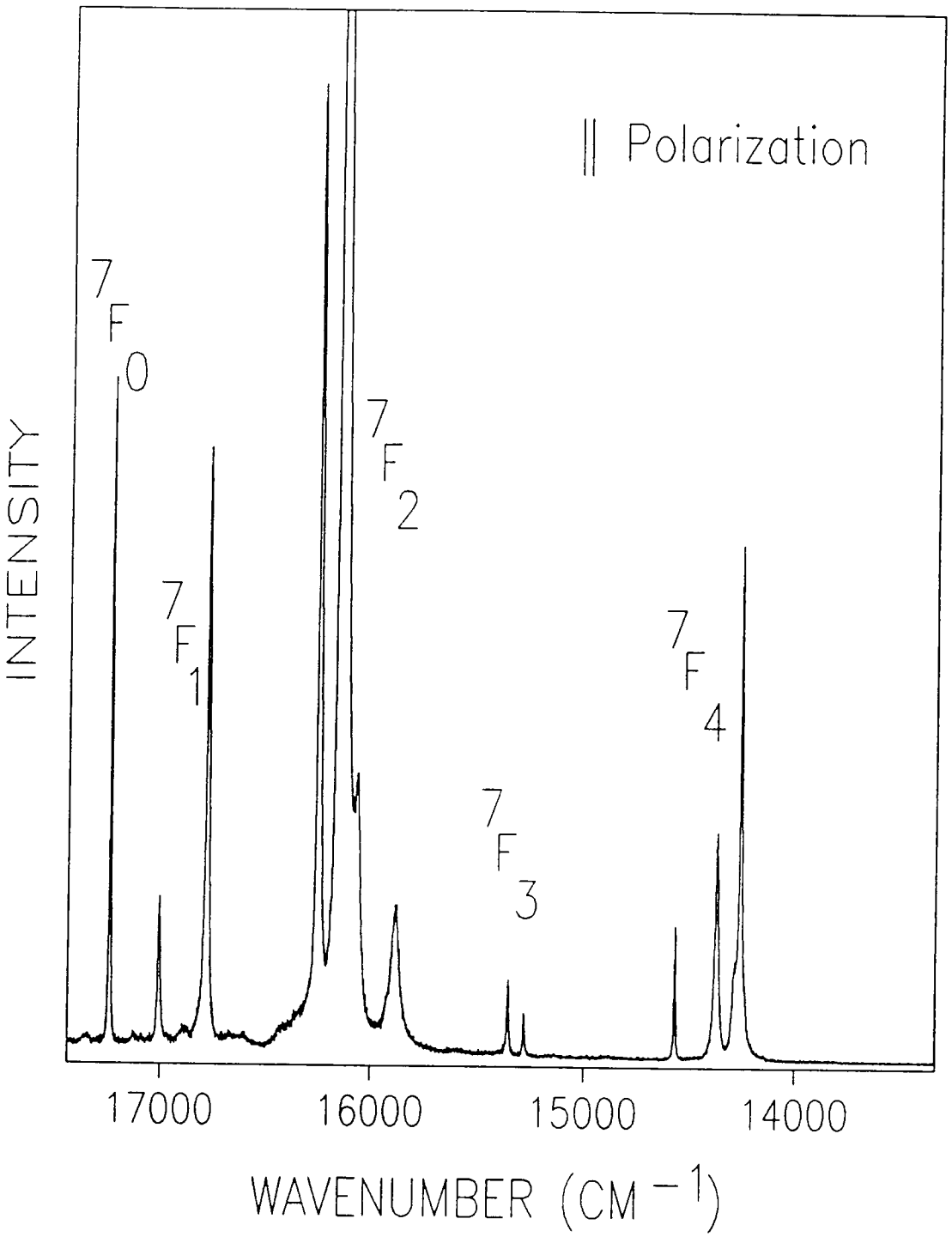

Figure 19. Polarized Luminescence Spectrum of EuOCl Showing Emission from the $^5D_0$ Level to the $^7F_{0-4}$ Levels. The Electric Vector is Parallel to the Z Axis. Argon-Ion Laser Excitation (465.8 nm).

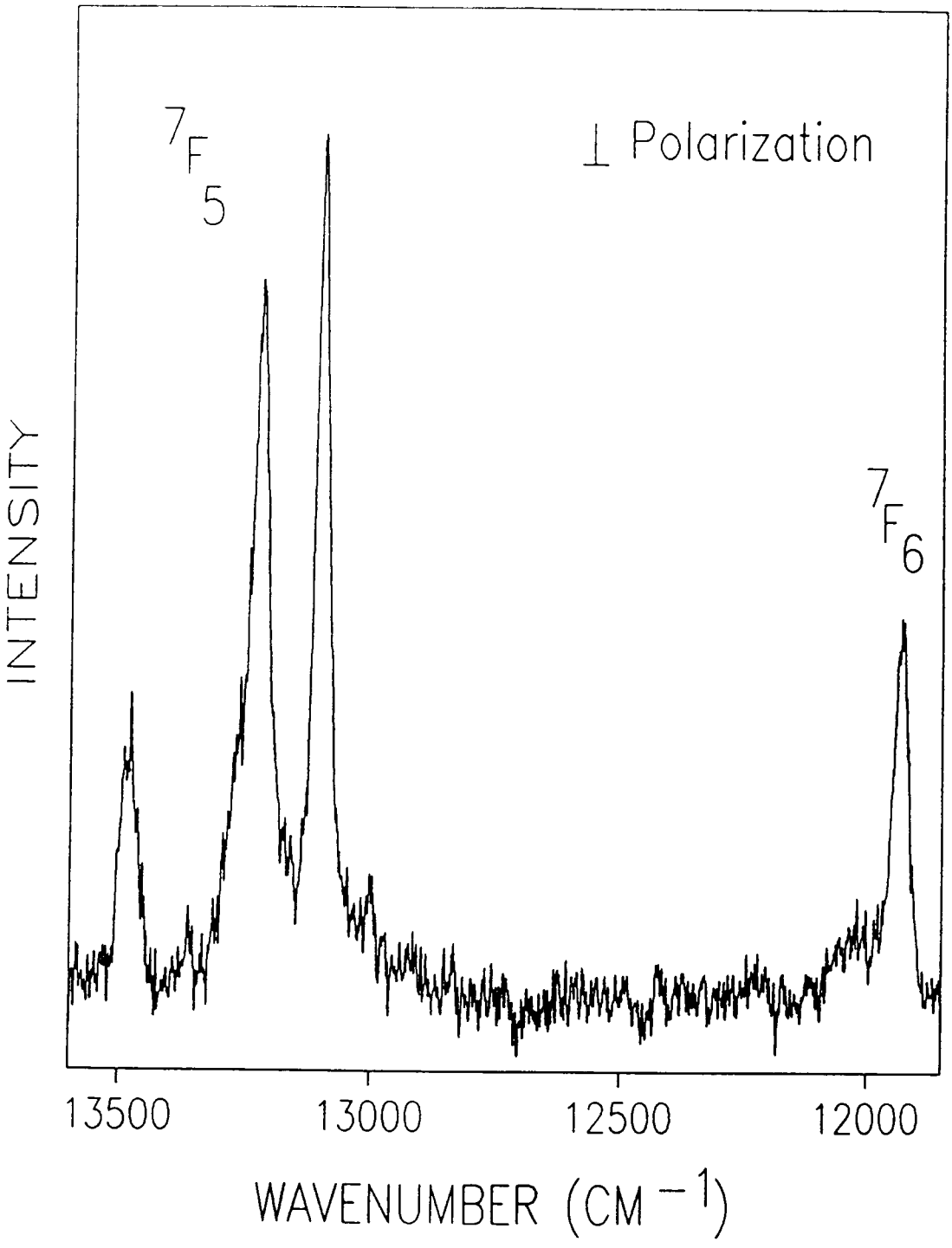

Figure 20. Polarized Luminescence Spectrum of EuOCl Showing Emission from the $^5D_0$ Level to the $^7F_{5,6}$ Levels. The Electric Vector is Perpendicular to the Z Axis. Argon-Ion Laser Excitation (465.8 nm).

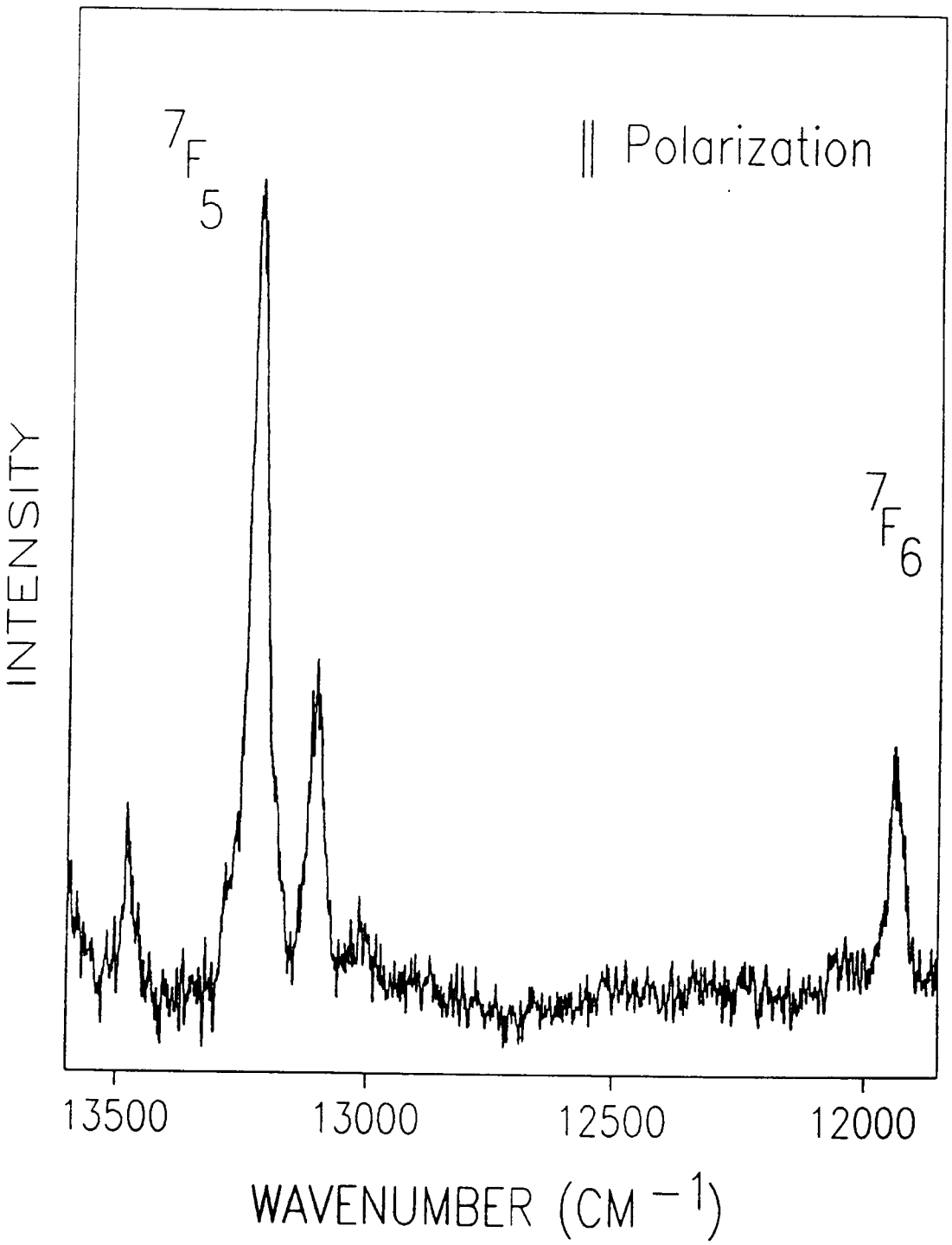

Figure 21. Polarized Luminescence Spectrum of EuOCl Showing Emission from the $^5D_0$ Level to the $^7F_{5,6}$ Levels. The Electric Vector is Parallel to the Z axis. Argon-Ion Laser Excitation (465.8 nm).

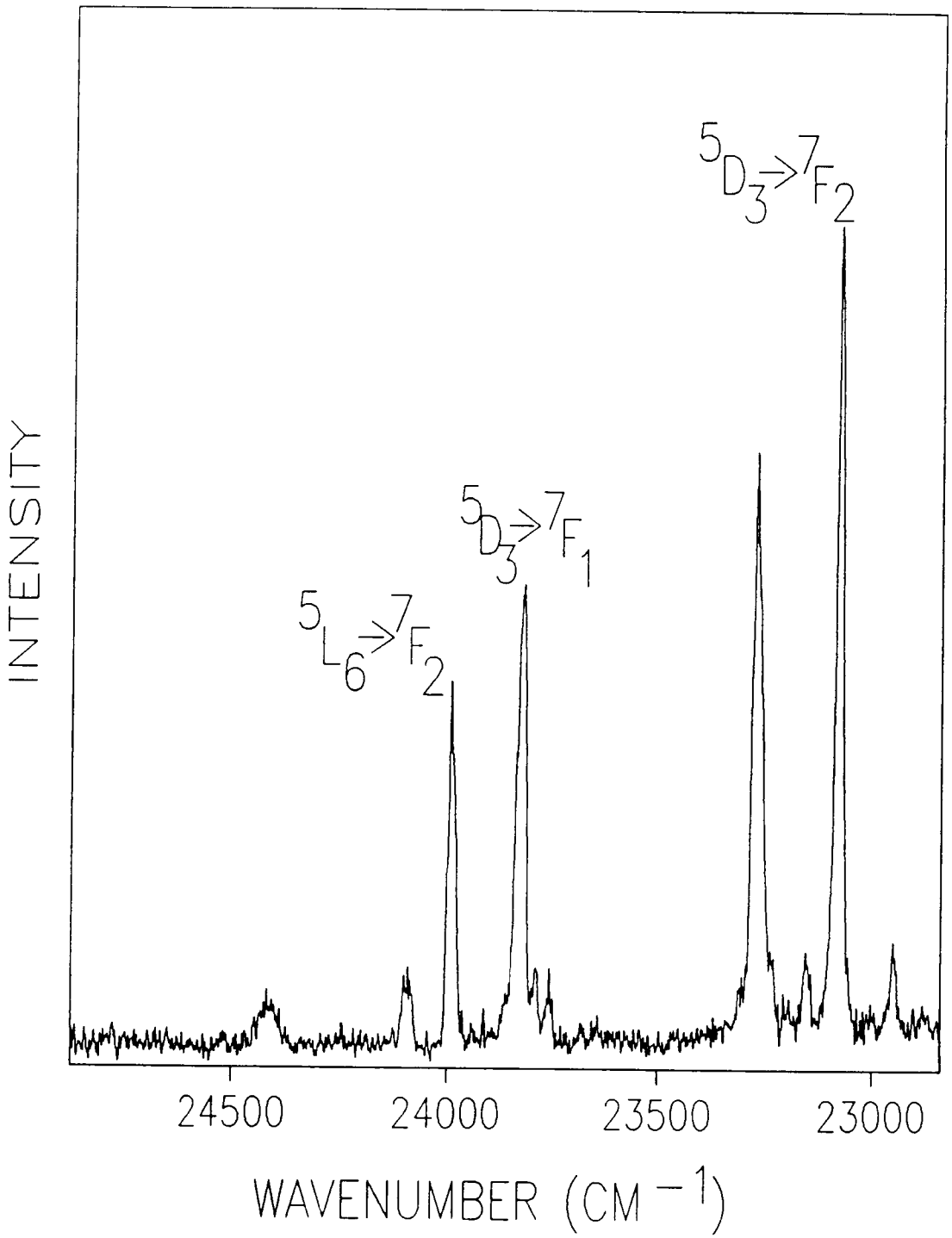

Figure 22. Two-Photon Luminescence Spectrum of EuOCl Showing Emission from Some High Lying Levels in the 25-23K cm^{-1} Region. Dye Laser Excitation (Tuned to the $^5D_0$ Level).

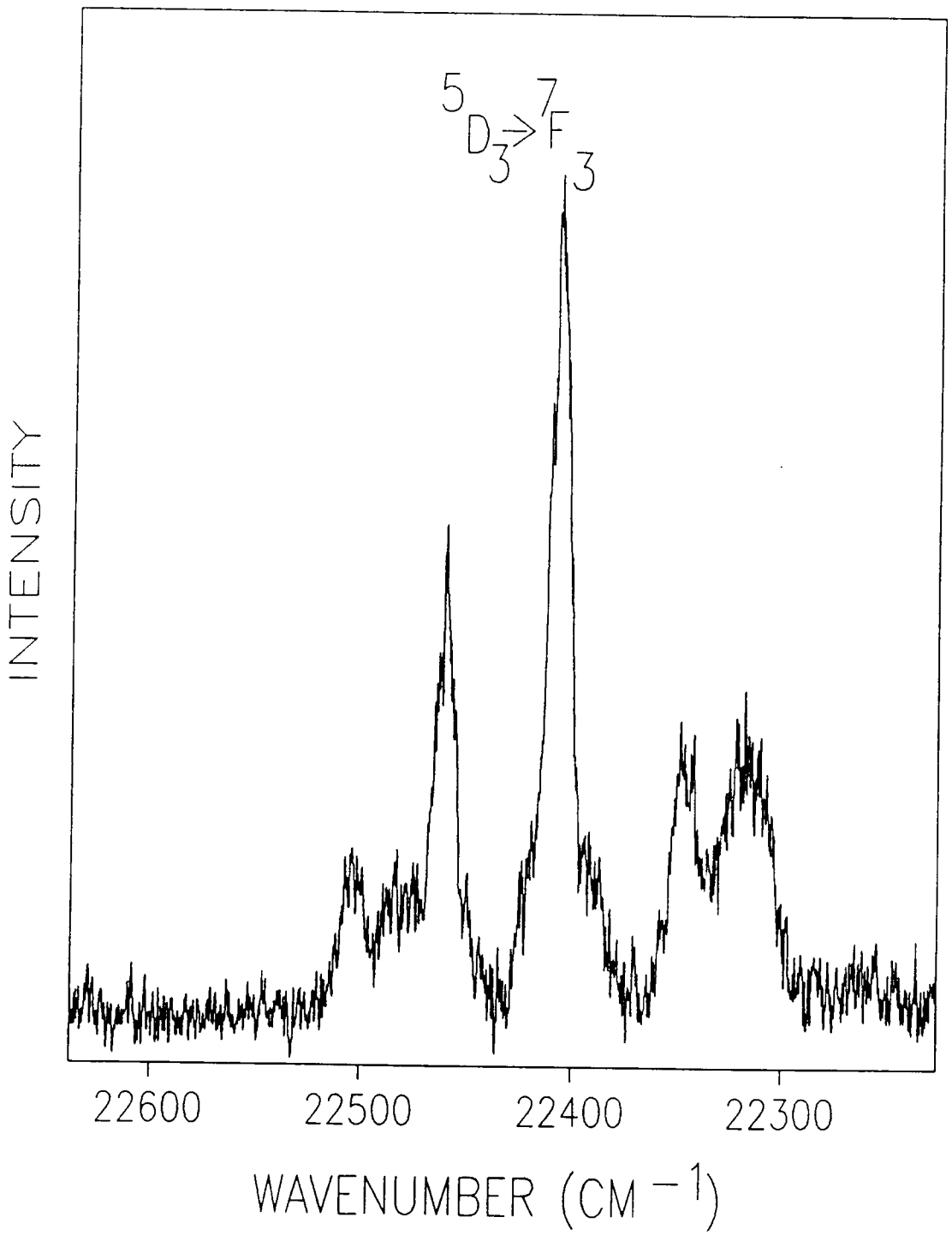

Figure 23. Two-Photon Luminescence Spectrum of EuOCl Showing Emission from the $^5D_3$ to the $^7F_3$ Levels. Dye-Laser Excitation (Tuned to the $^5D_0$ Level).

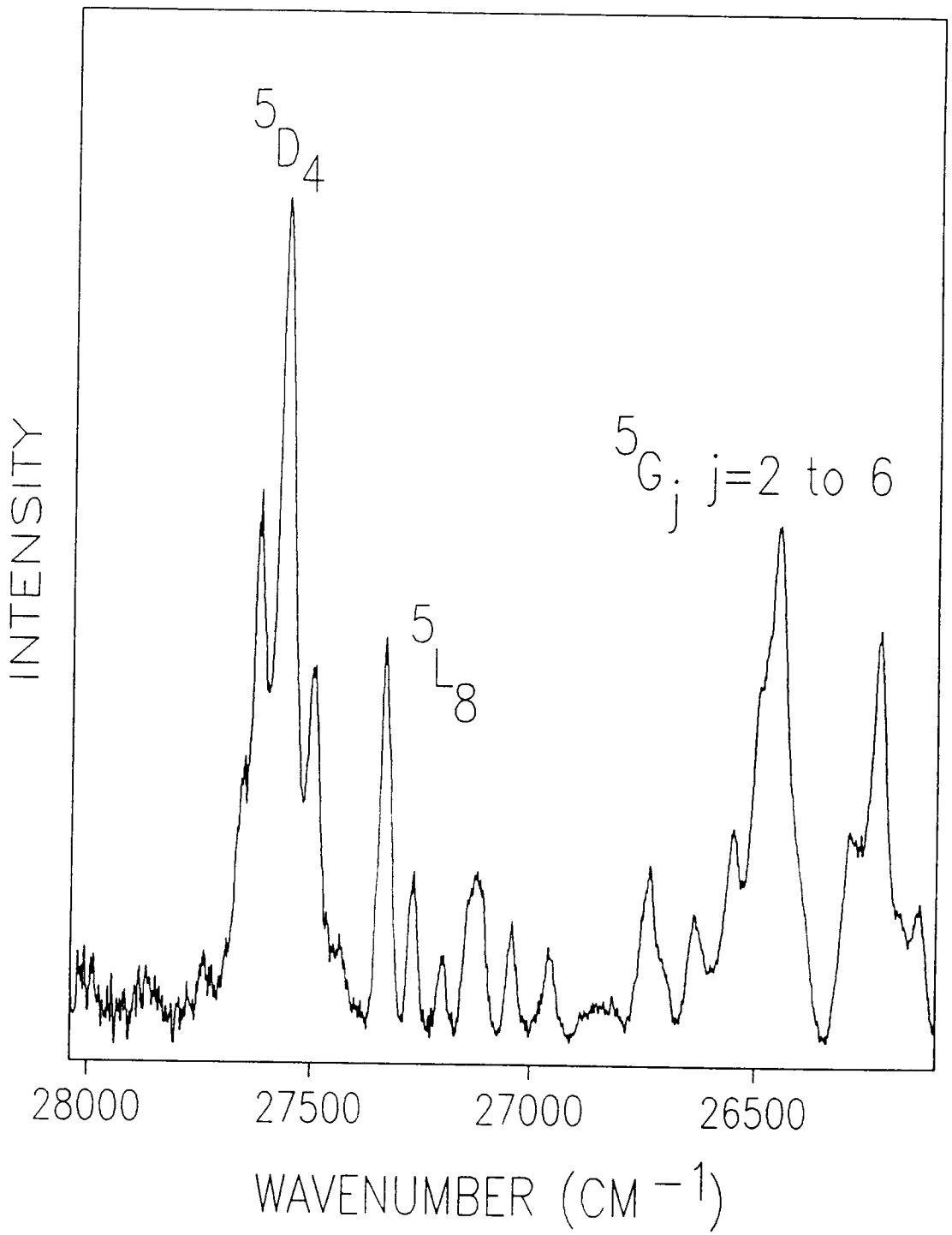

Figure 24. Absorption Spectrum of EuOCl in the 28-26K cm^{-1} Region.

Table III

C_{4v} Character Table

C_{4v}	E	$2C_4$	C_2	$2\sigma_v$	$2\sigma_d$	
A_1	1	1	1	1	1	T_z
A_2	1	1	1	-1	-1	R_z
B_1	1	-1	1	1	-1	
B_2	1	-1	1	-1	1	
E	2	0	-2	0	0	$(T_x,T_y);(R_x,R_y)$

Table IV

Number and Symmetry of the Stark Levels for C_{4v} Site Symmetry

J	A_1	A_2	B_1	B_2	E
0	1	0	0	0	0
1	0	1	0	0	1
2	1	0	1	1	1
3	0	1	1	1	2
4	2	1	1	1	2
5	1	2	1	1	3
6	2	1	2	2	3
7	1	2	2	2	4
8	2	3	2	2	4

Table V

Selection Rules for Electric Dipole Transitions*

	A_1	A_2	B_1	B_2	E
A_1	∥				⊥
A_2		∥			⊥
B_1			∥		⊥
B_2				∥	⊥
E	⊥	⊥	⊥	⊥	∥

* ∥ means polarization parallel to the z axis and ⊥ signifies a polarization in the x,y plane with reference to the electric vector.

Table VI

Selection Rules for Magnetic Dipole Transitions*

	A_1	A_2	B_1	B_2	E
A_1		∥			⊥
A_2	∥				⊥
B_1				∥	⊥
B_2			∥		⊥
E	⊥	⊥	⊥	⊥	⊥

* ∥ means polarization parallel to the z axis and ⊥ signifies a polarization in the x,y plane with reference to the magnetic vector. If the reference is the electric vector, the symbols ⊥ and ∥ must be interchanged.

identify the bands was iterative. A program developed by Carnall [5-7] to calculate the energy levels of rare earth ions with crystal field splitting was used (see description in next section). Entering the experimental energy values for the identified peaks, and using approximate parameters, allowed the preliminary calculation of the unassigned energy levels. Knowing the approximate position of the peaks and the expected polarization allowed the assignment of more energy levels. The process was repeated, and an increased number of parameters were freed during each successive fit. This iterative procedure permitted the assignment of thirty three experimental energy levels that were correlated with the calculated energy levels to a standard deviation of 10 cm^{-1}. A tabulation of the final parameters is given in Table IV. The practical impossibility at the present time of obtaining the needed absorption spectra impeded the unambiguous characterization of the superimposed upper manifolds. At room temperature, besides the ground state $^7F_0$, the $^7F_{1,2}$ levels are appreciably populated. Because of this fact, absorption occurs not only between ground state and the upper levels but also between the thermally populated lower excited states and the upper levels. These aditional peaks increase significantly the complexity of an already crowded spectrum and in many cases precluded a clear assignment. The experimental and calculated energy levels at 77 K are listed in Table VII.

Table VII

Experimental and Calculated Electronic Energy Levels for Single-Crystal Europium Oxychloride (77 K)

		Calc.	Exp.
$^7F_5$			
	A_2	4184	4193
	E	4125	4117
	B"	4087	
	A_1	4023	4002
	A_2	3956	3941
	B'	3877	
	E	3873	3865
	E	3757	3753
$^7F_4$			
	B"	3068	
	B'	3035	3031
	E	2970	2966
	A_1	2944	2946
	E	2851	2852
	A_2	2847	2850
	A_1	2662	2652
$^7F_3$			
	B"	2005	
	B'	1993	1990
	E	1949	1948
	E	1877	1877
	A_2	1863	1863
$^7F_2$			
	B'	1293	1281
	A_1	1092	1091
	B"	983	975
	E	975	974
$^7F_1$			
	E	461	450
	A_2	232	223
$^7F_0$			
Ref.	A_1	0	0

Table VII (Continuation)

$^5L_6$			
	A	25467	
	E	25463	
	E	25361	
	A	25359	
	B	25347	
	B	25161	
	B	25160	
	A	25106	
	E	25087	
	B	25065	
$^5D_3$			
	A_2	24362	24352
	E	24336	24326
	B	24330	
	B	24329	
	E	24281	24281
$^5D_2$			
	B"	21487	21484
	E	21459	21463
	B'	21436	
	A_1	21434	21431
$^5D_0$			
		17226	17225
$^7F_6$			
	B	5306	
	E	5305	5276
	A	5304	
	B	5173	5197
	E	5141	
	A	5050	
	A	5012	
	E	4839	
	B	4812	4815
	B	4811	

Table VII (Continuation)

$^5G_4$		
	E	26737
	B	26668
	A	26665
	A	26661
	B	26658
	A	26571
	E	26475
$^5G_3$		
	E	26581
	E	26555
	A	26490
	B	26418
	B	26361
$^5L_7$		
	B	26350
	B	26440
	E	26427
	A	26406
	A	26401
	B	26391
	E	26374
	B	26235
	E	26206
	A	26131
	E	26115
$^5G_2$		
	A	26257
	E	26212
	B	26068
	B	26045

Table VII (Continuation)

$^5L_8$		
	B	27419
	E	27409
	B	27391
	E	27376
	A	27367
	B	27305
	E	27300
	A	27292
	A	27193
	A	27190
	B	27195
	E	27149
	A	27129
$^5G_6$		
	B	26909
	A	26836
	B	26822
	E	26816
	A	26794
	E	26649
	B	26633
	B	26615
	E	26612
	A	26608
$^5G_5$		
	E	26896
	E	26877
	B	26853
	B	26850

Table VII (Continuation)

$^5L_{10}$		
	A	28747
	E	28744
	B	28743
	A	28692
	A	28672
	E	28663
	B	28647
	E	28640
	B	28532
	E	28526
	A	28523
	B	28338
	B	28333
	B	28328
	E	28326
	A	28319
$^5L_9$		
	E	28171
	B	28171
	A	28168
	B	28146
	E	28140
	A	28129
	A	28105
	A	28037
	E	28036
	B	28032
	E	27893
	B	27861
	E	27852
	A	27844
$^5D_4$		
	A	27657
	E	27626
	B	27589
	B	27582
	E	27581
	A	27493
	A	27489

C. Crystal Field Parameters

As already mentioned, the calculations of the crystal field parameters were done using the program developed by Carnall [5-7]. This program was written relying on some reasonable general assumptions. The main suppositions are that the $4f^n$ electronic states are well removed from other electronic states and that the influence of the electric field due to the solid state environment can be treated as a small perturbation of the f^n free ion configuration. The total Hamiltonian of a rare earth ion in a crystalline environment can be treated as the sum of the elemental Hamiltonians appropriate for the different interactions. In general, the contribution of free-ion interactions to the total Hamiltonian can be written as [60]

$$H = H_0 + \sum_{k=0}^{3} e_k E^k + \zeta A_{SO} + \alpha L(L+1) + \beta G(G_2) + \gamma G(R_7) + \sum_{\lambda=2,3,4,6,7,8} t_\lambda T^\lambda$$

where H_0 represents the kinetic energy of the electrons and their interaction with the nucleus. The second and third terms are due to the electrostatic and spin orbit interactions, respectively. Three additional parameters (α, β and γ) account for the two-body configuration interactions in the form given by Rajnak and Wybourne [51,61]. The last term arises from the three-body interactions, describing configuration interaction for one electron but in a nonlinear perturbation treatment. In addition, two other interactions to the free-ion Hamiltonian

are also included in our calculations. Firstly, configuration interaction effects give rise to effective values of the spin-orbit interaction parameter which are no longer constant over all configurations. The major part of this interaction can be expressed in a parametric form by the quantities P^k, k = 2, 4, 6. Secondly, relativistic corrections for spin-other-orbit and spin-spin are computed using the Marvin integrals $M^{0,2,4}$. Using a single-particle crystal field theory, the crystal field contribution is described as a sum of spherical tensors

$$H_{CF} = \sum_{k,q,i} B_q^k (C_q^k)_i$$

The number of nonzero crystal field parameters Bq^k depends on the site symmetry of the rare earth ion. For the C_{4v} site symmetry of the Eu^{III} ion in oxychlorides, the nonzero crystal field parameters are B_0^2, B_0^4, B_4^4, B_0^6, and B_4^6. The free-ion and crystal field parts of the Hamiltonian are diagonalized simultaneously to include J-mixing effects which have been shown to be significant. The total degeneracy of the $4f^6$ configuration of the Eu^{III} ion is too large to be conveniently handled by the computer. We, therefore, used a chain of diagonalization as Carnall has proposed. In the first stage, the free-ion part of the Hamiltonian was diagonalized separately by each possible J value using estimated parameters [62]. At this point we truncated the basis set by omitting all states above a certain selected energy, which was 30000 cm^{-1} for the present case. Reduced matrix elements $(SLJ||C^{(k)}||SL'J')$ were then calculated and stored for

appropriate values of the crystal field operator rank (2, 4, or 6). In the second stage, the eigenvectors derived from this diagonalization were used to transform all Hamiltonian matrices (including those of the reduced $C^{(k)}$) to this truncated base. A preliminary crystal field calculation using approximate parameters [56] correlated well with most of the experimental energy levels. Assignments were then made and a number of calculations carried out in which increasing numbers of parameters were freely varied. Several additional assignments were made based on correlations between calculated and observed energy levels and correct symmetry species. In the final calculation, five of the free-ion and all of the crystal field parameters were freely varied. The results are given in Table VIII.

D. Conclusions

The use of pure europium oxychloride single crystals for the study of the splitting of the energy levels due to the effect of the crystal field environment on Eu^{III} proved to be successful. No significant quenching due to energy transfer processes was observed. The crystal field parameters were determined and the energy levels calculated were in good agreement with the experimental values (σ = 10 cm^{-1}). A future study of the absorption spectrum at low temperature would permit the unambiguous assignment of some higher energy levels. The introduction of these additional levels would

Table VIII. EuOCl Electronic Energy Level Parameters [cm^{-1}]

F^2	83106(89)	T^8	320
F^4	60257(565)	M^0	2.1
F^6	40935(338)	M^2	1.176
α	20	M^4	0.651
β	-640	P^2	360
γ	1750	P^4	180
ζ	1319(1.8)	P^6	36
T^2	300	B_0^2	-938(20)
T^3	40	B_0^4	-698(47)
T^4	60	B_4^6	±867(28)
T^6	-300	B_0^6	1027(51)
T^7	370	B_4^6	±341(36)

Thirty three experimental energy levels were used in the calculation. The standard deviation is 10.4 cm^{-1}.
Values in parenthesis are root mean square (rms) uncertainties in the indicated parameters. Values without indicated uncertainties were not allowed to vary during the parameter fitting procedure.

allow the free variation of more parameters, and consequently, a set of parameters could be obtained which should reproduce all the energy levels in the $4f^6$ configuration to a higher degree of accuracy.

CHAPTER V

RESULTS AND DISCUSSION: LUMINESCENCE, ABSORBANCE AND RAMAN STUDIES OF EUROPIUM OXYCHLORIDE AT VARIOUS PRESSURES

A. Introduction

The use of lanthanide compounds as phosphors has produced a considerable literature concerning their optical properties. These properties are strongly influenced by the crystal structures of the respective compounds which normally change across a series of homologous lanthanide compounds, owing to the change in the lanthanide ion's size. The nature of the changes in the coordination polyhedron and crystal field parameters is normally obtained by observing a spectroscopic probe ion dispersed in spectroscopically inactive compounds. An alternative way of observing and examining structural changes is by the application of pressure. The application of pressure causes structural changes analogous to those produced by the substitution of differing lanthanide ions without the ambiguity of differing probe ion properties. Pressure studies can also be used to investigate new synthesis methods and the delocalization of f electrons.

The UV-VIS absorption spectra of lanthanide ions in solid compounds consist of weak, narrow, intra-4f level transitions at low energies and strong, broad, f→d or charge transfer

transitions at higher energies. The positions of these two spectral regions, relative to visible light, are dependent on the oxidation state of the lanthanide ion.

Normally Ln^{III} ions exhibit narrow lines in the entire visible region, while Ln^{II} ions have broad features in the blue to green and perhaps some narrow features in the far red. When a lanthanide ion is placed in a crystal field, the atomic free ion levels will split into a number of sublevels that can be characterized by the irreducible representation of the appropriate point group describing the crystal field symmetry about that ion. In this manner, the narrow, intra-4f transitions are split into groups, or manifolds, whose pattern reflects the coordination polyhedron about the lanthanide ion. Thus spectroscopic investigations of lanthanide ions under pressure can be a sensitive tool to study structural changes.

B. Results and Discussion

The equipment and methodology for the pressure studies have been described previously in Chapter II-D.4. The material used in the diamond anvil cell was single crystals of EuOCl which were prepared as written in Chapter II-A.4 by flux growth from a melt of anhydrous $EuCl_3$. The crystal structure of each sample examined in this work was verified by X-ray diffraction analysis and by Raman phonon spectroscopy.

Luminescence from the $^5D_{2,3}$ levels was obtained by

resonance enhanced two-photon excitation in the same manner mentioned in Chapter II-E.1. The crystal structure of EuOCl is the PbFCl type (D_{4h}^7-P4/nmm) with the Eu^{III} ions residing in sites with C_{4v} point symmetry (see Chapter III-A.2). The relative intensities of the lines in a given manifold will be roughly equal to the degeneracy of the irreducible representation characteristic of the respective transition. For C_{4v} site symmetry all the transitions of Eu^{III} ion are either singly or doubly degenerate. The luminescence spectrum exhibited by the Eu^{III} ion in EuOCl, under ambient to low applied pressure, corresponds very well to the spectrum expected from an Eu^{III} ion in a crystal field of C_{4v} symmetry. The predominant luminescence produced by the Eu^{III} ion results from transitions originating in the $^5D_0$ excited electronic state relaxing to the lower $^7F_{0-6}$ levels. The luminescence spectrum exhibited by Eu^{III} at ambient or low applied pressure is illustrated in Figure 25.

As stated above, Ln^{II} ions can be expected to exhibit strong, broad transitions in the visible range. In the case of Eu^{II} ion, the peak of the band in the visible region occurs at about 18000 cm^{-1}. The luminescence spectrum of a representative Eu(II) compound, $EuCl_2$, is shown in Figure 26. Also seen in Figure 2 are the luminescence spectra of EuOCl at moderate pressures, 48 and 112 kbar. It is apparent in Figure 26 that the narrow, intra-4f transitions are becoming obscured by a broad, strong emission band in the energy region for Eu^{II} ion

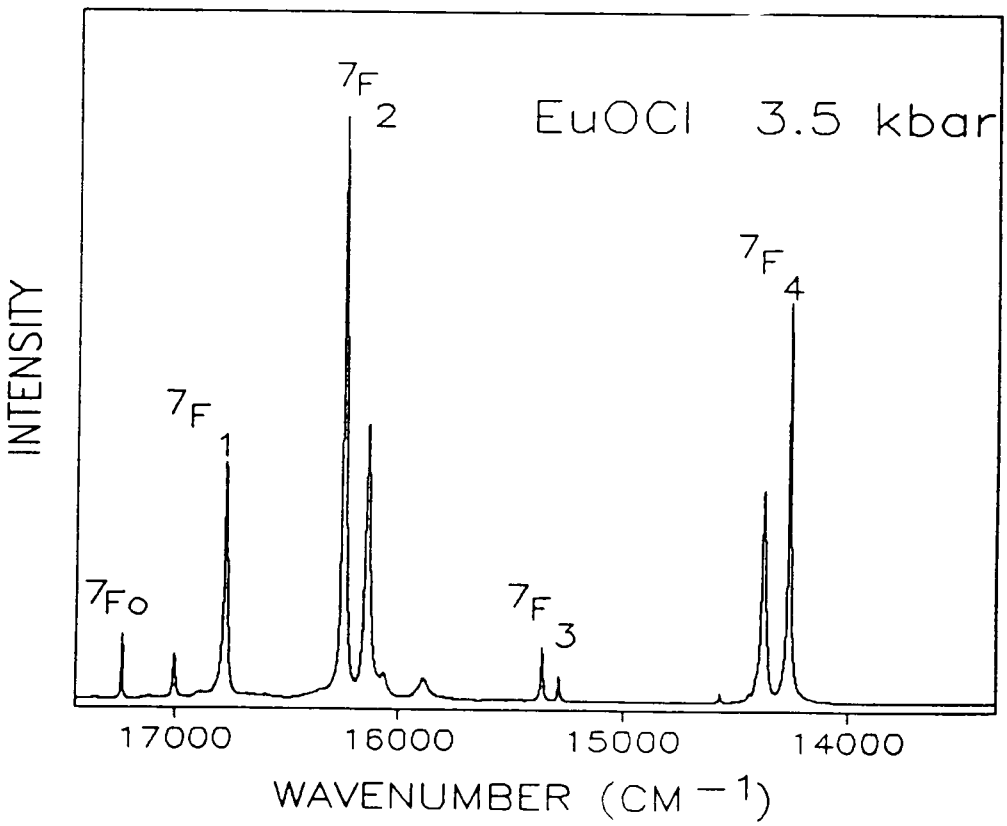

Figure 25. Luminescence Spectrum of EuOCl Showing Emission from the $^5D_0$ Level to the $^7F_{0-4}$ Levels.

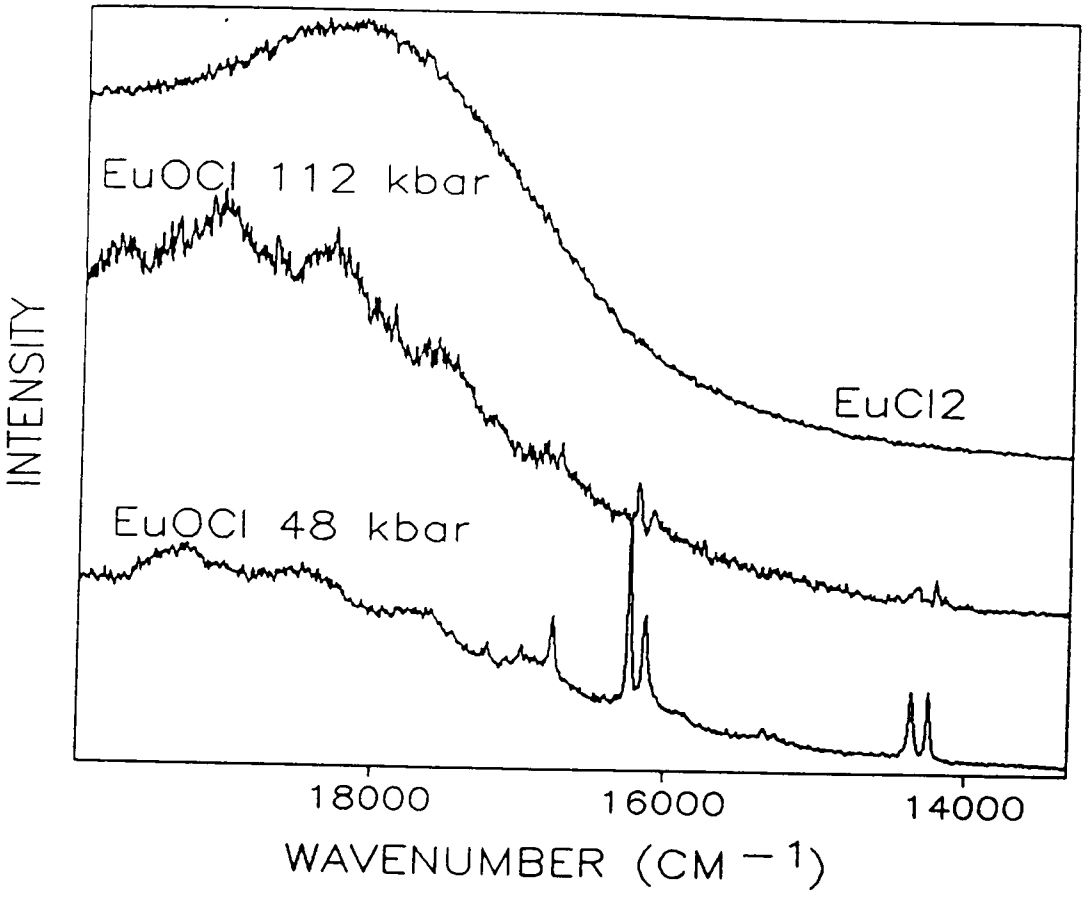

Figure 26. Luminescence Spectra of EuOCl at Elevated Pressure and $EuCl_2$ at Ambient Pressure.

emission. The f→f transitions are also red-shifted with increased pressure due to compression of the electronic cloud and conceivably increased covalency. All these occurrences are reversible and vanish when the pressure is released.

Because the dye-laser beam is not as well focused as the argon-ion laser beam, the power effectively reaching the sample through the microscope attachment is significantly diminished. For this reason the two-photon luminescence was only successful at low pressures, and even then the spectrum was quite weak.

Examination of the sample at elevated pressure, by light microscopy, revealed that the crystals had become brown and slightly opaque. The absorption spectra obtained at elevated pressures still showed the characteristic Eu^{III} peaks, although they were weakened because of the smaller light path due to gradual thinning and diminishing transparency of the sample with increased pressure. The peaks were also broadened by the effect of the raised pressure. The UV-VIS spectrum of an Eu^{II} compound as exemplified in Figure 27 presents no sharp features. Thus, the presence of Eu^{II} ions in an EuOCl sample under pressure cannot be determined precisely from an absorption spectrum obtained using our single-beam microscope spectrophotometer.

The incremental application of pressure was repeated with simultaneous measurement of luminescence lifetimes. The results of these measurements are given in Table IX. It is

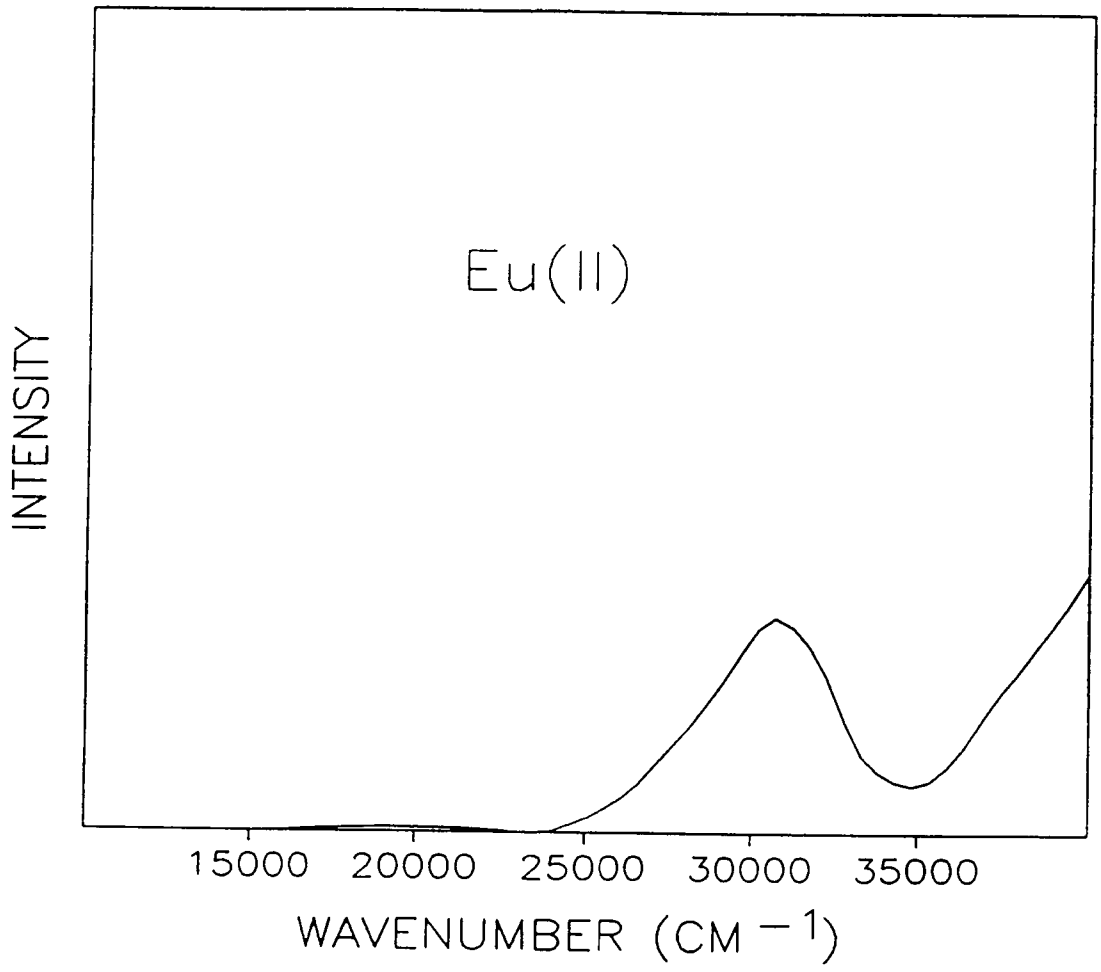

Figure 27. Characteristic Profile of the UV-VIS Absorption Spectrum of Eu^{II} Compounds.

interesting to note that the luminescence lifetimes for EuOCl are on the order of microseconds, whereas for Eu^{III} complexes with organic ligands, the reported lifetimes are in the millisecond range [63-66].

Table IX

Radiative Lifetime Versus Pressure for EuOCl

Pressure (kbar)	Lifetime $t_{1/2}$ (μs)
0	15.5
3	12.6
7	7.8
13	7.2
54	5.6

Concurrent with the rise in broadband emission, there is a decrease in the radiative lifetime. The diminishing radiative lifetime is indicative of an increasing electronic-phonon interaction of the Eu^{III} ions; that interaction was already bigger in EuOCl than in the case of the organoeuropium crystals. These events are probably caused by an increased interaction of the 4f electrons with their environment with the pressure effect generated by a closer packing.

In addition to the luminescence study an attempt was made to acquire further information from analysis of the phonon

to be useful.

Because a measurement of the magnetic moment or a Mössbauer spectrum at elevated pressure remains, as yet, unfeasible, it is uncertain whether the apparent reduction of Eu^{III} to Eu^{II} is a bulk process or only a surface phenomenon.

C. Conclusions

The appearance under pressure of the broad emission band in the expected energy region for Eu^{II} ion emission is a reversible phenomenon. This occurrence is probably generated by a reversible shifting of electron density from the anionic environment toward the europium ions due to an increased electronic interaction caused by the closer packing.

CHAPTER VI

RESULTS AND DISCUSSION: ANTI-STOKES LUMINESCENCE OF SELECTED ACTINIDE(III) COMPOUNDS

A. Introduction

As mentioned in Chapter IV, anti-Stokes luminescence from lanthanide and lanthanide-doped compounds has been studied extensively [67]. The mechanisms described for these processes involve simultaneous, two-photon absorption [68], ion-ion interactions [68], and sequential or resonance-assisted two-photon absorption [58]. The sequential or resonance-assisted route may employ one or more photon energies for excitation.

The present work is the result of a search for a technique to observe weak luminescence from a large number of different lanthanide and actinide excited states. As mentioned in Chapter IV, such luminescence is often weak due to efficient, nonradiative decay from closely spaced excited levels. However, because of the low background produced by sequential two-photon excitation, the energies (and polarizations) of many more levels can be obtained. These energy values are useful in calculating crystal field parameters and in determining lanthanide and actinide ion site symmetries. This work presents, for the first time, sequentially excited two-photon anti-Stokes luminescence for actinide compounds [69]. The anti-Stokes luminescence from

pure $^{248}CmX_3$ (X = F, Cl, Br, I) and $^{249}Cf^{III}$-doped $LuCl_3$ (≈5% Cf^{III} in $LuCl_3$) was measured and investigated.

As indicated in Chapter II, the actinide isotopes ^{248}Cm and ^{249}Cf used in this work were produced in the High Flux Isotope Reactor and were processed and purified using standard solvent extraction and/or ion exchange techniques [70]. The anhydrous compounds were prepared by using the microchemical techniques described in Chapter II. The crystal structure of each sample examined in this work was verified by a Raman crystal phonon technique [71]. The instrumentation used to acquire the Raman and luminescence spectra has been described previously in Chapter II.

B. Results and Discussion

A group theoretical analysis predicts that the various free ion electronic levels will be split into (J + 1/2) Stark components for all Kramers ions in non-cubic symmetry [3,4].

Since the ground state of the Cm^{III} ion is, in Russell-Saunders notation, an S state, it is not expected to exhibit a significant crystal field splitting (values obtained for $LaCl_3:Cm^{III}$ show components split by less than 1 cm^{-1}) [72]. Therefore the Cm^{III} ion spectra will normally consist of groups of two or more lines, the intragroup lines separated by about 100 cm^{-1} and the groups of lines separated by about 1000 cm^{-1}, beginning at about 16500 cm^{-1} and extending to higher energy.

An anti-Stokes luminescence spectrum from each of the curium trihalides $^{248}CmX_3$ (X = F, Cl, Br, I) is shown in Figures 28 to 31.

In the case of Cf^{III} ion, the ground state is $^6H_{15/2}$ and the ground-state splitting is about 300 cm^{-1}. The Cf^{III} ion luminescence spectra are composed of complex cluster of lines, with band spreads at least 300 cm^{-1} and the bands themselves separated by about 1000 cm^{-1}. The anti-Stokes luminescence spectrum from ≈5% Cf^{III} ion in $LuCl_3$ is given in Figure 32.

The mechanism for the two-photon, sequentially excited, Cm^{III} ion luminescence is illustrated in Figure 33. A large energy gap between the ground state and the first excited Stark manifold results in the excited state possessing a relatively long lifetime (≈10.0 μs). This long lifetime facilitates the absorption of a second photon, further exciting the Cm^{III} ion to a high-lying, 5f level. The existence of an excited state level of the correct energy is corroborated by the absorption spectrum presented in Figure 34. The absorption of the second photon is followed by rapid multiphonon de-excitation to lower-lying excited states which luminesce. Since excitation by two photons is very specific to the Cm^{III} ion, background from scattered radiation and matrix luminescence are virtually eliminated. Therefore, the two-photon absorption process allows observation of Cm^{III} ion luminescence from excited states which previously were seen only by absorbance measurements. In Cf^{III} ion there exist many

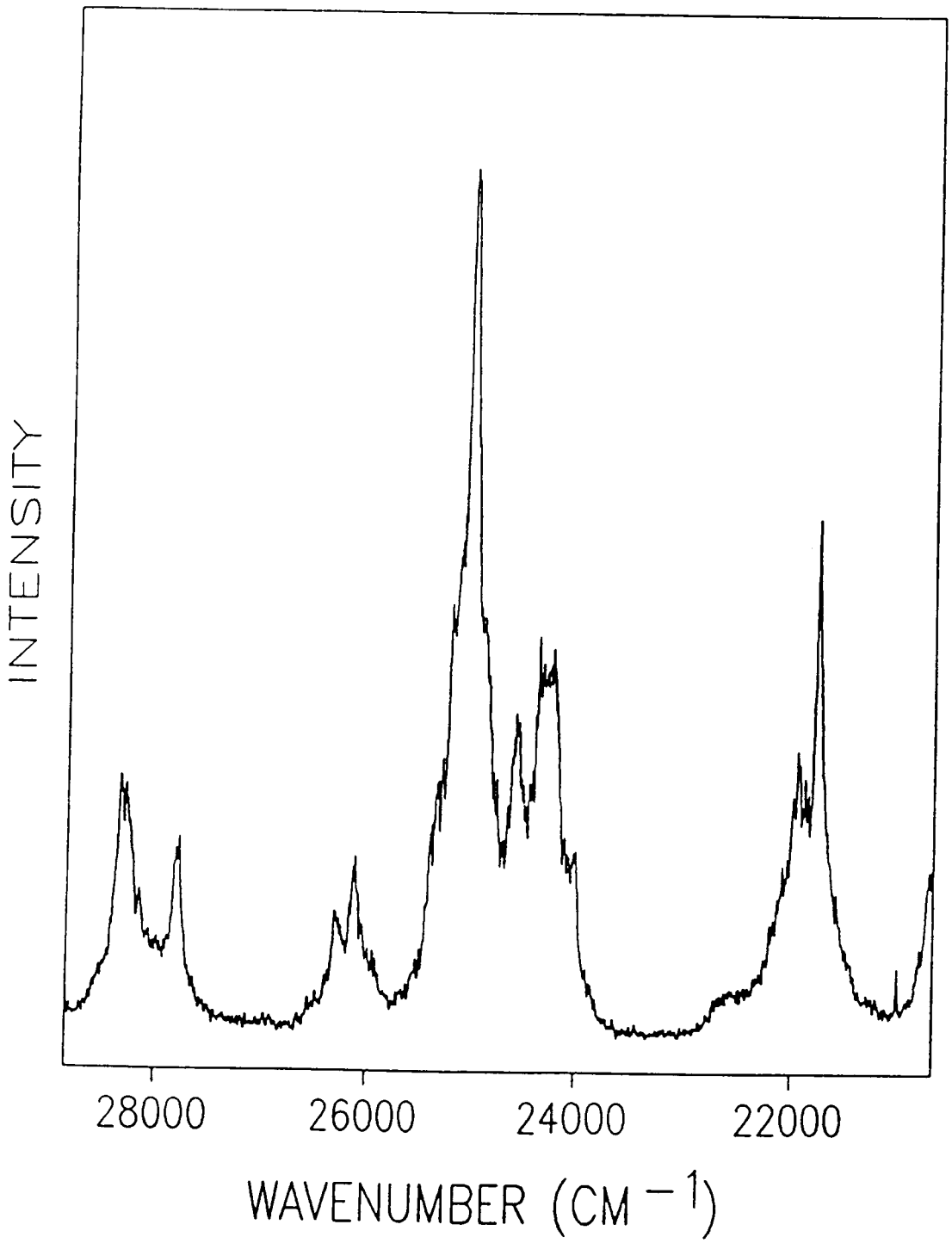

Figure 28. Anti-Stokes Luminescence Spectrum of $^{248}CmF_3$ Dye-Laser Excitation (16757 cm^{-1}).

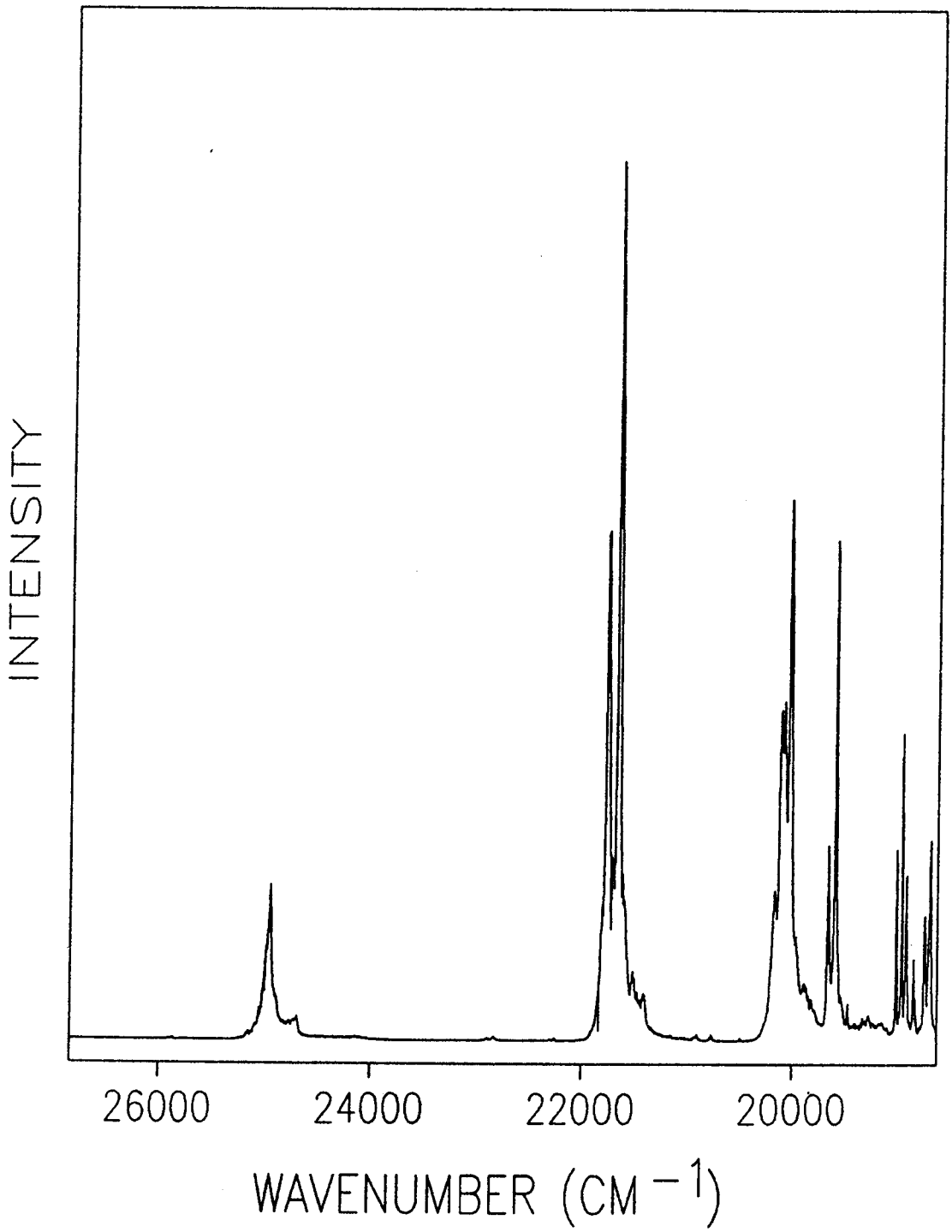

Figure 29. Anti-Stokes Luminescence Spectrum of $^{248}CmCl_3$ Dye-Laser Excitation (16341 cm^{-1}).

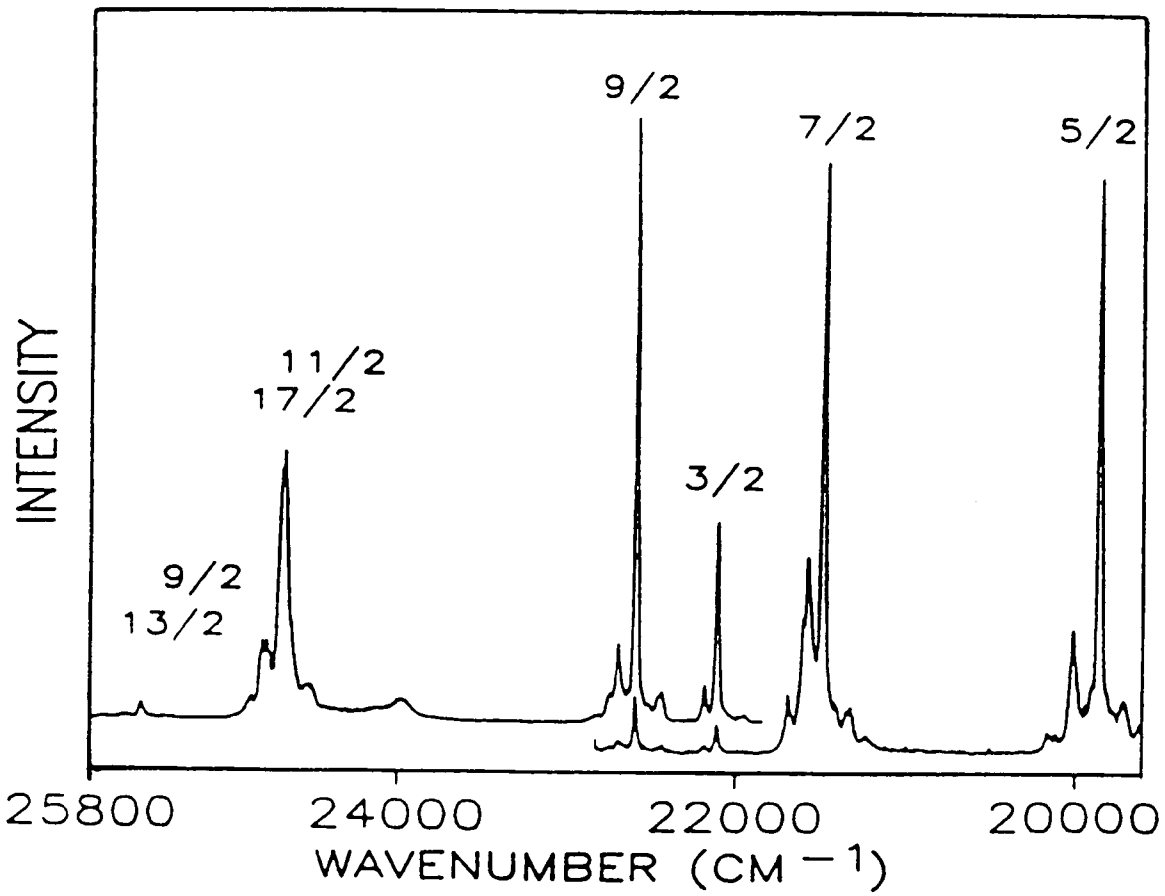

Figure 30. Anti-Stokes Luminescence Spectrum of $^{248}CmBr_3$ Dye-Laser Excitation (16605 cm^{-1}).

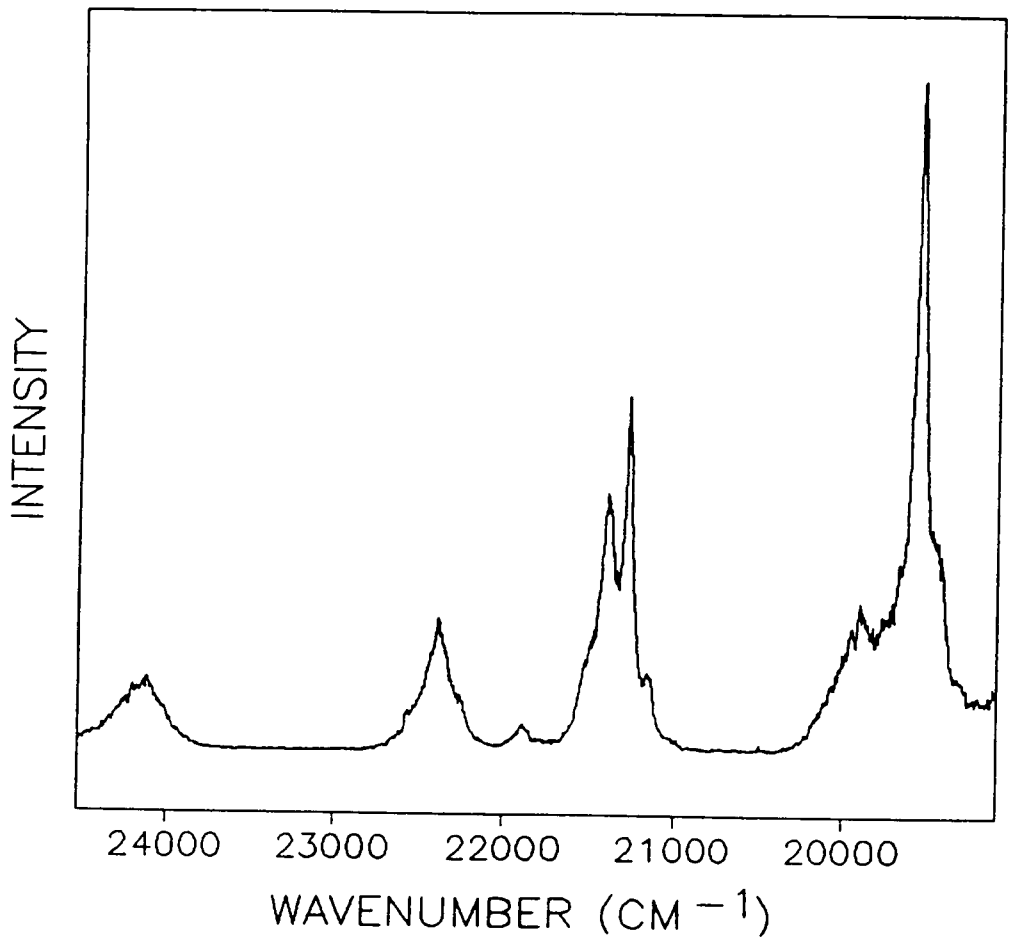

Figure 31. Anti-Stokes Luminescence Spectrum of $^{248}CmI_3$ Dye-Laser Excitation (16345 cm^{-1}).

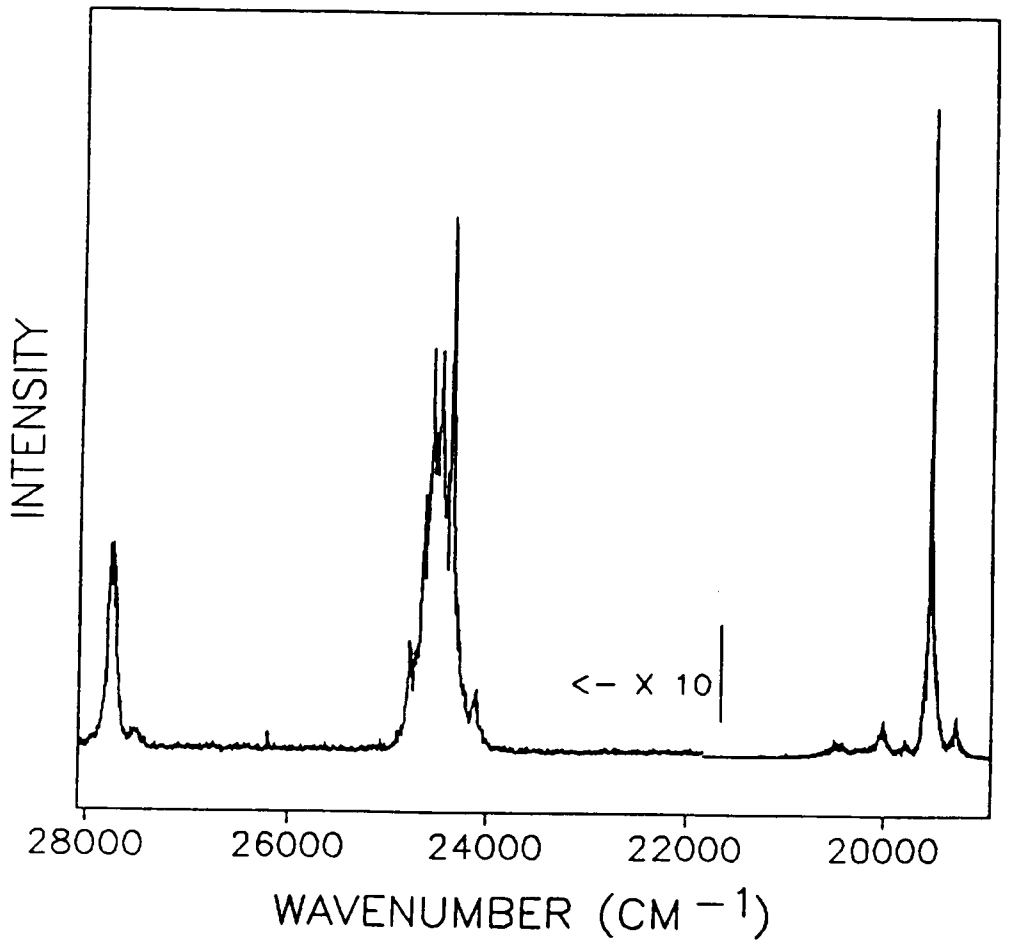

Figure 32. **Anti-Stokes Luminescence Spectrum of $LuCl_3:Cf^{III}$. Dye-Laser Excitation** (16345 cm^{-1}).

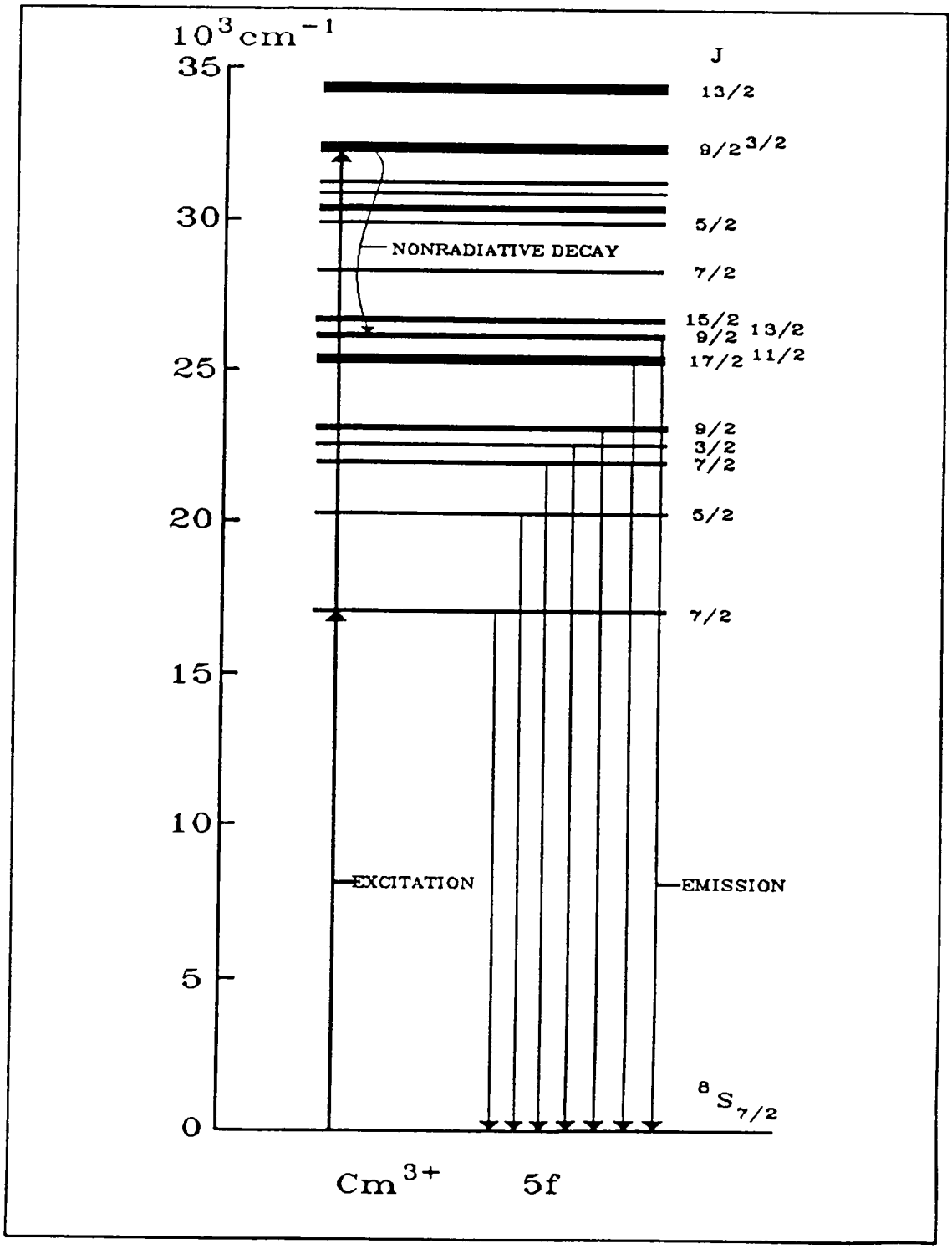

Figure 33. Schematic Diagram of the 5f Electronic Energy Levels in the Curium(III) ion.

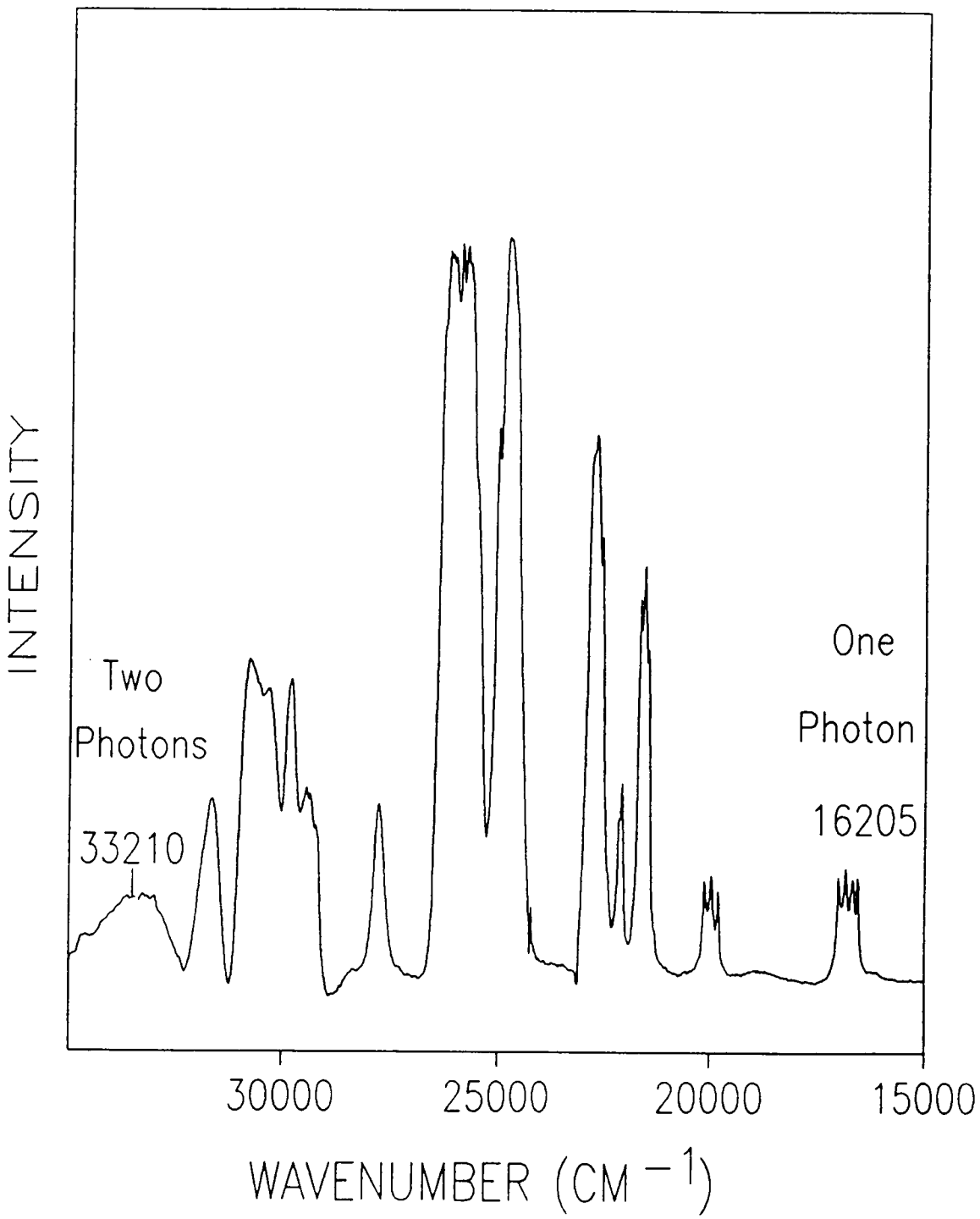

Figure 34. UV-VIS Absorption Spectrum of $^{248}CmBr_3$.

more low-lying levels than there are in Cm^{III}. Therefore, exciting Cf^{III} ion as a dopant, which reduces Cf^{III} ion-ion interactions and self-absorption, facilitates the observation of anti-Stokes luminescence in the visible range. The demonstration of anti-Stokes luminescence from Cf^{III} ion and Cm^{III} ion suggests that anti-Stokes luminescence should occur from other An^{III} ions as well.

The calculations of the crystal field parameters for the Cm^{III} trihalides following the methodology described in Chapter IV-B.2 were unsuccessful up to the present time. The attempted approach was to modify a subset of parameters obtained from the extensive set of energy levels for Cm^{III} doped in $LaCl_3$ [7] to give a better fit to the limited set of energy levels obtained from the luminescence spectra of the pure curium halides. The energy values for the pure curium halides are red shifted with respect to those of the Cm^{III} doped in $LaCl_3$ by approximately 300 cm^{-1}. This relatively big difference in the energy levels for the pure curium trihalides is not totally unexpected, because of the greater exposure of 5f electrons to the halide ions' influence. The reason for the failure of the determination of the crystal field parameters at the present time lies in the fact that the subset of the parameters is too small to give a good fit to the observed energy levels. In order to solve the problem the only possible approach is to determine a larger base of energy levels. The experimental approach to determine a larger number of electronic energy

states would involve measuring the absorption spectra of the curium trihalides at liquid nitrogen temperature.

C. Conclusions

Anti-Stokes luminescence from curium trihalides and californium-doped lutetium trichloride have been reported for the first time. The luminescence results from a sequential two-photon absorption to a high lying 5f level. The absence of scattered light and matrix luminescence achieved by the two-photon process highly reduces the background and allows observation of luminescence from excited states previously unobserved by luminescence spectroscopy. When using laser-excited luminescence, the two-photon process can permit a more thorough examination of the electronic properties of samples too small or too short-lived to be used for high resolution absorbance spectroscopy. Thus, two-photon-excited luminescence spectroscopy shows great promise for future investigations of heavy actinide compounds, as these materials are scarce and often short-lived.

CHAPTER VII

RESULTS AND DISCUSSION: EFFECTS OF PRESSURE ON THE LUMINESCENCE, RAMAN AND ABSORPTION SPECTRA OF $CmCl_3$

A. Introduction

Curium trichloride, along with all the actinide and the lighter lanthanide (Ce to Gd) trichlorides, exhibits under room temperature and pressure (RTP) conditions the hexagonal UCl_3-type structure, space group C^2_{6h}-$P6_3/m$. As mentioned in Chapter I-D.2, the metal ion in this structure is bonded to nine halogens in a tricapped trigonal prismatic geometry as displayed in Figure 35. An orthorhombic phase can be obtained in these trichlorides by applying pressure [73], or as reported for $CfCl_3$ [10], $PrBr_3$ [73], $NdBr_3$ [73] and $GdCl_3$ [74], it can be produced as a metastable phase by quenching from the melt. This orthorhombic $PuBr_3$-type layered structure is octacoordinated with a bicapped trigonal prismatic distribution and is shown in Figure 36. As indicated in that figure the contacts a and b (3.81 and 3.65 Å, respectively, for $PuBr_3$) prevent the layers from approaching close enough across c for coordination (4.03 Å for $PuBr_3$) and thus effectively limit the metal ion to eight coordination.

The UCl_3-type [Figure 35] and $PuBr_3$-type [Figure 36] structures have many similarities; the orthorhombic one can be viewed in a sense as a distortion of the hexagonal structure.

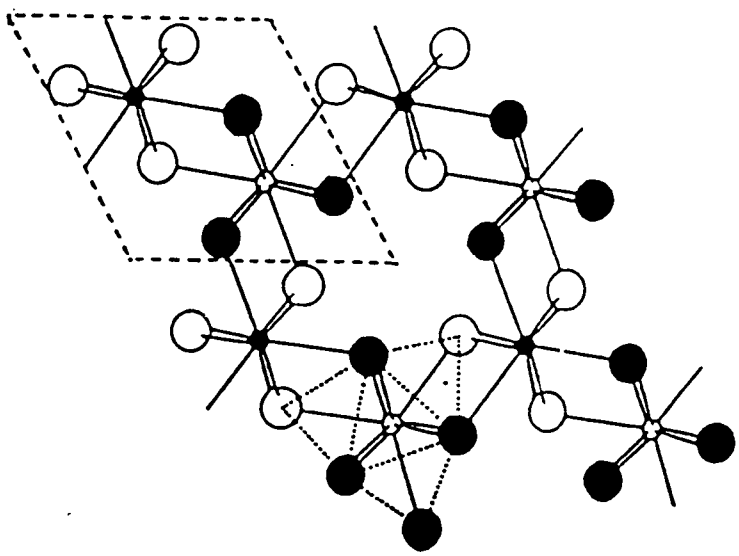

o Cm (1 / 4) ○ Cl (1 / 4)

• Cm (3 / 4) ● Cl (3 / 4)

Figure 35. The Unit Cell of the Hexagonal UCl_3-Type Crystal Structure. Depicted $CmCl_3$.

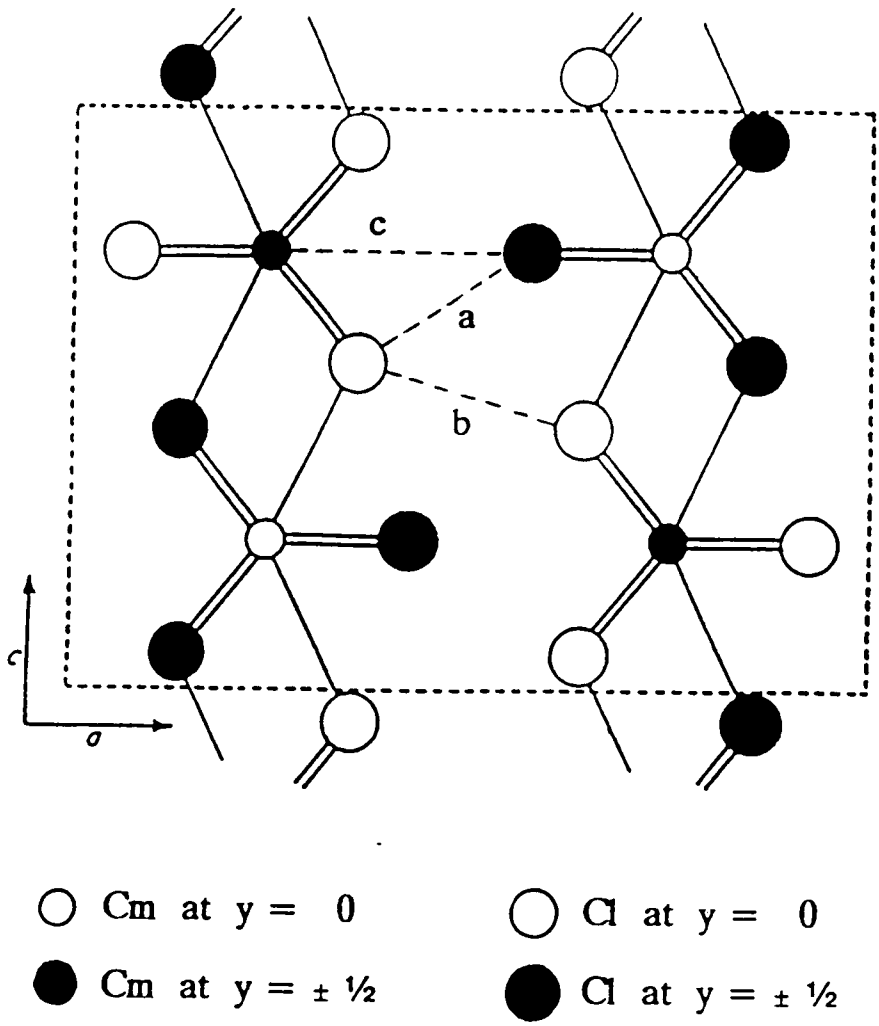

Figure 36. The Unit Cell of the Orthorhombic $PuBr_3$-Type Crystal Structure. Projected along the b Axis. Depicted $CmCl_3$. (After A. F. Wells, Structural Inorganic Chemistry, Clarendon Press, Oxford, 1962).

The mechanism of the hexagonal to orthorhombic transformation is not known; but as indicated by Burns [75], it can be visualized as resulting from the breaking of one third of the equatorial linkages with the remainder of the structure remaining intact and undergoing small atomic shifts. The site symmetry of the metal ion is somewhat similar in both structures, and for that reason the absorption and luminescence spectra from $LnCl_3$ or $AnCl_3$ samples exhibiting these structures should display some similarities.

There are two other phases for LnX_3 and AnX_3 (X= halide) where the metal ion is hexacoordinated in an almost perfect octahedral geometry. These two phases are the monoclinic $AlCl_3$-type structure and the rhombohedral BiI_3-type (same as $FeCl_3$-type) structure. Both phases can be considered as resulting from a closest-packing of the halides with the metal ions occupying one third of the octahedral sites. The halide ion packing in the monoclinic structure is ccp while that in the rhombohedral form is hcp.

For a given lanthanide or actinide trihalide, which one of the mentioned structures is adopted seems to be related to the relative sizes of the metal and halide ions. The combination of bulky cations and small halides tends to display the maximum coordination (e.g., light lanthanides and actinides with chloride). On the other hand, small cations combined with bulky halides (e.g., heavy lanthanides and actinides with iodide) adopt a closest-packed structure for

the halides with the metal ions occupying the octahedral holes. The orthorhombic structure appears in intermediate cases.

The reason for this kind of behavior can be explained primarily as a compromise between coulombic attraction between cations and anions (maximum coordination) and minimum repulsion between anions (closest-packed structure). The effect of temperature on the coordination seems to be more complex. At RTP, the light lanthanide trifluorides are nine-coordinated (LaF_3-type trigonal) while the heavy ones are octacoordinated (YF_3-type orthorhombic). It was reported [76] that the high-temperature form of the heavy lanthanide trifluorides is the nine-coordinated one. It has also been reported that the low-temperature form of $GdCl_3$ is octacoordinated ($PuBr_3$-type) while the high-temperature modification is nonacoordinated (UCl_3-type) [77]; nevertheless studies carried out in our laboratory by Daniel [74] have shown the reverse to be true. The expansion of the crystal lattice due to a higher temperature should decrease the anionic repulsion and favor a higher coordination. Concurrently, a higher temperature should increase the tendency toward disorder (i.e., a larger number of available states), thus effectively favoring lower coordination numbers.

The ultimate effect of applying pressure is also a balance of opposite trends. The incremented pressure diminishes the distance between the metal ion and the halides

increasing significantly the Coulombic attraction; this effect should promote a larger coordination number. At the same time, increased pressure augments the repulsions between halide ions by shrinking the anion-anion distances. This latter phenomenon should promote lower coordination numbers.

Examples of changes to both lower and higher coordination numbers with increased pressure have been reported. Among the reports for increased coordination number with increased pressure are: i) hexacoordinated BiI_3-type rhombohedral AmI_3 transforms under pressure to the octacoordinated $PuBr_3$-type structure [11]; ii) hexacoordinated $AlCl_3$-type monoclinic $CfBr_3$ also adopts under pressure this octacoordinated $PuBr_3$ form [12]; and iii) hexacoordinated BiI_3-type rhombohedral PuI_3 converts under pressure to this same octacoordinated $PuBr_3$ structure [13]. In addition it has been reported that nonacoordinated UCl_3-type hexagonal $PrCl_3$ and $PrBr_3$ transform under pressure firstly to the octacoordinated $PuBr_3$-type orthorhombic structure and then later to an as yet unidentified structure [73]. Similarly, it has been indicated by spectrophotometric analysis that nonacoordinated UCl_3-type hexagonal $CfCl_3$ transforms under pressure to the octacoordinated $PuBr_3$ form [10].

The conclusion about pressure effects on the coordination number seems to be that, for structures that display initially a lower coordination number, the increase of coulombic attraction causes a concomitant increase in the coordination

number, at least as a first stage. Although it has not yet been reported, according to the previous comments here at even higher pressures, the balance of increased vs. decreased coordination number should swing to favor a lower coordination number. For crystal structures that initially possess a large coordination number, the repulsive effect appears to drive the decrease in coordination number seen with increased pressure.

Wilmarth [73], in a previous study conducted in the Transuranium Research Laboratory (TRL), studied the behavior of $PrCl_3$, $PrBr_3$, and $NdBr_3$ under pressure and suggested from the analysis of the absorption and Raman spectroscopic results the existence of a potentially new, as-yet-unidentified, high pressure phase.

The luminescence studies of selected lanthanide and actinide compounds presented in Chapters IV to VI of this dissertation indicate its great potential as a tool to study structural changes. Using the knowledge gained from the study of the luminescence of curium trihalides described in Chapter VI along with data from the phonon Raman and absorption spectrophotometric analyses, a study of $CmCl_3$ under pressure was undertaken.

B. Results and Discussion

As a reference, the Raman spectrum of $CfCl_3$ in its RTP stable hexagonal form and that from the orthorhombic

modification obtained by quenching from the melt [71] are shown in Figure 37. The Raman spectra from the hexagonal and orthorhombic forms of $CmCl_3$ should be essentially equivalent to those of $CfCl_3$, with the only difference being small shifts in the positions of the peaks. Our starting hexagonal $CmCl_3$ yielded a Raman spectrum like that of hexagonal $CfCl_3$ but with the peaks at 80, 184, 196 and 224 cm^{-1}, respectively.

Raman, luminescence and absorption spectra were taken at each pressure step during the course of the experiment. The Raman phonon spectra are shown sequentially in Figures 38 to 43 and all luminescence spectra in Figures 44 to 48. In order to enhance the resolution, three absorption spectra, covering three different regions, were taken for each pressure step. The first region covers the transitions from the ground state ($^8S_{7/2}$) to the $^6I_{15/2}$, $^6I_{13/2}$, $^6D_{9/2}$, $^6I_{11/2}$ and $^6I_{17/2}$ levels, and are shown collectively for the different pressures in Figures 49 to 52. The second region covers absorption from the ground state to the $^6P_{3/2}$ and $^6I_{7/2}$ levels (Figures 53 to 56). Finally, the third region covers the transitions from the ground state to the $^6D_{7/2}$ level, and these spectra are shown in Figures 57 to 60.

The $CmCl_3$ Raman, luminescence and absorption spectra from the hexagonal, low-pressure form obtained at 2.1 kbar in the first experiment are shown in Figures 38, 44, 49, 53 and 57. As expected the spectra are consistent with the ones obtained at RTP. The pressure was raised to 64 kbar and the Raman

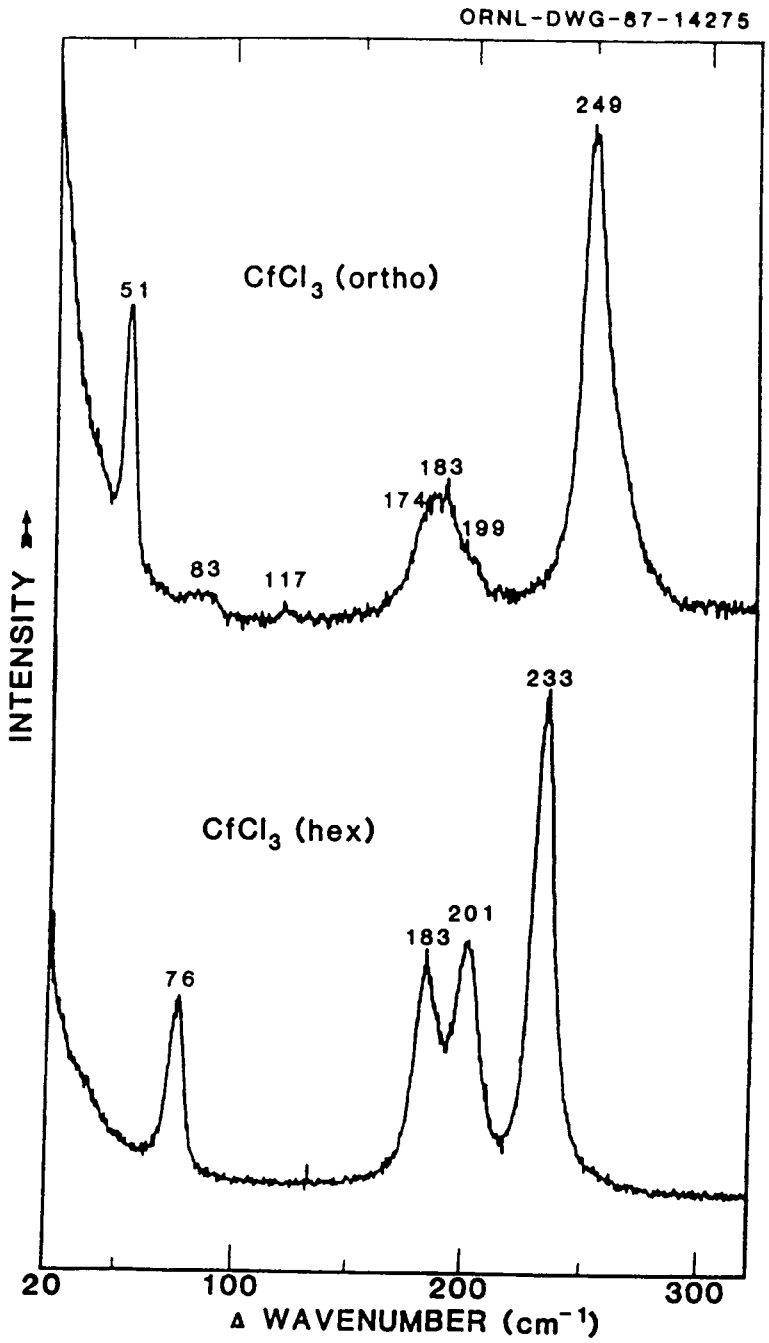

Figure 37. Raman Spectra of $CfCl_3$ in its Hexagonal and Orthorhombic Forms.

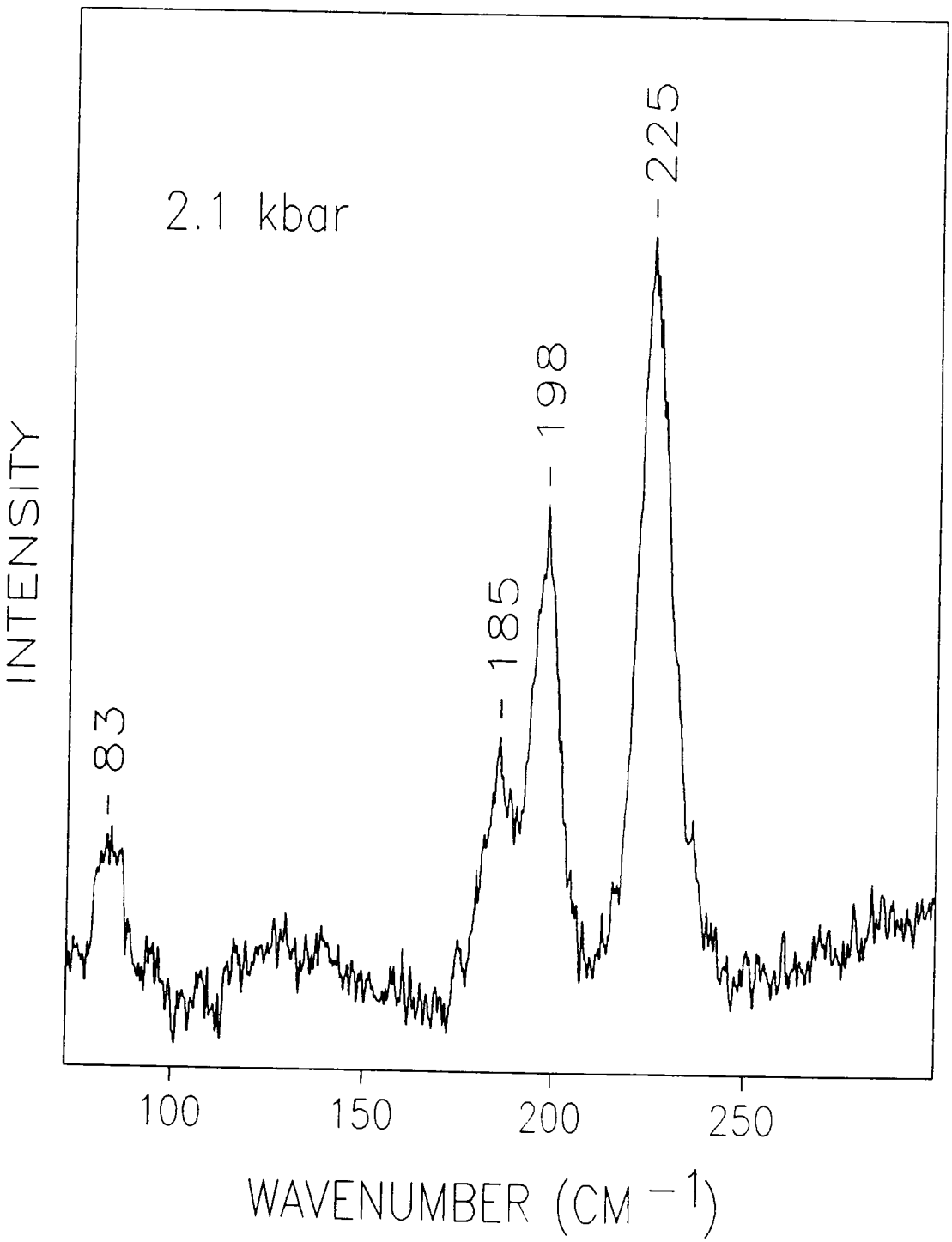

Figure 38. Raman Phonon Spectrum of $CmCl_3$ at 2.1 kbar Argon-Ion Laser 514.5 nm.

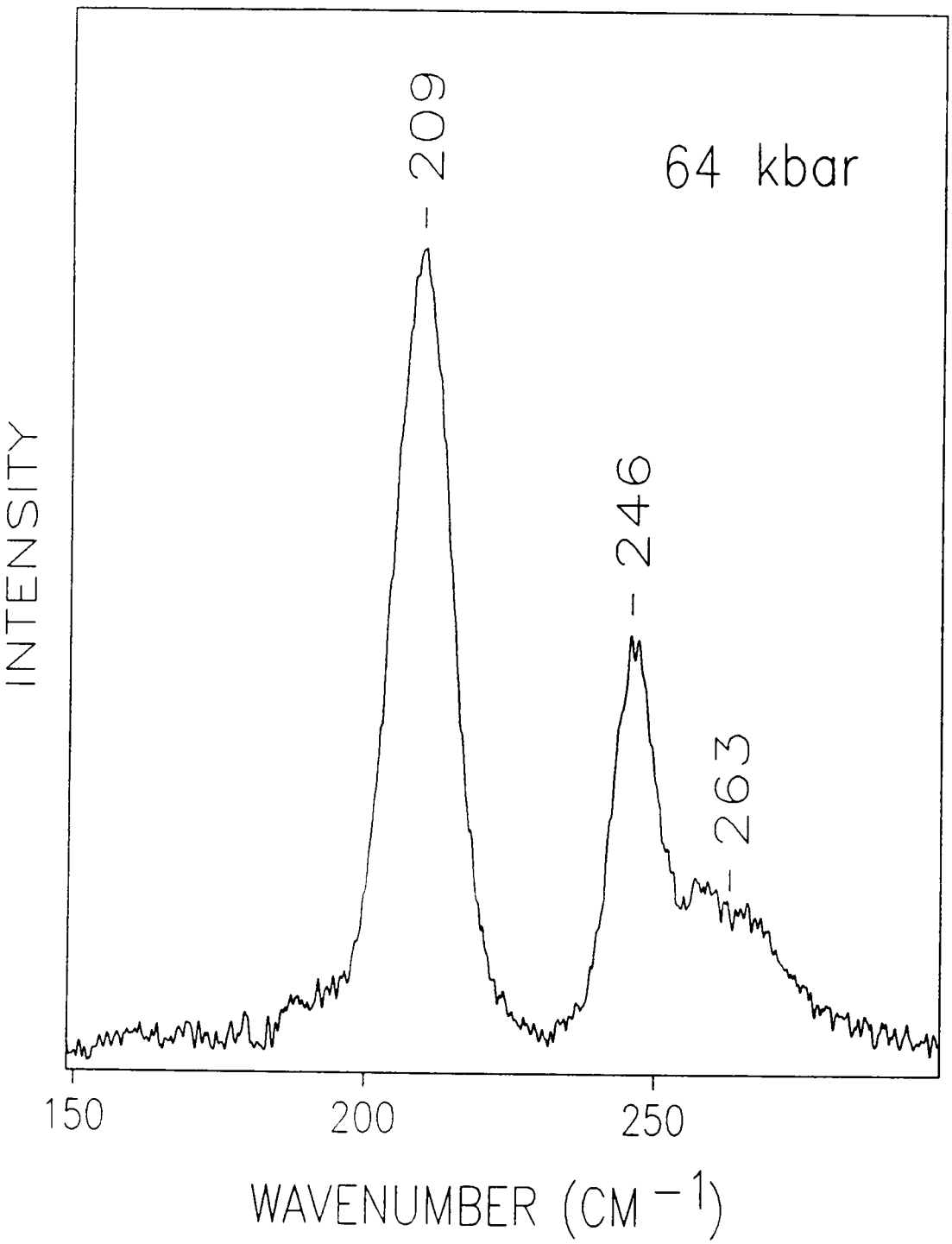

Figure 39. Raman Phonon Spectrum of $CmCl_3$ at 64 kbar Argon-Ion Laser 514.5 nm.

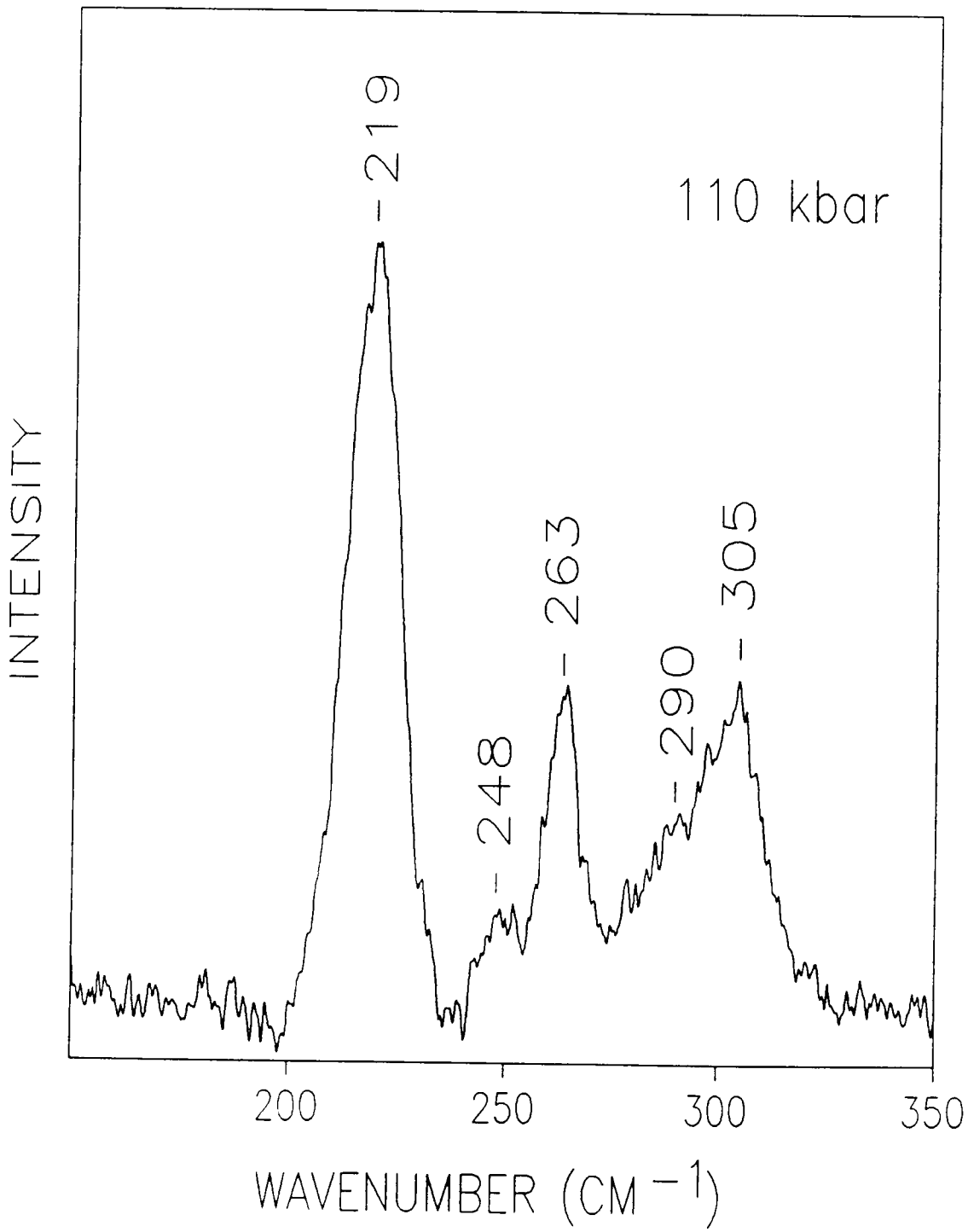

Figure 40. Raman Phonon Spectrum of $CmCl_3$ at 110 kbar Argon-Ion Laser 514.5 nm.

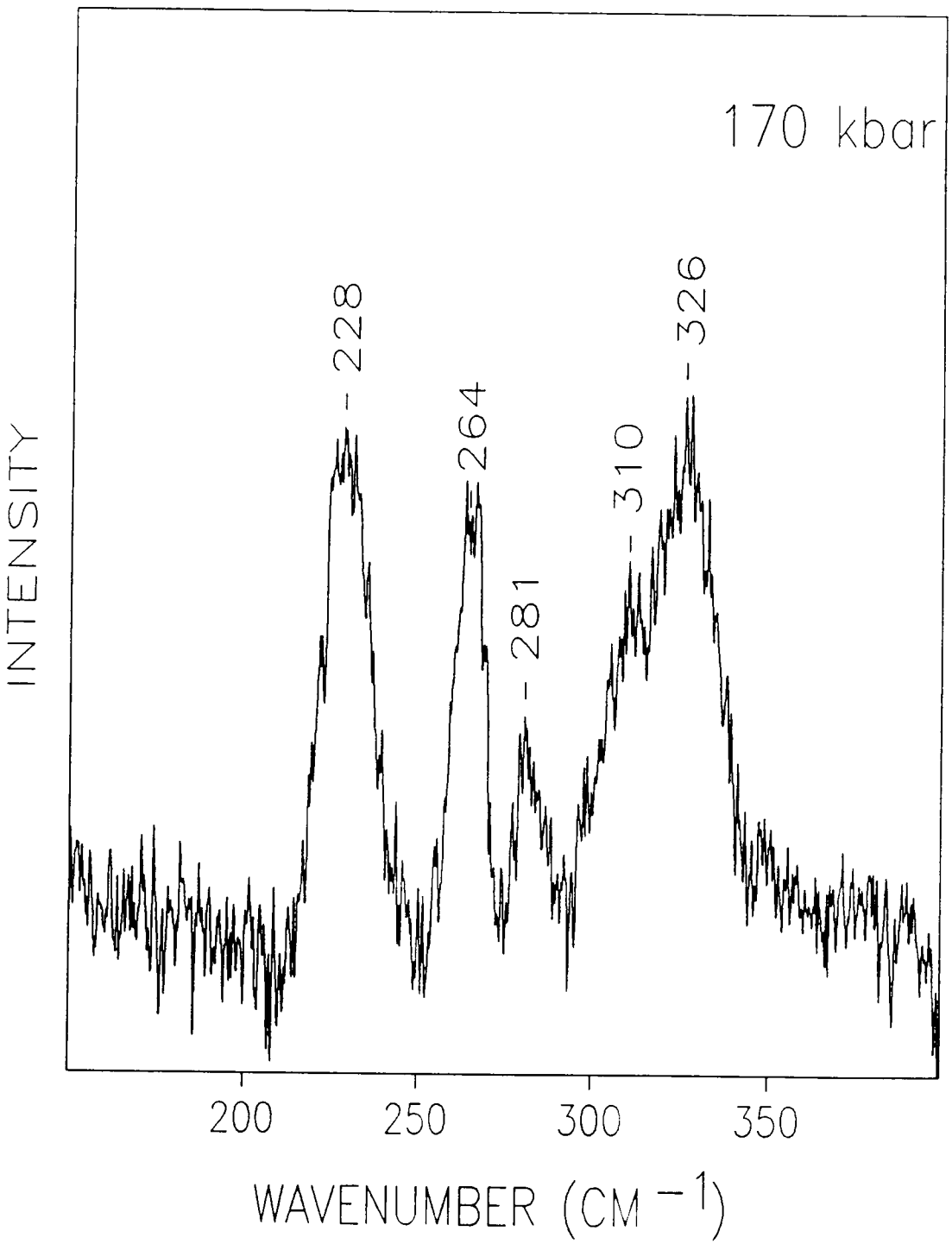

Figure 41. Raman Phonon Spectrum of $CmCl_3$ at 170 kbar Argon-Ion Laser 514.5 nm.

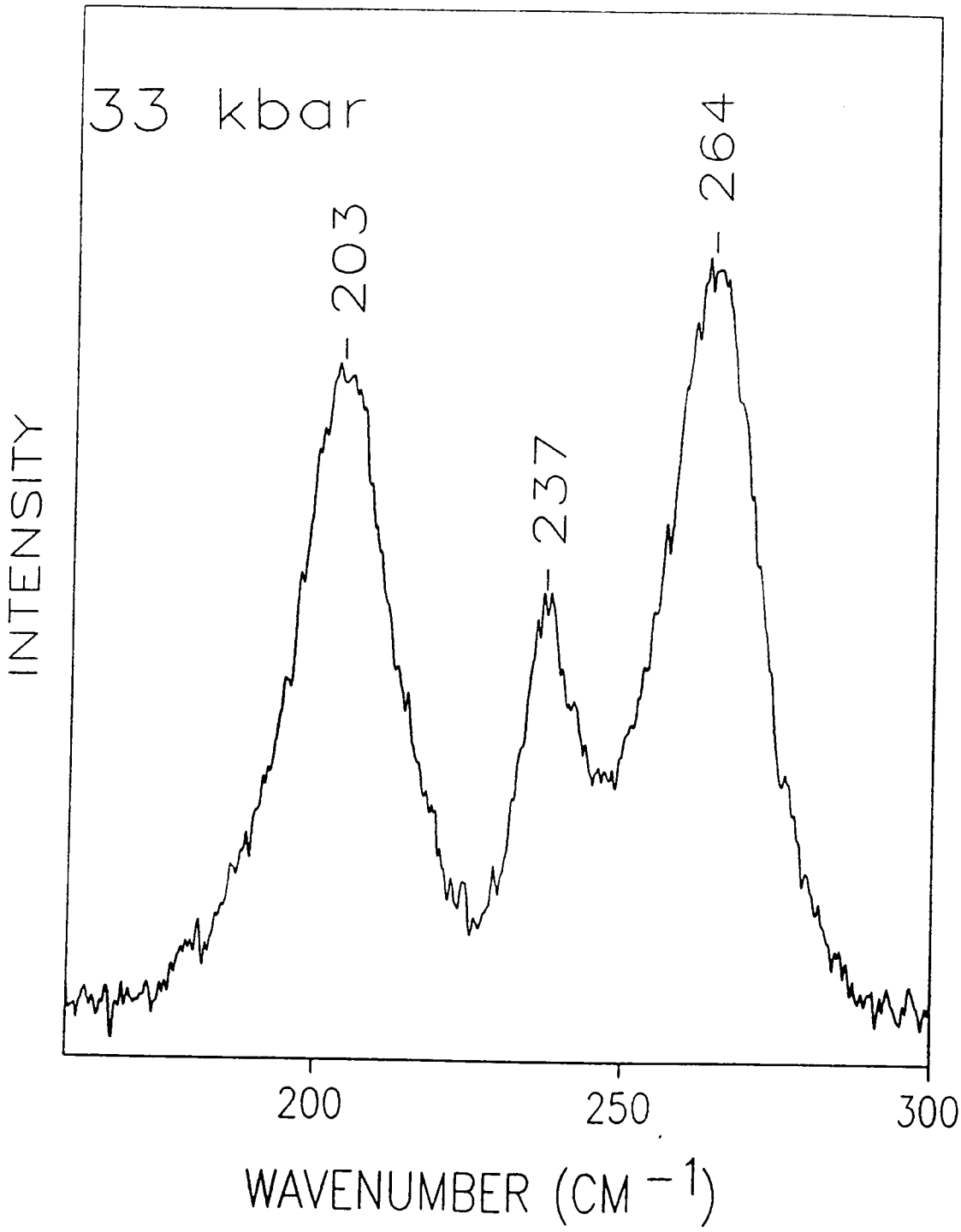

Figure 42. Raman Phonon Spectrum of $CmCl_3$ at 33 kbar Argon-Ion Laser 514.5 nm.

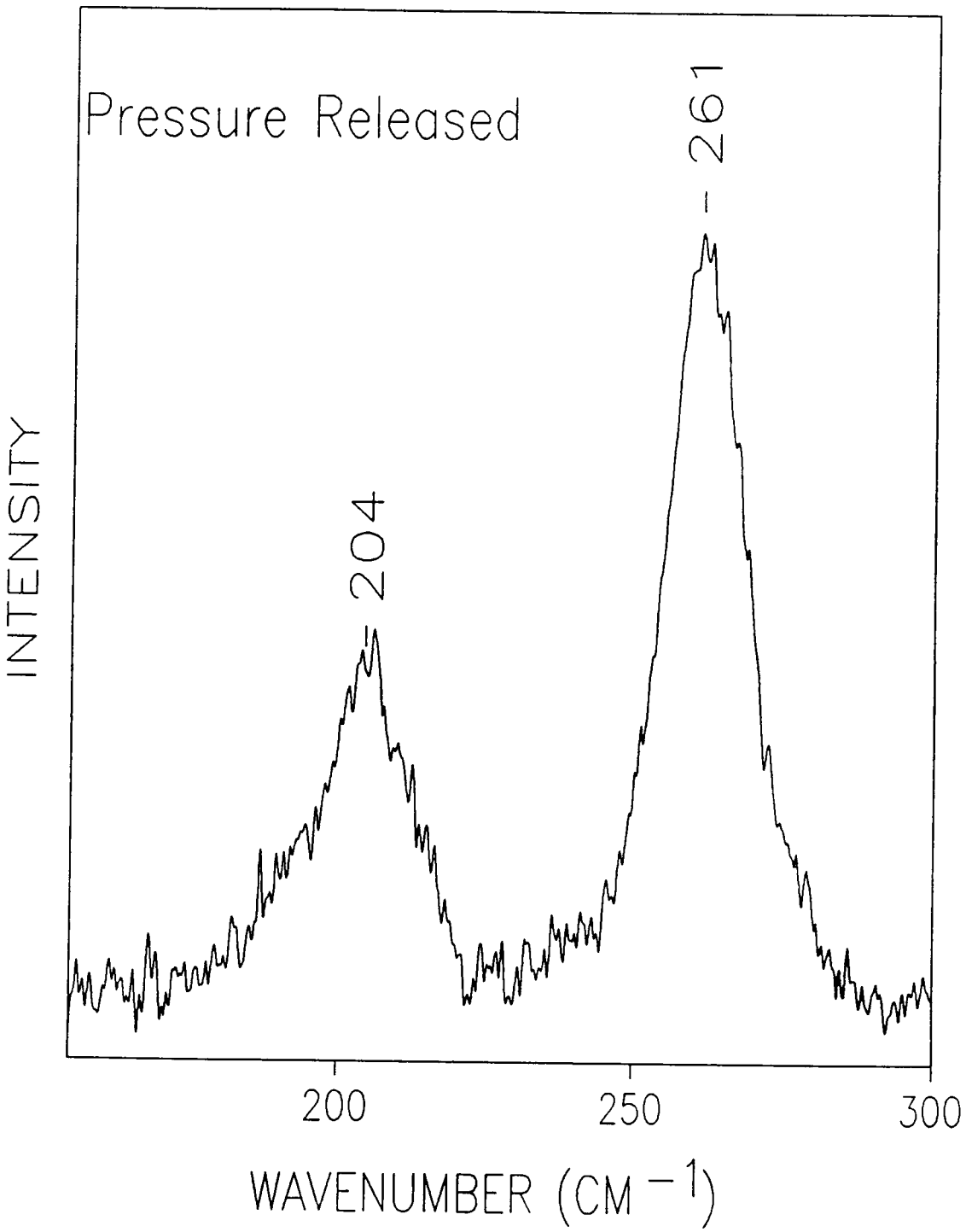

Figure 43. Raman Phonon Spectrum of $CmCl_3$ at RTP Argon-Ion Laser 514.5 nm.

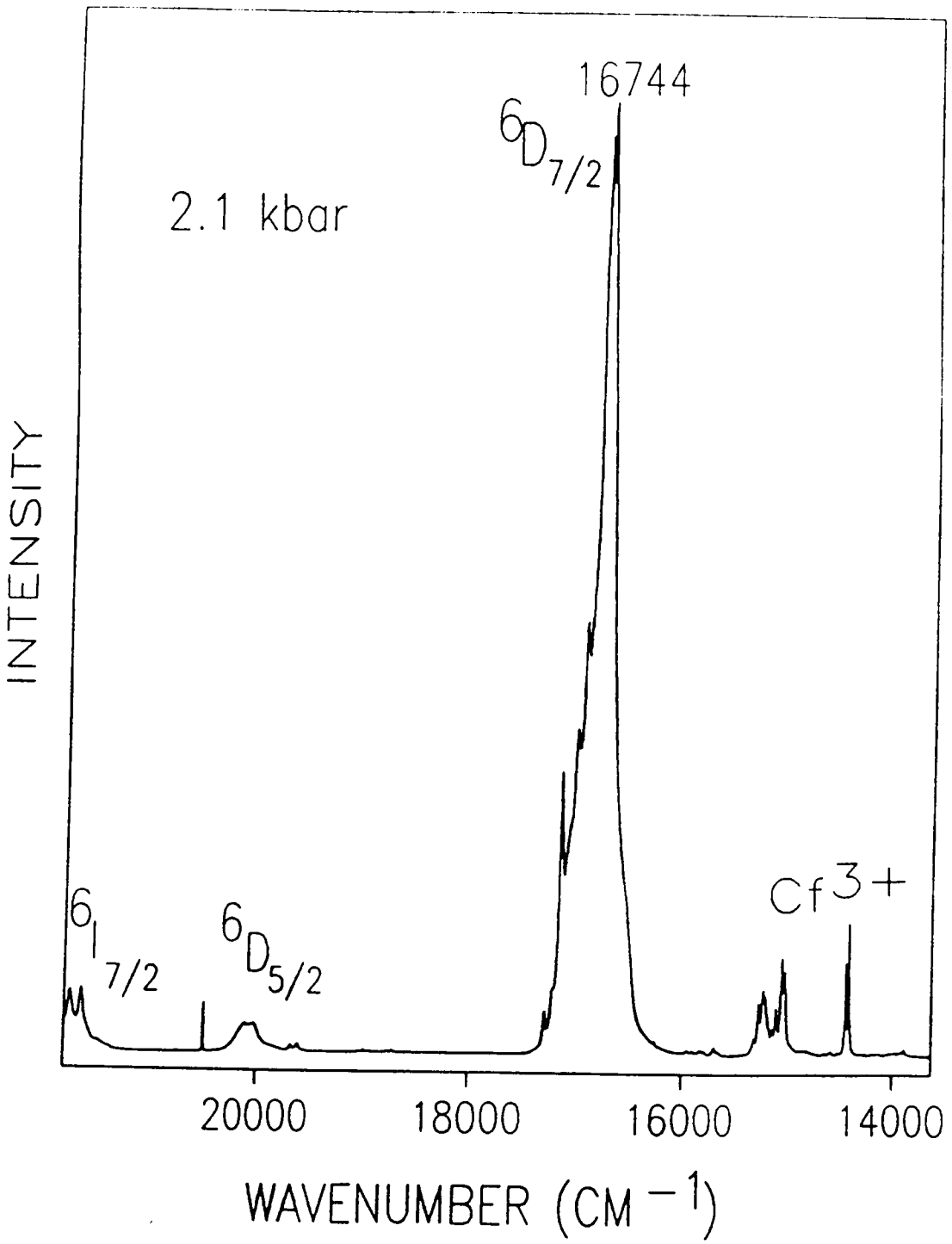

Figure 44. Luminescence Spectrum of $CmCl_3$ at 2.1 kbar Argon-Ion Laser 458 nm.

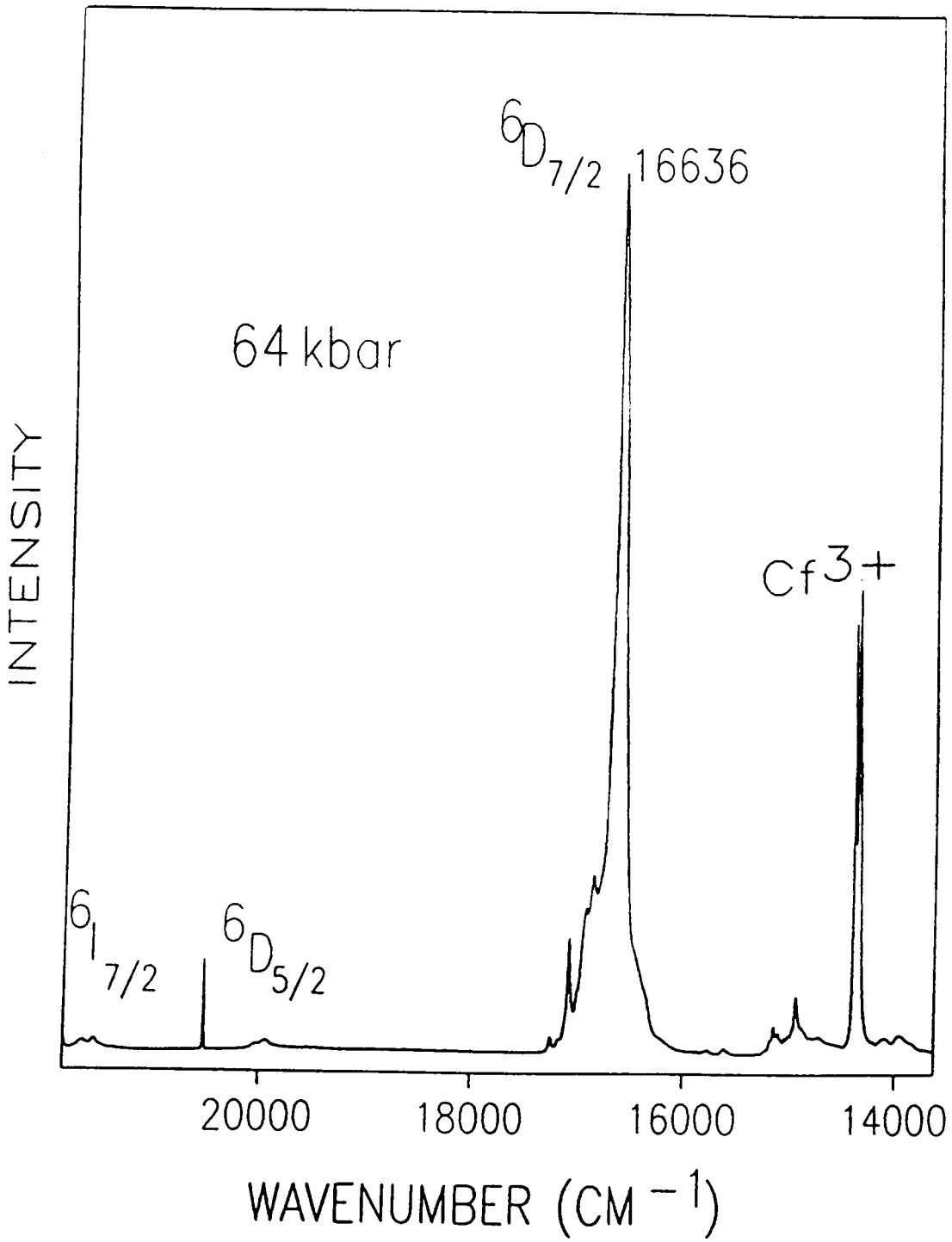

Figure 45. Luminescence Spectrum of $CmCl_3$ at 64 kbar Argon-Ion Laser 458 nm.

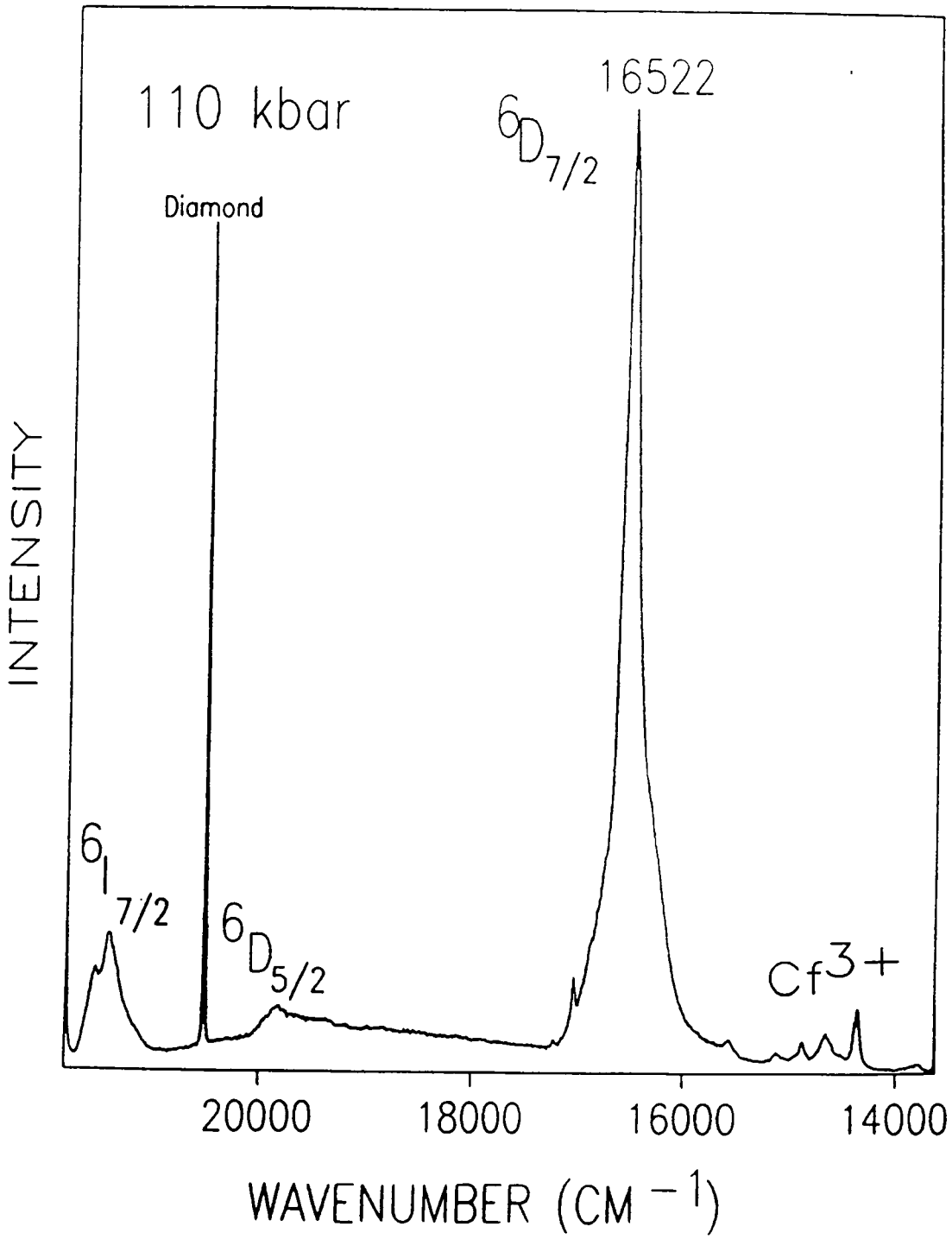

Figure 46. Luminescence Spectrum of $CmCl_3$ at 110 kbar Argon-Ion Laser 458 nm.

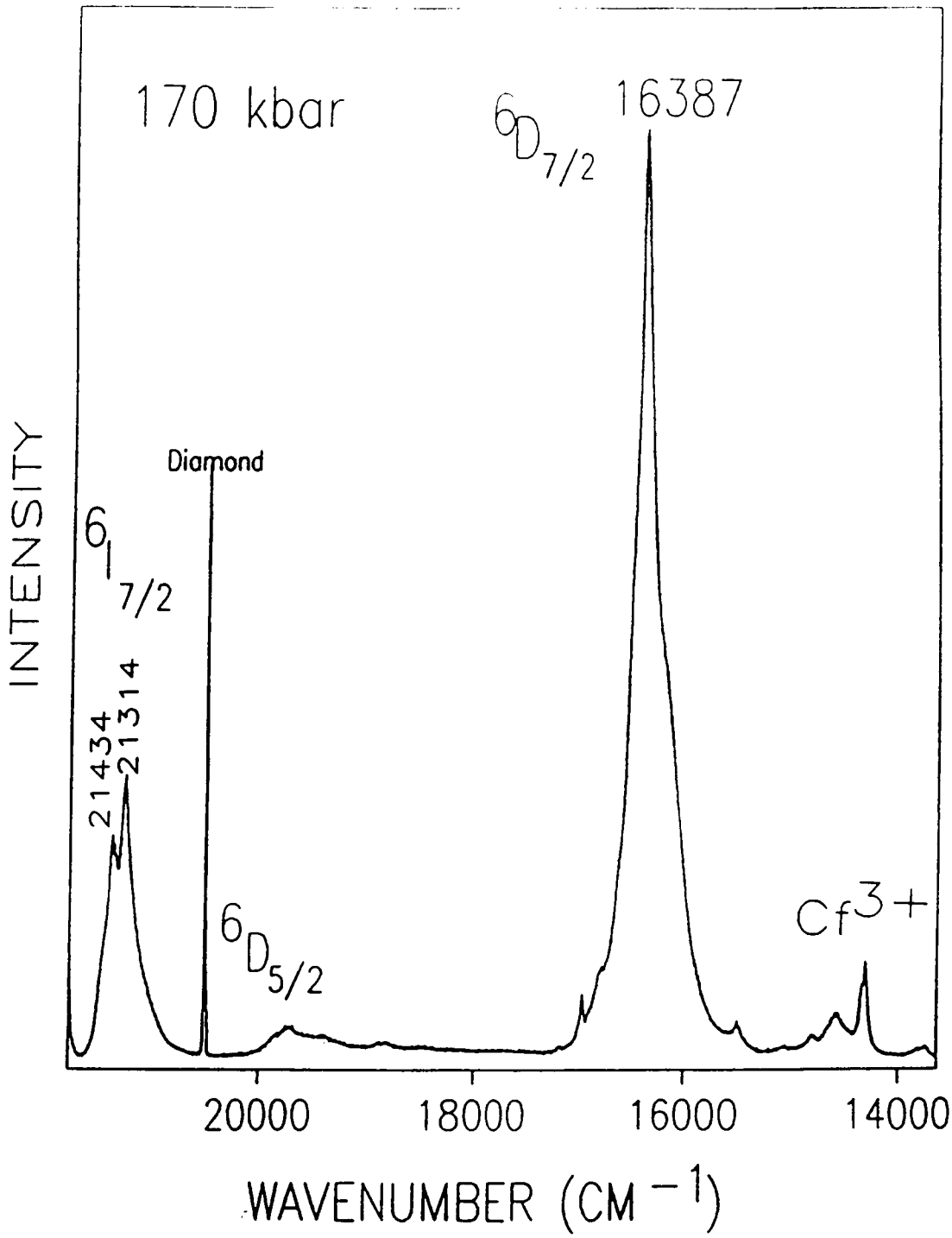

Figure 47. Luminescence Spectrum of $CmCl_3$ at 170 kbar Argon-Ion Laser 458 nm.

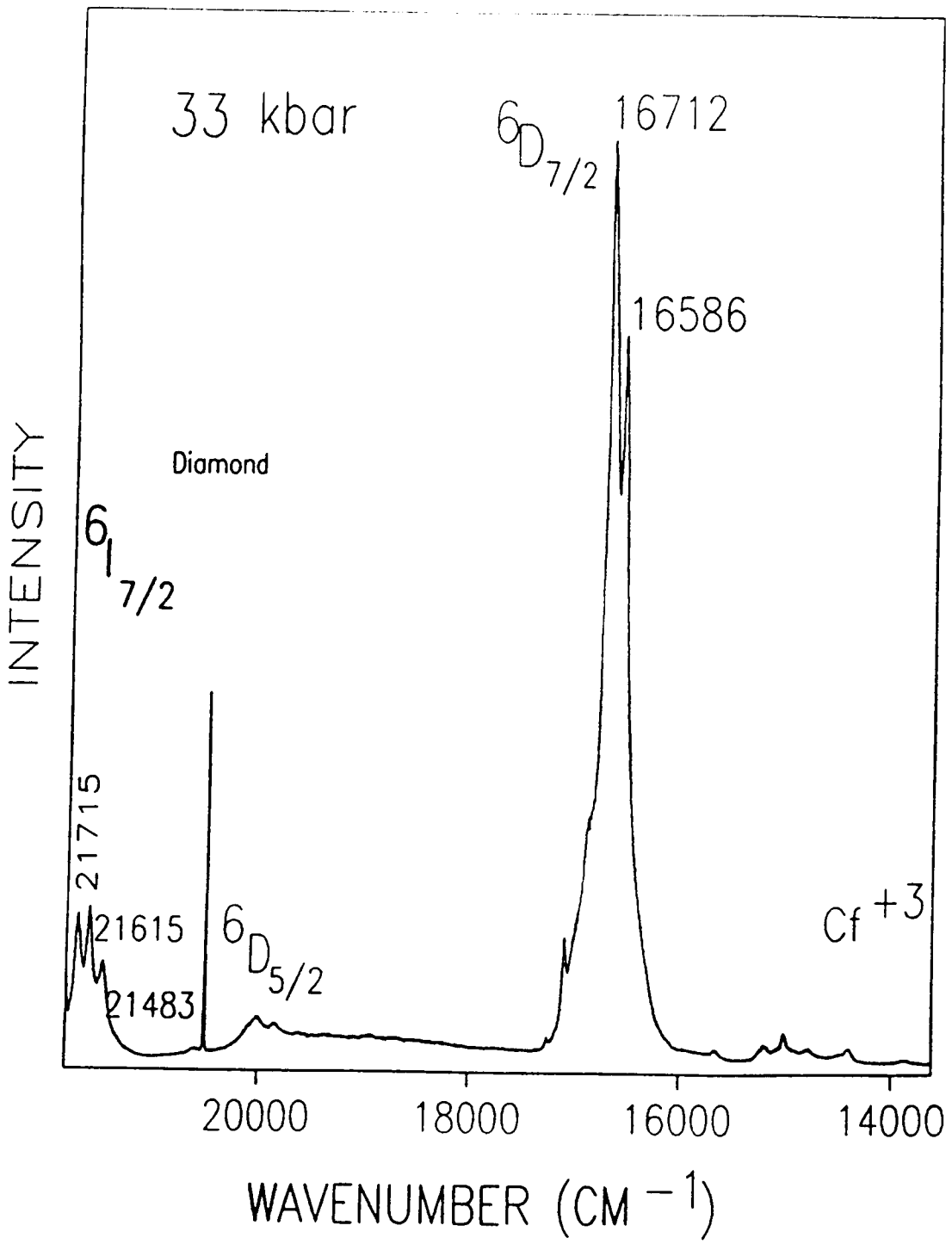

Figure 48. Luminescence Spectrum of $CmCl_3$ at 33 kbar Argon-Ion Laser 458 nm.

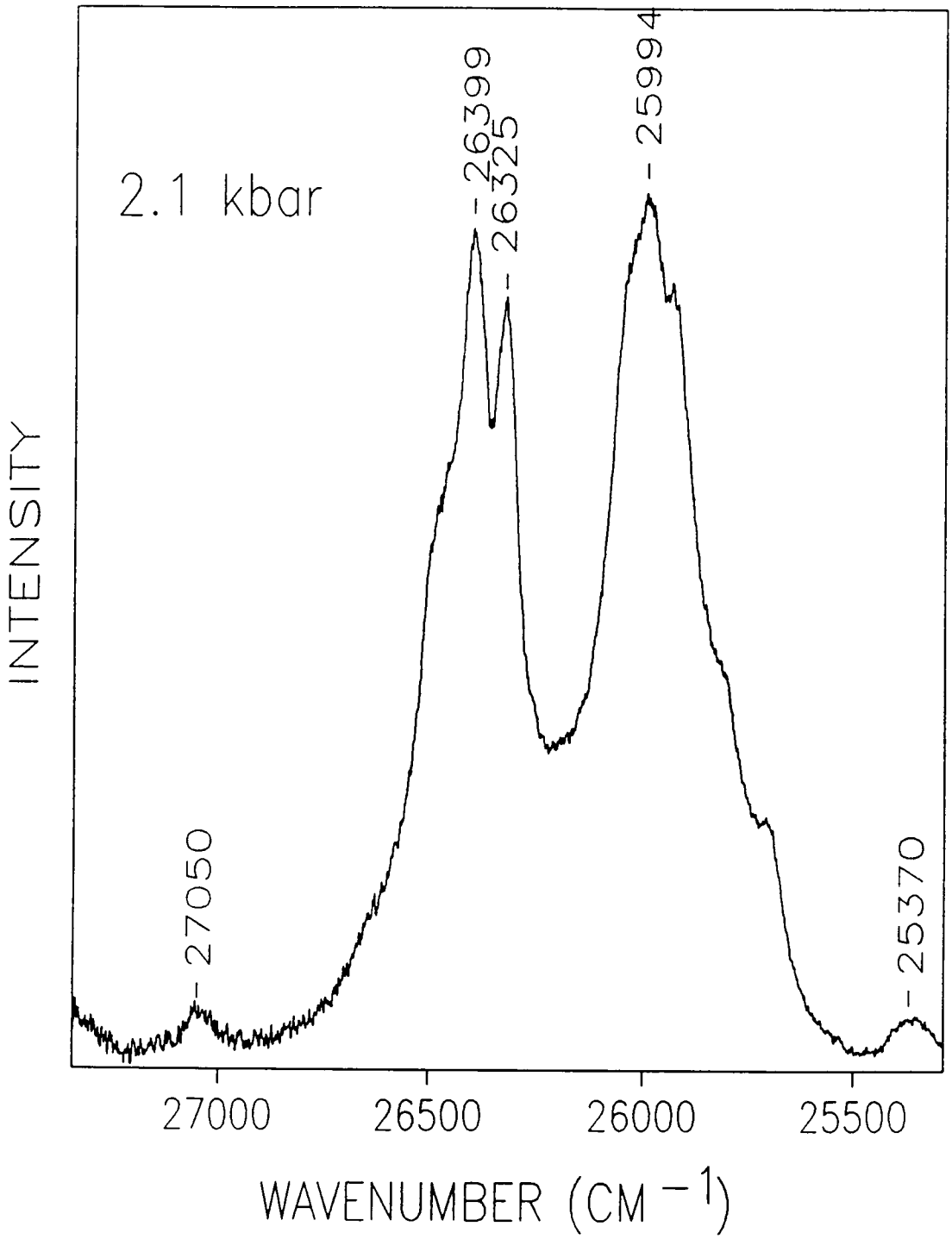

Figure 49. Absorption Spectrum of $CmCl_3$ at 2.1 kbar Showing the Region Covering the Transitions from the Ground State to $^6D_{7/2}$, $^6I_{15/2}$, $^6I_{13/2}$, $^6D_{9/2}$, $^6I_{11/2}$ and $^6I_{17/2}$.

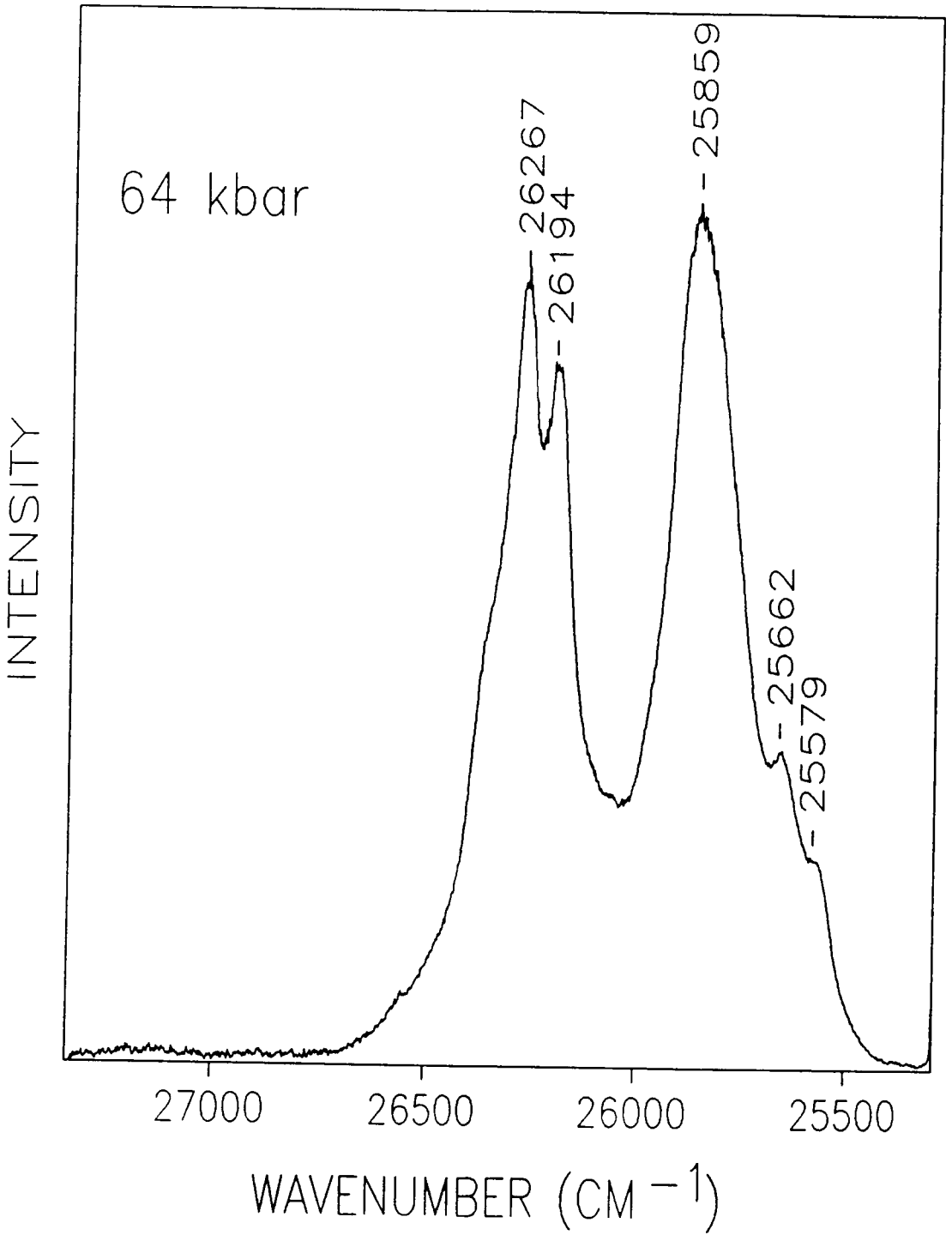

Figure 50. Absorption Spectrum of $CmCl_3$ at 64 kbar Showing the Region Covering the Transitions from the Ground State to $^6D_{7/2}$, $^6I_{15/2}$, $^6I_{13/2}$, $^6D_{9/2}$, $^6I_{11/2}$ and $^6I_{17/2}$.

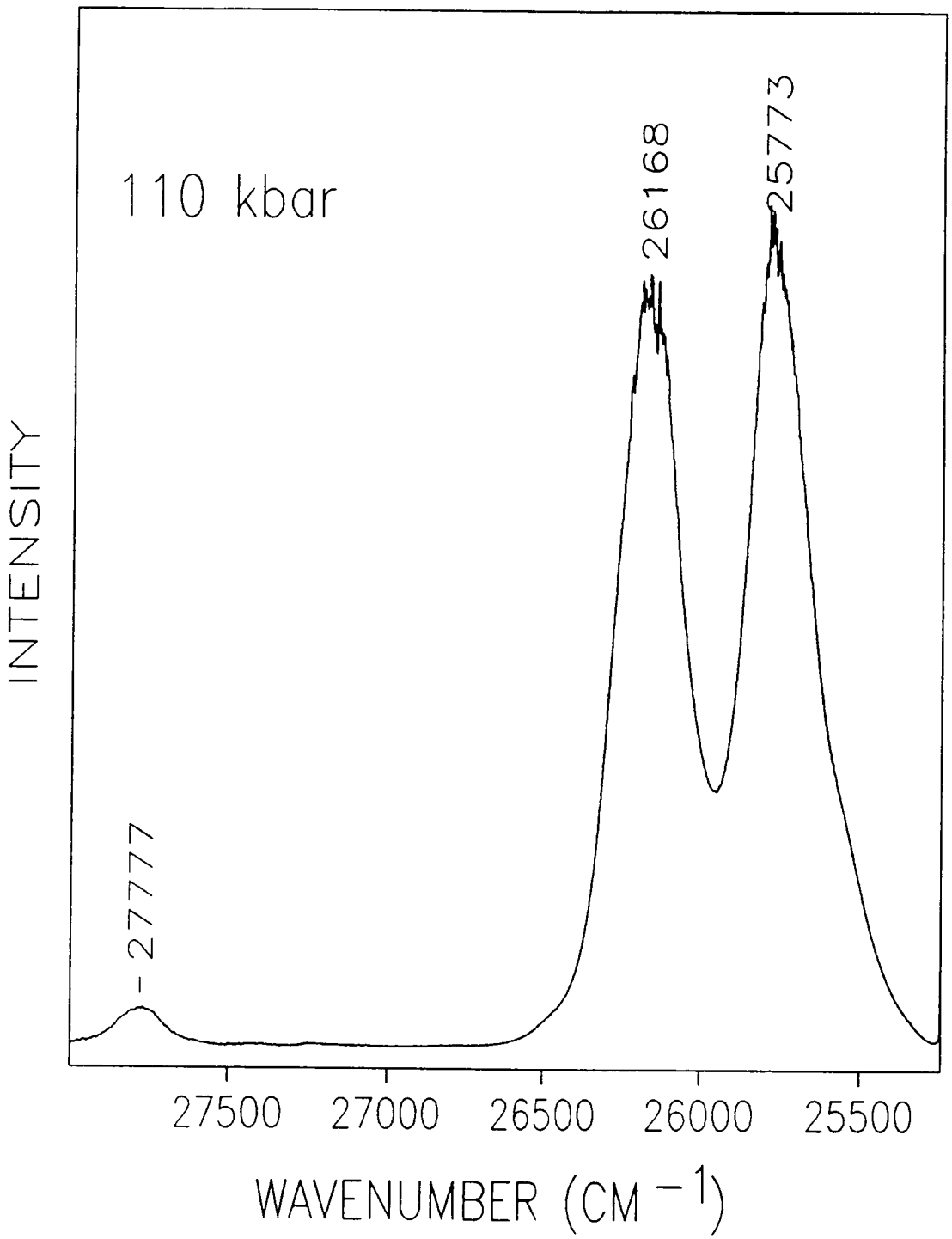

Figure 51. Absorption Spectrum of $CmCl_3$ at 110 kbar Showing the Region Covering the Transitions from the Ground State to $^6D_{7/2}$, $^6I_{15/2}$, $^6I_{13/2}$, $^6D_{9/2}$, $^6I_{11/2}$ and $^6I_{17/2}$.

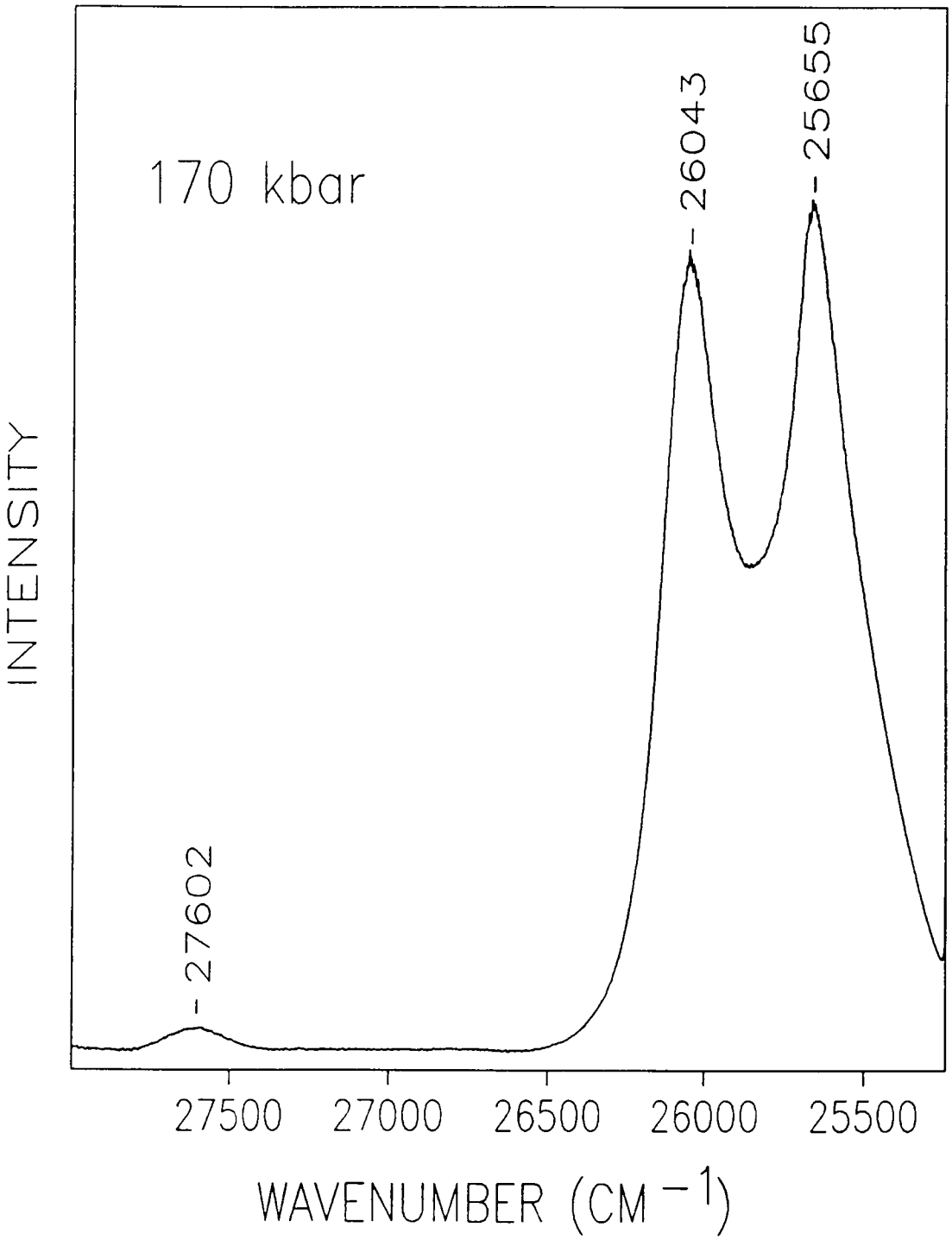

Figure 52. Absorption Spectrum of $CmCl_3$ at 170 kbar Showing the Region Covering the Transitions from the Ground State to $^6D_{7/2}$, $^6I_{15/2}$, $^6I_{13/2}$, $^6D_{9/2}$, $^6I_{11/2}$ and $^6I_{17/2}$.

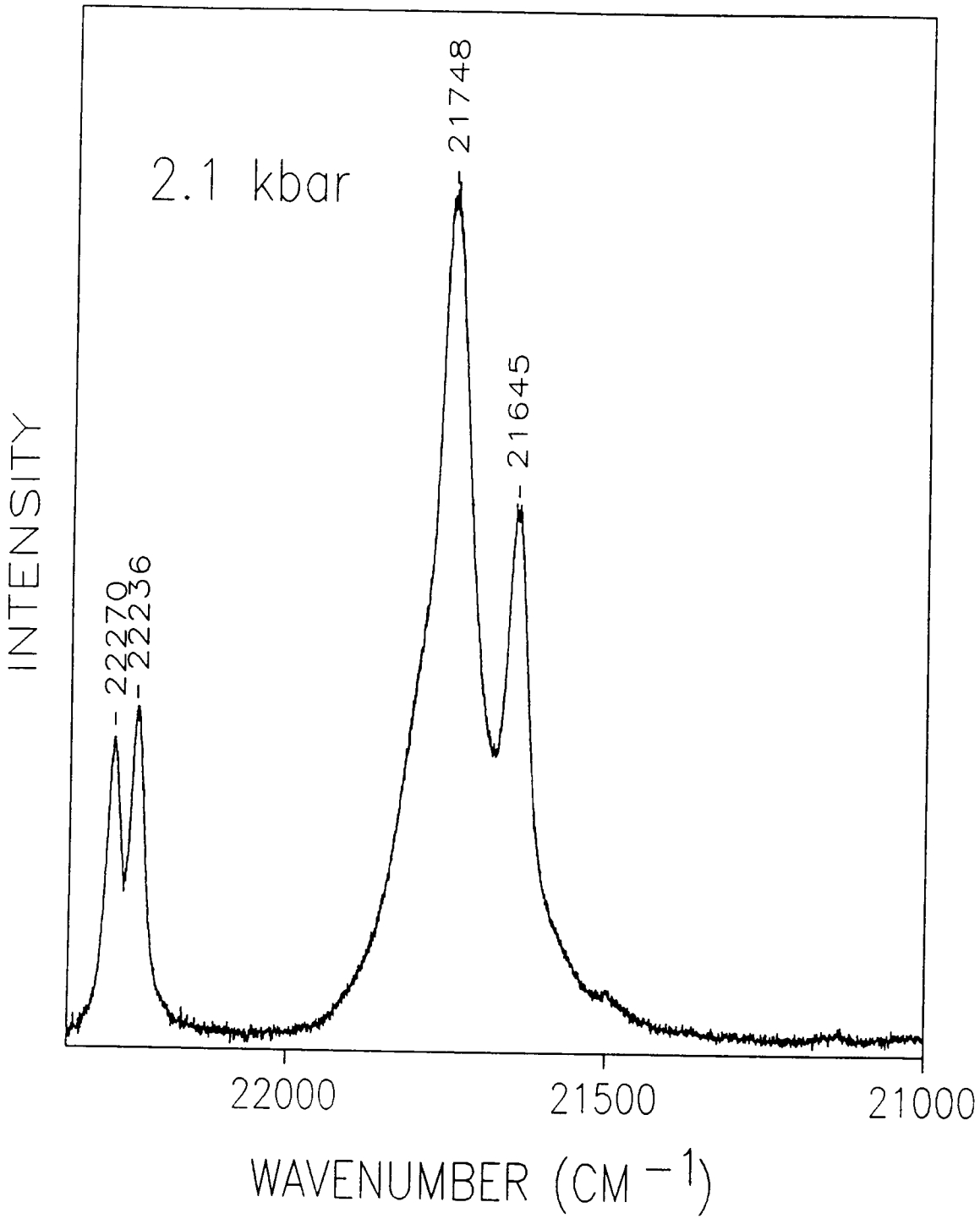

Figure 53 Absorption Spectrum of $CmCl_3$ at 2.1 kbar Showing the Region Covering the Transitions from the Ground State to $^6P_{3/2}$ and $^6I_{7/2}$.

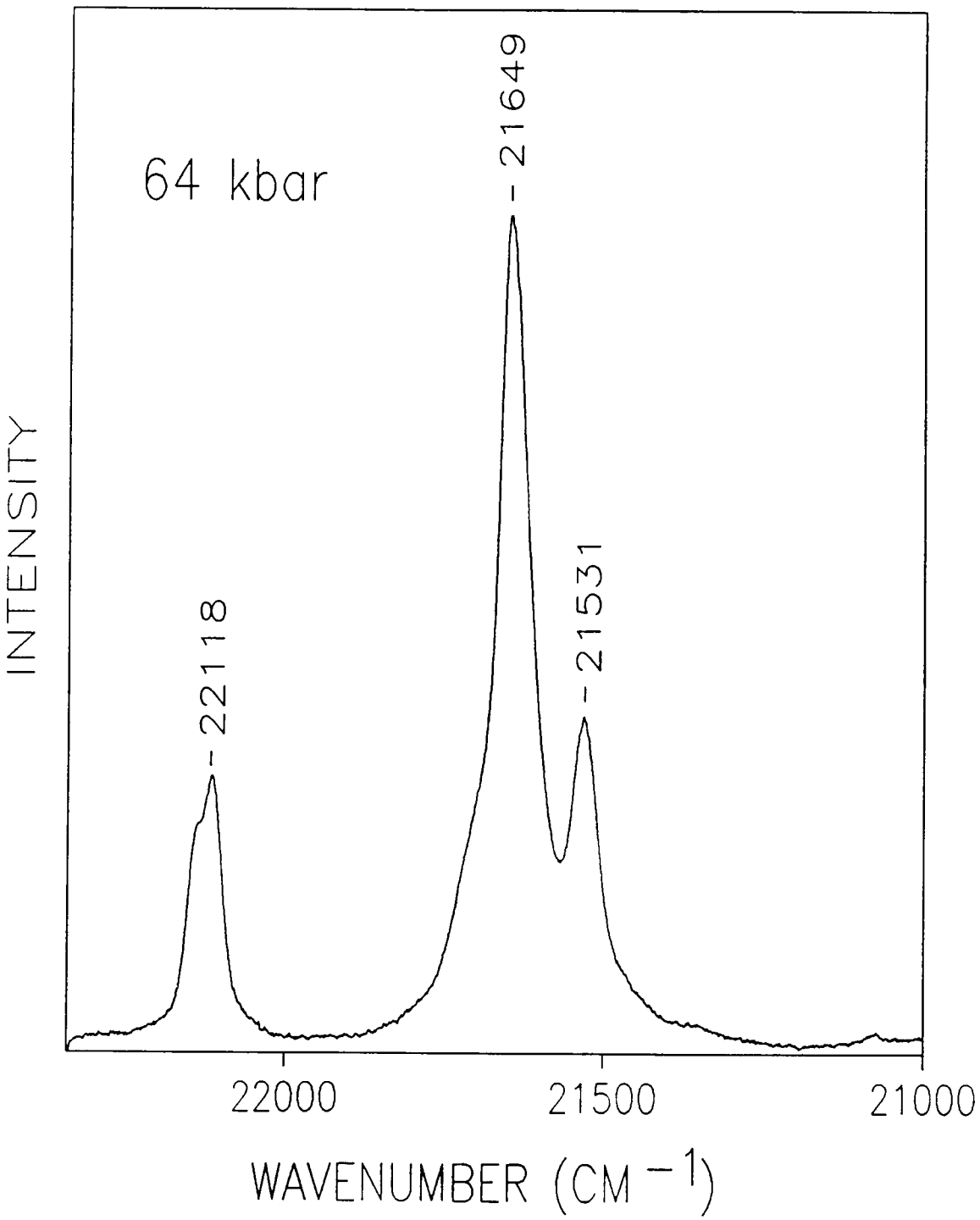

Figure 54. Absorption Spectrum of $CmCl_3$ at 64 kbar Showing the Region Covering the Transitions from the Ground State to $^6P_{3/2}$, $^6I_{7/2}$.

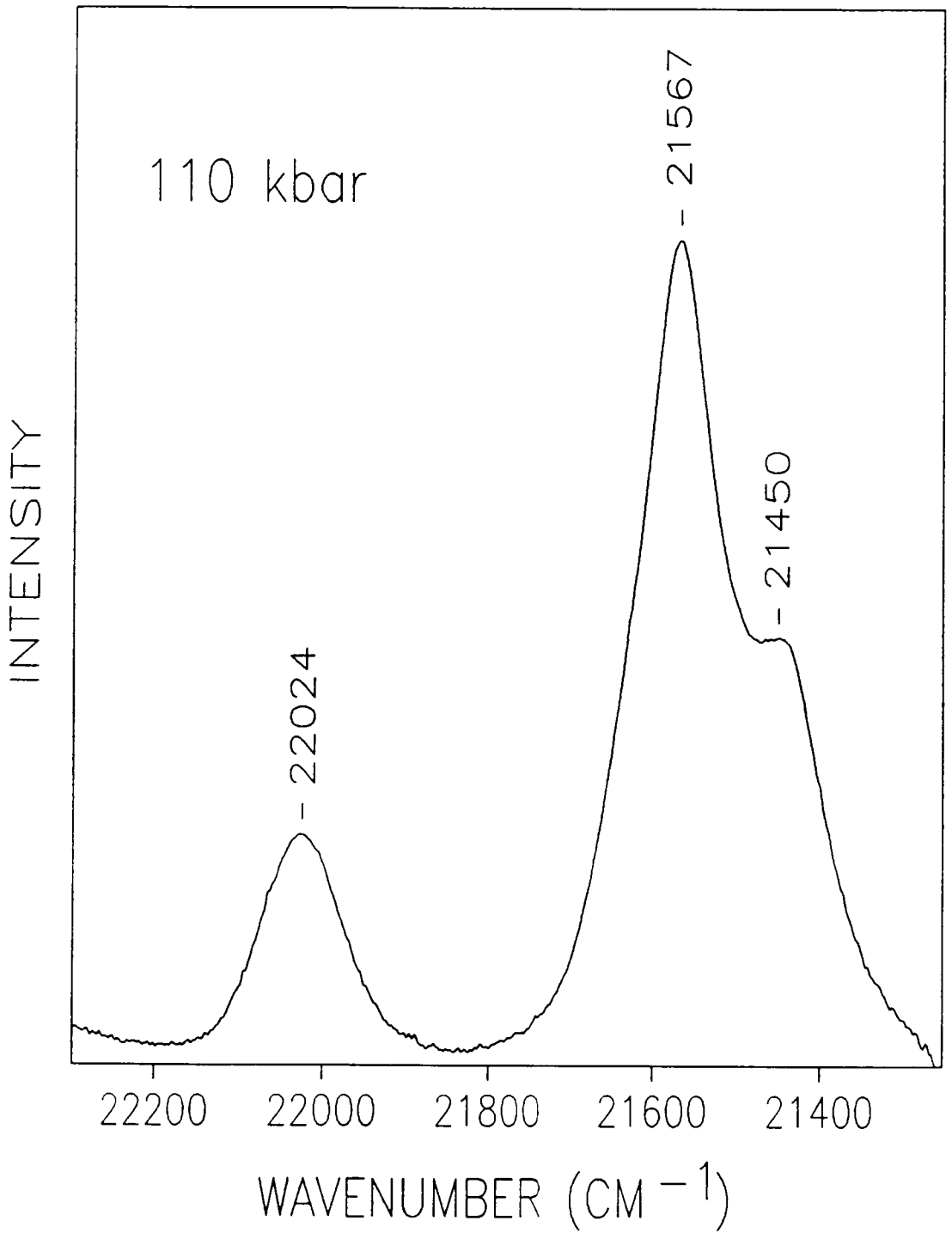

Figure 55. Absorption Spectrum of $CmCl_3$ at 110 kbar Showing the Region Covering the Transitions from the Ground State to $^6P_{3/2}$, $^6I_{7/2}$.

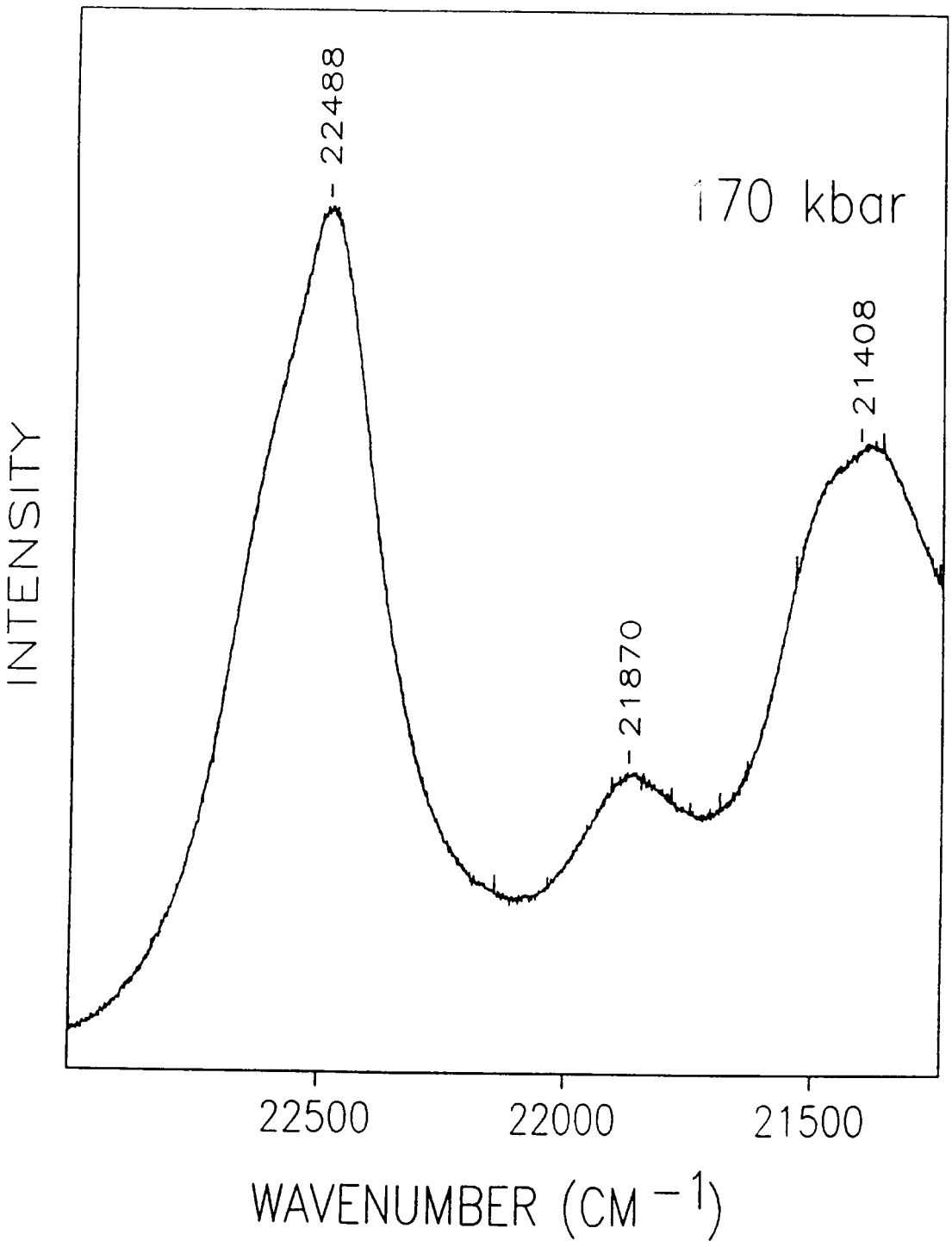

Figure 56. Absorption Spectrum of $CmCl_3$ at 170 kbar Showing the Region Covering the Transitions from the Ground State to $^6P_{3/2}$, $^6I_{7/2}$.

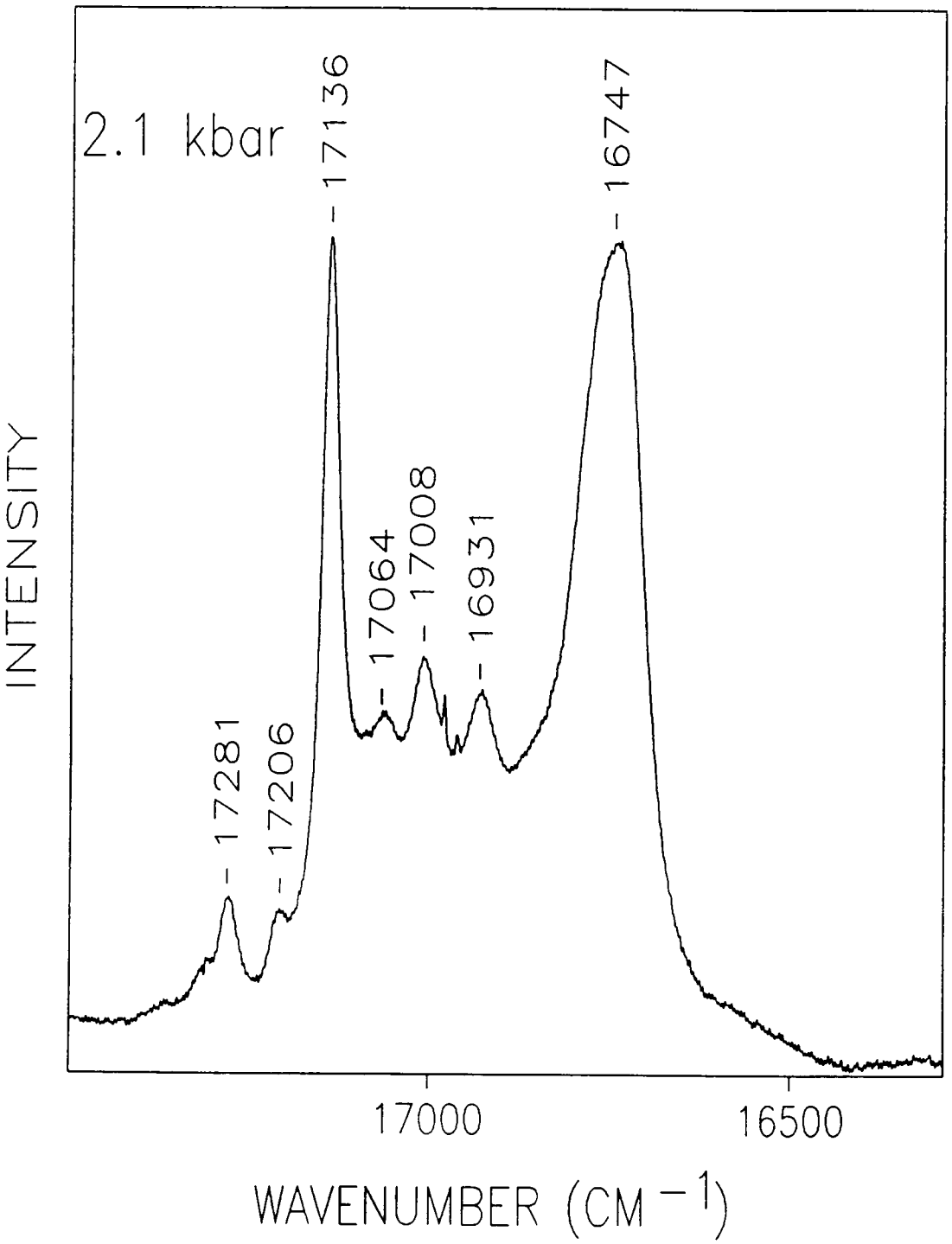

Figure 57. Absorption Spectrum of $CmCl_3$ at 2.1 kbar Showing the Region Covering the Transitions from the Ground State to $^6D_{7/2}$.

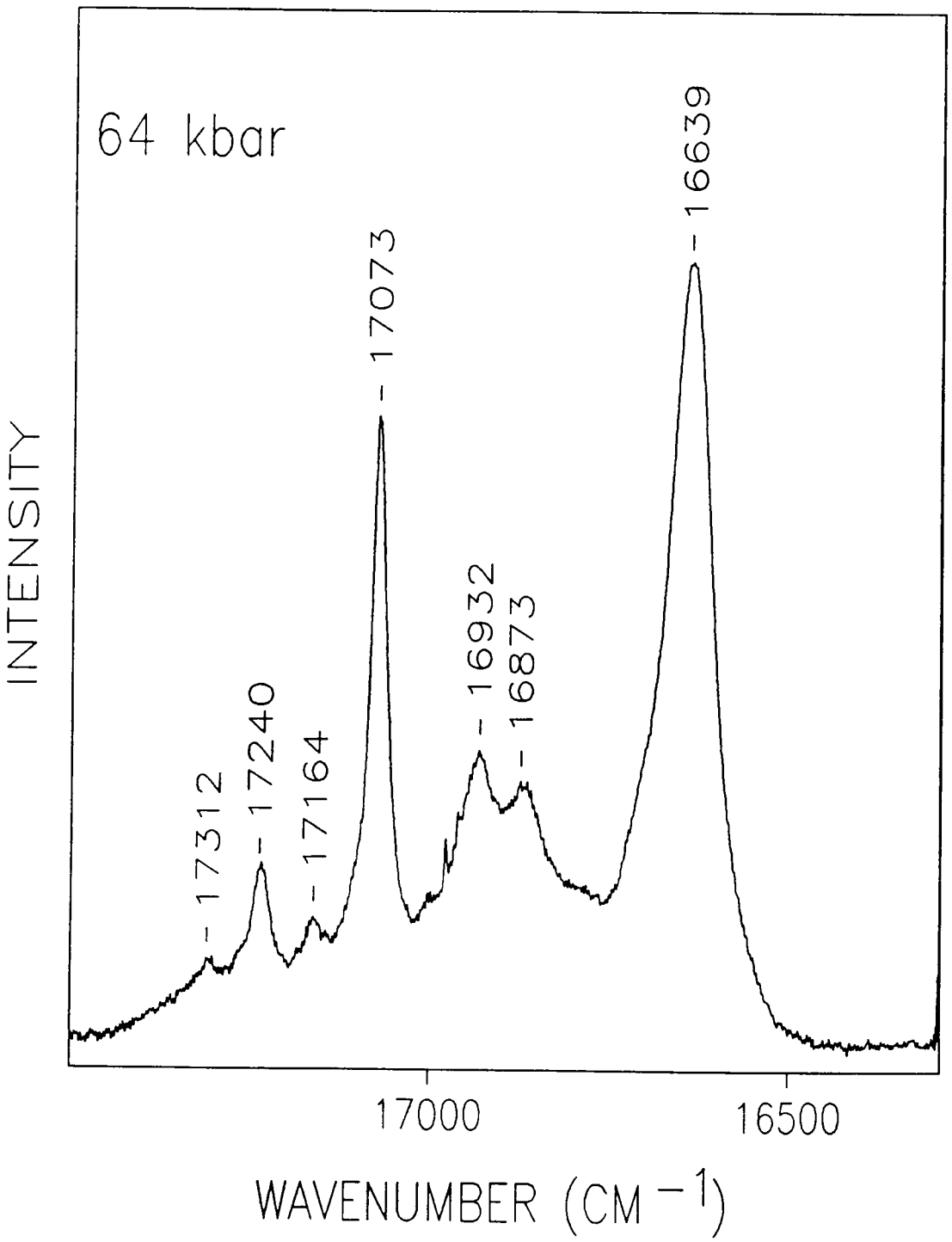

Figure 58. Absorption Spectrum of $CmCl_3$ at 64 kbar Showing the Region Covering the Transitions from the Ground State to $^6D_{7/2}$.

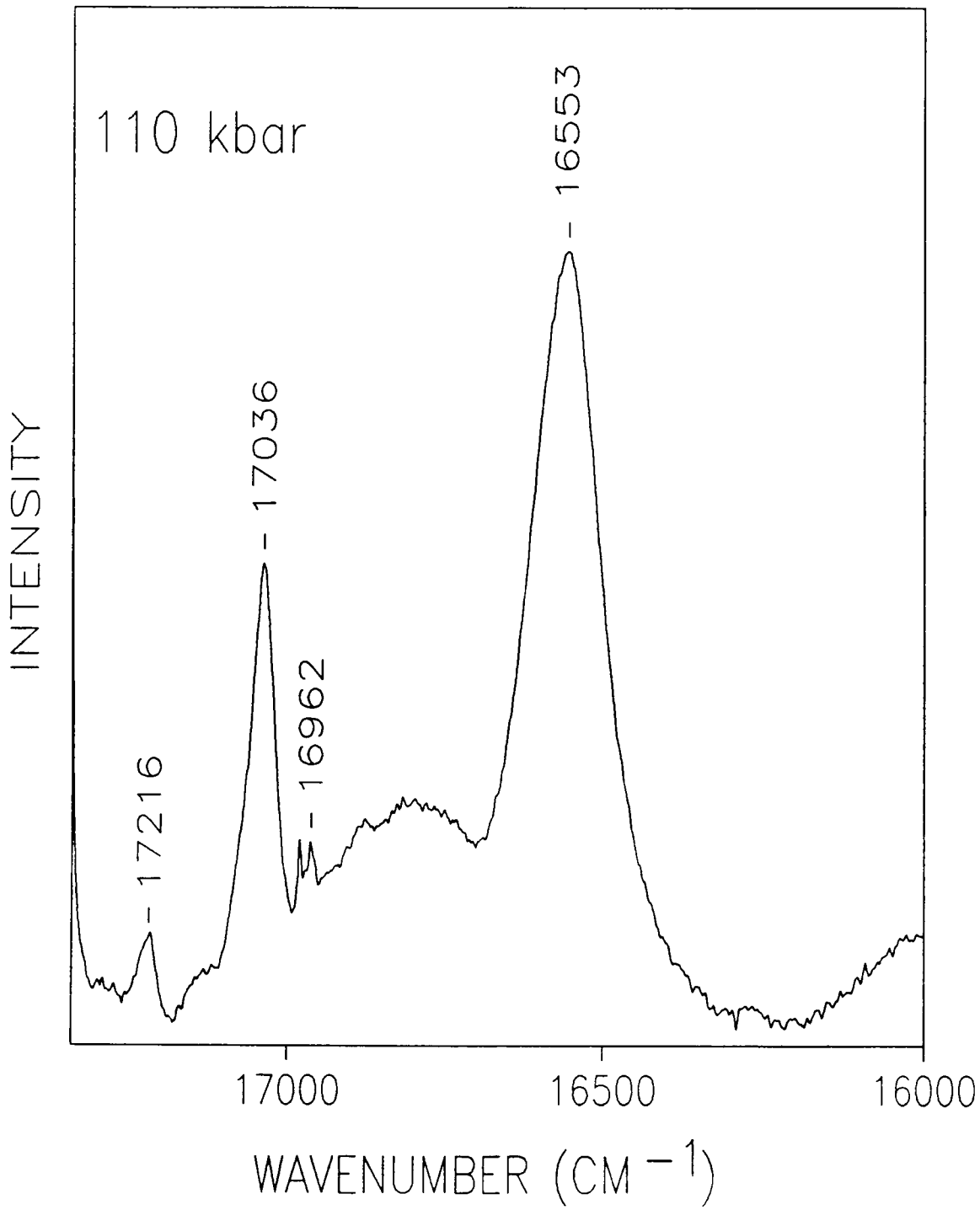

Figure 59. Absorption Spectrum of $CmCl_3$ at 110 kbar Showing the Region Covering the Transitions from the Ground State to $^6D_{7/2}$.

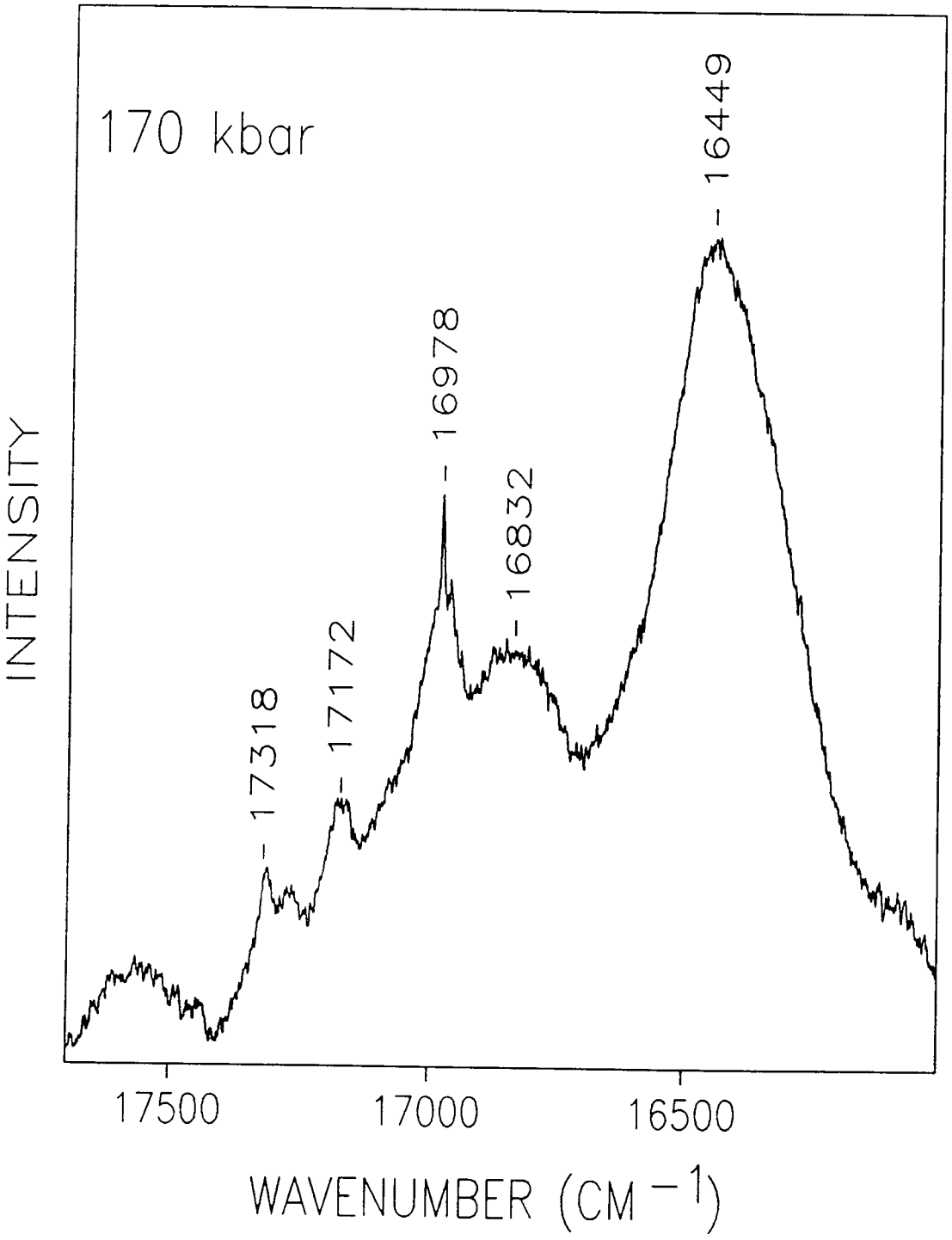

Figure 60. Absorption Spectrum of $CmCl_3$ at 170 kbar Showing the Region Covering the Transitions from the Ground State to $^6D_{7/2}$.

spectrum (see Figure 39) seems to correlate with that expected for the orthorhombic form. The pressure was then released and the Raman spectrum recorded after pressure release corresponded again with that expected for the hexagonal phase (similar to Figure 37). The reported cases [10,73] of hexagonal→ orthorhombic transformation were irreversible with pressure release ,and the orthorhombic structure remained as a metastable form. The observed reversibility in the first phase of the present work can be attributed to a distortion of the hexagonal form consisting of an enlargement in the equatorial metal-chloride linkage without having reached the critical distance at which the equatorial bond would be broken. The luminescence and absorption spectra obtained at 64 kbar (Figures 45, 50, 54, and 58) do not show any significant change from those recorded at 2.1 kbar, indicating that the curium-site ligand environment remains essentially the same.

To investigate the behavior of $CmCl_3$ at even higher pressures, a second sample was prepared and loaded into the diamond anvil cell. Raising the pressure up to 67 kbar caused the sample to undergo the orthorhombic-like distortion (not shown). At a pressure of 110 kbar, the Raman, luminescence and absorption spectra seem to indicate that the sample had experienced a phase change to a new form, distinct from the hexagonal and the orthorhombic structures (see Figures 40, 46, 51, 55, and 59). The pressure was raised up to 170 kbar and the Raman, luminescence and absorption spectra recorded seem

to indicate that the sample remains in the same form (see Figures 41, 47, 52, 56, and 60). The pressure was then released to 33 kbar. Raman and luminescence spectra were taken without delay. The spectra shown in Figures 42 and 48 do not resemble either the spectra characteristic of the hexagonal or the orthorhombic form. The splitting pattern of the luminescence spectrum is particularly striking. The band corresponding to the transition $^6D_{7/2} \rightarrow {}^8S_{7/2}$ appears split in two while the $^6I_{7/2} \rightarrow {}^8S_{7/2}$ transition that was displaying at all stages a doublet pattern appears now as a triplet. This new splitting pattern is not likely caused by a change in the metal ion site symmetry. A more plausible explanation is the presence of two different site symmetries corresponding to the simultaneous presence of two different crystal structures. After the pressure is released completely and after a waiting period, the Raman phonon spectrum indicates that the sample has reverted back to the orthorhombic form (see Figure 43). The two site symmetries could possibly correspond to a mix of the octacoordinated orthorhombic form and the suspected, new, high-pressure form, probably an hexacoordinated closest-packed structure like the BiI_3-type rhombohedral or the $AlCl_3$-type monoclinic.

C. Conclusions

The experimental evidence obtained in the present work,

although not conclusive, seems to suggest the existence of another high-pressure form besides the known orthorhombic one. This conclusion is in agreement with a previous study done on $PrBr_3$ and $NdBr_3$ carried out by our group [73]. One possible experiment that could give conclusive evidence would be the study of $EuCl_3$ under pressure unless as mentioned in Chapter V, the fine structure of Eu^{III} luminescence is obscured by an intense broad band. Another possibility is the study of europium-doped curium or californium trichloride. One problem in this latter case would be some overlap between the europium and the curium (or californium) luminescence.

LIST OF REFERENCES

LIST OF REFERENCES

1. G. T. Seaborg, Man-Made Transuranium Elements, Prentice-Hall, Englewood Cliffs, NJ (1963).

2. N. N. Greenwood and A. Earnshaw, Chemistry of the Elements, Pergamon Press, Oxford (1984).

3. G. H. Dieke, Spectra and Energy Levels of Rare Earth Ions in Crystals; H. M. Crosswhite and H. Crosswhite, Eds.; Wiley, NY (1968).

4. S. Hüfner, Optical Spectra of Transparent Rare Earth Compounds, Academic Press, NY 1978.

5. W. T. Carnall and H. M. Crosswhite, Optical Spectra and Electronic Structure of Actinide ions in Compounds and in Solution, U.S. Department of Energy Document ANL-84-90 (1985).

6. W. T. Carnall, G. L. Goodman, K. Rajnak, and R. S. Rana, A Systematic Analysis of the Spectra of the Lanthanides Doped into Single Crystal LaF_3, U.S. Department of Energy Document ANL-88-8 (1988).

7. W. T. Carnall, A Systematic Analysis of the Spectra of Trivalent Actinide Chlorides in D_{3h} Site Symmetry, U.S. Department of Energy Document , ANL-89-39 (1989).

8. D. Brown, Halides of the Lanthanides and Actinides, John Wiley & Sons Ltd., NY (1968).

9. W. R. Wilmarth and J. R. Peterson, Characterization of Selected Solid-State Actinide (and Related) Compounds Via Raman and Absorption Spectrophotometry,in Volume 6, Handbook on the Physics and Chemistry of the Actinides; C. Keller, Ed., in press.

10. J. P. Young, J. R. Peterson, R. G. Haire, W. R. Wilmarth, and G. M. Begun, High Pressure Res., in press.

11. R. G. Haire, U. Benedict, J. P. Young, J. R. Peterson, and G. M. Begun, J. Phys. C: Solid State Phys., 18, 4595 (1985).

12. J. R. Peterson, J. P. Young, R. G. Haire, G. M. Begun, and U. Benedict, Inorg. Chem., 24, 2466 (1985).

13. R. G. Haire, J. P. Young, J. R. Peterson, and U. Benedict J. Less-Common Metals, 133, 167 (1987).

14. M. C. Dagron and F. Thevet, Ann. Chim., 6, 67 (1971).

15. G. Brandt and R. Diehl, Mat. Res. Bull., 9, 411 (1974).

16. R. G. Haire, Actinides in Perspective; N. M. Edelstein, Ed.; Pergamon Press, Oxford and New York, 309 (1978).

17. J. P. Young, R. G. Haire, R. L. Fellows and J. R. Peterson, J. Radioanal. Chem., 43, 479 (1978).

18 C. M. Hollabaugh, E. I. Onstott, T. C. Wallace and M. G. Bowman, A Study of the Cerium Chlorine System for Thermochemical Production of Hydrogen, Proceedings of the Second World Hydrogen Energy Conference, 809, Zurich, (1978).

19. J. Aride, J-P. Chaminade and M. Pouchard, J. Crystal Growth, 57, 194 (1982).

20. H. Haeuseler, J. Raman. Spec., 15-2, 120 (1984).

21. H. Haeuseler and M. Jung, Mat. Res. Bull., 21, 1291 (1986).

22. R. L. Sherman and O. L. Keller, Rev. Sci. Instruments, 37, 240 (1966).

23. JCDPS Powder Diffraction File, JCDPS International Center for Diffraction Data, Swarthmore, PA (1990).

24. M. J. Buerger, The Precession Method in X-Ray Crystallography, Wiley, New York (1964).

25. Spectra Calc, version 2.12, Copyright from Galactic Industries Corporation (1988).

26. T. C. Damen, S. P. S. Porto, and B. Tell, Phys. Rev., 142, 570 (1960); Phys. Rev., 144, 771 (1966).

27. J. R. Peterson, U. Benedict, J. P. Young, R. G. Haire and G. M. Begun, Microchem. J., 34, 76 (1986).

28. S. K. Sharma, Proc. from the Int. Soc. for Opt. Eng., 1055, 105 (1989); F. Adar, J. E. Griffits, and J. M. Lerner, Eds.; Los Angeles (1989).

29. G. J. Piermarini, S. Block and J. D. Barnett, J. Appl. Phys., 44, 5377 (1973).

30. J. D. Barnett, S. Block and G. J. Piermarini, Rev. Sci. Instruments, 44, 1 (1973).

31. G. J. Piermarini and S. Block, Rev. Sci. Instruments, 46, 973 (1975).

32. H. K. Mao, P. M. Bell, J. Shaner and D. Steinberg, J. Appl. Phys., 49, 3276 (1978).

33. W. G. Fateley, F. R. Dollish, N. T. McDevitt, and F. F. Bentley, Infrared and Raman Selection Rules for Molecular and Lattice Vibrations, Wiley-Interscience, New York (1972).

34. D. L. Rosseau, R. P. Bauman, and S. P. S. Porto, J. Raman Spectrosc., 10, 253 (1981).

35. E. B. Wilson, J. R. Decius and P. C. Cross, Molecular Vibrations, McGraw-Hill, New York (1955).

36. W. H. Zachariasen, Theory of X-ray Diffraction in Crystals, Wiley, New York (1945).

37. D. H. Templeton and C. H. Dauben, J. Am. Chem. Soc., 75, 6069 (1953).

38. I. Meyer and S. Zolotov, J. Inorg. Nucl. Chem., 27, 1905, (1965).

39. International Tables for Crystallography, Vol.I, N. F. M. Henry and K. Lonsdale, Eds., Kynoch Press, Birmingham (1952).

40. B. E. Douglas and C. A. Hollingsworth, Symmetry in Bonding and Spectra, Academic Press, London (1985).

41. M. R. Bonnaire, Compt. Rendu. Acad. Sci. Paris, 266 Serie B, 1415 (1968).

42. A. Rulmont, Spectrochim. Acta, 28A, 1287 (1972).

43. L. J. Basile, J. R. Ferraro and D. Gronert, J. Inorg. Nucl. Chem., 33, 1047 (1971).

44. Y. Hase, P. O. Dunstan and M. L. A. Temperini, Spectrochim. Acta, 37A(8), 597 (1981).

45. H. Haeuseler and G. Schneider, Z. Naturforsch, 39A, 783 (1984).

46. H. Haeuseler, J. Raman Spectrosc., 15(2), 120 (1984).

47. P. C. Becker, G. M. Williams, R. E. Russo, and N. Edelstein, Optics Letters, 77, 282 (1986).

48. P. C. Becker, G. M. Williams, J. A. Koningstein, L. A. Boatner and M. M. Abraham, to be published in Phys. Rev. Lett. (1990).

49. G. Blasse, Handbook on the Physics and Chemistry of Rare Earths, 4, 237; K. A. Gschneidner and L. Eyring, Eds.; North-Holland Publishing Co., New York (1979).

50. M. J. Weber, Handbook on the Physics and Chemistry of Rare Earths, 4, 275; K. A. Gschneidner and L. Eyring, Eds.; North-Holland Publishing Co., New York (1979).

51. B. G. Wybourne, Spectroscopic Properties of the Rare Earths, 163, Interscience Publishers, New York (1965).

52. G. S. Ofelt, J. Chem. Phys., 37, 511 (1962).

53. R. D. Peacock, Structure and Bonding, 22, 83 (1975).

54. D. E. Henrie, R. L. Fellows and G. R. Choppin, Coordination Chem. Revs., 18, 199 (1976).

55. G. F. Imbush, Luminescence Spectroscopy, 1, 65; M. D. Lumb, Ed.; Academic Press, London (1978).

56. J. Hölsä and Pierre Porcher, J. Chem. Phys., 75, 2108 (1981).

57. J. Hölsä and Pierre Porcher, J. Chem. Phys., 76(6), 2798 (1982).

58. J. Hölsä, Chem. Phys. Lett., 112, 246 (1984).

59. J. Hölsä and Pierre Porcher, J. Less-Common Met., 112, 121 (1985).

60. C. A. Morrison and R. P. Leavitt, Spectroscopic Properties of Triply Ionized Lanthanides in Transparent Host Crystals, Handbook on the Physics and Chemistry of Rare Earths, 5, 461; K. A. Gschneidner and L. Eyring, Ed.; North-Holland, New York (1987).

61. K. Rajnak and B. G. Wybourne, Phys. Rev., 132, 280 (1963).

62. W. T. Carnall, H. Crosswhite, H. M. Crosswhite, and J. G. Conway, J. Chem. Phys., 64, 3582 (1976).

63. H. Samelson, A. Lempicki, and C. Brecher, J. Chem. Phys.; 40-9, 2547 (1964); 40-9, 2553 (1964).

64. J. L. Kropp and M. W. Windsor, J. Chem. Phys., 42-5, 1599 (1965).

65. W. R. Dawson, J. L. Kropp, and M. W. Windsor, J. Chem. Phys., 45-7, 2410 (1966); 45-7, 2419 (1966).

66. A. P. B. Sinha, Fluorescence and Laser Action in Rare Earth Chelates, Spectroscopy in Inorganic Chemistry, Vol. II; C. N. R. Rao and J. R. Ferraro, Eds; Academic Press, NY (1971).

67. F. Auzel, Compt. Acad. Sci., B262 , 1016 (1966).

68. M. Downer, Laser Spectroscopy of Solids II; W. Yen, Ed.; Springer-Verlag, Berlin, 1989.

69. G. M. Murray, G. D. Del Cul, G. M. Begun, R. G. Haire, J. P. Young, and J. R. Peterson, Chem. Phys. Letters, 168(5), 473 (1990).

70. L. King, J. Bigelow, and D. Collins, Transplutonium Elements - Production and Recovery, ACS Symposium Series 161, 133 (1981); J. Navratil and W. Schulz, Eds; American Chemical Society, Washington.

71. W. R. Wilmarth, G. M. Begun, R. G. Haire, and J. R. Peterson, J. Chem. Phys., 89 , 4666 (1988).

72. J. Gruger, W. Cochran, J. Conway, and A. Nichol, J. Chem. Phys., 45, 1423 (1966).

73. W. R. Wilmarth, G. M. Begun, R. G. Haire, J. P. Young, and J. R. Peterson, Appl. Spectrosc., 43, 1038 (1989).

74. J. F. Daniel, W. R. Wilmarth, G. M. Begun, and J. R. Peterson, J. Crystallogr. and Spectrosc. Res., 19, 39 (1989).

75. J. H. Burns, J. R. Peterson and R. D. Baybarz, J. Inorg. Nucl. Chem., 35, 1171 (1973).

76. R. E. Thoma and G. D. Brunton, Inorg. Chem., 5, 1937 (1966).

77. A. L. Harris and C. P. Veale, J. Inorg. Nucl. Chem., 27, 1437 (1965).

VITA

Guillermo Daniel Del Cul was born in Lanús, Buenos Aires, Argentina on March 26, 1955. He graduated from Lanús High School in December 1971. He entered La Plata National University (Argentina) in March 1972 where he received a Bachelor of Science degree with a major in chemistry in March 1976 and a Master of Science degree with a major in Physical Chemistry in December 1977. On October 28, 1977, he married Maria Amalia Steinberg. After graduation, he joined the Argentine National Institute of Technology (INTI). He left INTI in January 1979 to accept a position as Section Head of thermodynamic studies at INLAB, a private oil company in Argentina. In February 1981, he joined SEGBA (electrical utility that supplies electricity to Buenos Aires) as Associate Head of Research and Development. In August 1981, he accepted a job in the Alpha Active Division at the National Atomic Energy Commission of Argentina. In March 1986, he joined the Chemical Technology Division of the Oak Ridge National Laboratory, initially as a Guest Scientist and later on as a Consultant. He entered graduate school at the University of Tennessee, Knoxville, in January 1988 and was granted a graduate research assistantship which enabled him to conduct specialized research in the Transuranium Research Laboratory at the Oak Ridge National Laboratory in Oak Ridge, Tennessee.